

INFORMATION TO USERS

This manuscript has been reproduced from the microfilm master. UMI films the text directly from the original or copy submitted. Thus, some thesis and dissertation copies are in typewriter face, while others may be from any type of computer printer.

The quality of this reproduction is dependent upon the quality of the copy submitted. Broken or indistinct print, colored or poor quality illustrations and photographs, print bleedthrough, substandard margins, and improper alignment can adversely affect reproduction.

In the unlikely event that the author did not send UMI a complete manuscript and there are missing pages, these will be noted. Also, if unauthorized copyright material had to be removed, a note will indicate the deletion.

Oversize materials (e.g., maps, drawings, charts) are reproduced by sectioning the original, beginning at the upper left-hand corner and continuing from left to right in equal sections with small overlaps. Each original is also photographed in one exposure and is included in reduced form at the back of the book.

Photographs included in the original manuscript have been reproduced xerographically in this copy. Higher quality 6" x 9" black and white photographic prints are available for any photographs or illustrations appearing in this copy for an additional charge. Contact UMI directly to order.

UMI

A Bell & Howell Information Company
300 North Zeeb Road, Ann Arbor MI 48106-1346 USA
313/761-4700 800/521-0600

Curvature Analysis Using Multiresolution Techniques

BY

Azhar Quddus

A Dissertation Presented to the
FACULTY OF THE COLLEGE OF GRADUATE STUDIES
KING FAHD UNIVERSITY OF PETROLEUM & MINERALS
DHAHRAN, SAUDI ARABIA

In Partial Fulfillment of the
Requirements for the Degree of

DOCTOR OF PHILOSOPHY
In
ELECTRICAL ENGINEERING

September 1998

UMI Number: 9915359

UMI Microform 9915359
Copyright 1999, by UMI Company. All rights reserved.
This microform edition is protected against unauthorized
copying under Title 17, United States Code.

UMI
300 North Zeeb Road
Ann Arbor, MI 48103

KING FAHD UNIVERSITY OF PETROLEUM AND MINERALS
DHAHRAN 31261, SAUDI ARABIA

COLLEGE OF GRADUATE STUDIES

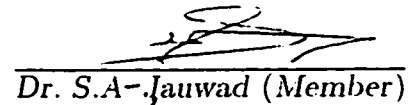
This dissertation, written by **Azhar Quddus**
under the direction of his Dissertation Advisor and approved by his Dissertation
Committee, has been presented to and accepted by the Dean of the College of Grad-
uate Studies, in partial fulfillment of the requirements for the degree of **DOCTOR**
OF PHILOSOPHY IN ELECTRICAL ENGINEERING.

Dissertation Committee


Prof. M.M. Fahmy (Advisor)


Dr. M. Bettayeb (Co - Advisor)


Dr. A.J. Al - Najjar (Member)


Dr. S.A.-Jauwad (Member)


Dr. A.S. Balghonaim (Member)


Dr. O.A. Al - Suwailem (Member)


Dr. Samir Al-Bayat
Department Chairman


Dean, College of Graduate Studies

26-10-98
Date



Dedicated to

My Parents, Shamroz

&

Maryah Azhar

whose supplication, patience and encouragement

led to this accomplishment

Acknowledgments

In the name of Allah, Most Gracious, Most Merciful

"Read in the name of thy Lord and Cherisher, who created. Created man from a [leech-like] clot. Read and thy Lord is Most Bountiful. He Who taught [the use] of the pen. Taught man that which he knew not. Nay, but man doth transgress all bounds. In that he looketh upon himself as self-sufficient. Verily, to thy Lord is the return [of all]" (The Holy Quran, Surah 96)

All praise and glory be to Almighty Allah (SWT) who gave me courage and patience to carry out this work, and peace and blessings of Allah be upon Prophet Muhammad (PBUH).

Acknowledgement is due to King Fahd University of Petroleum and Minerals for providing support for this research. Appreciation is due specially to the Library facility and to the computing and manuscript preparation facility at CCSE network. I also acknowledge the Electrical Engineering Department for its support during my course of study as a Graduate Student.

My deep appreciation goes to my thesis advisor Prof. M. M. Fahmy, for his constant help, guidance and the countless hours of attention he devoted throughout the course of this research work. He was always kind, understanding and sympathetic to me. The appreciation goes to my co-advisor Dr. M. Bettayeb for helping me with his comments and important suggestion when my advisor was not available to me.

Thanks are also due to my thesis committee members Dr. S. H. Abdul-Jauwad, Dr. A. J. Al-Najjar, Dr. A. S. Balghonaim and Dr. O. A. Al-Swailem for their interest, cooperation, advice and constructive criticism. Thanks are also due to Dr. A. R. Al-Ali and Dr. M. A. Al-Attar for giving me good suggestions at earlier stages of this thesis.

Special thanks are due to my colleagues and friends for their help and encouragement. It is worth mentioning a few like Mr. U. Qidwai, Mr. Farooq Ashraf, Mr. Syed Yunus and Mr. A. A. Farooqui. They have made my stay at KFUPM a very pleasant and unforgettable experience.

Finally, my heartfelt thanks and gratefulness to my parents, wife and other family members for their encouragement and moral support.

Contents

	Page
List of Figures	vii
List of Tables	xv
List of Symbols	xvi
Abstract (English)	xviii
Abstract (Arabic)	xix
1 INTRODUCTION	1
1.1 Literature Review	4
1.1.1 Feature Extraction	5
1.1.2 Multiresolution Analysis	7
1.1.3 Corner Detection	10
1.1.4 Observations from Literature Review	13
1.2 Research Objectives and Organization	14

2	MULTIRESOLUTION TECHNIQUES	16
2.1	Notation	17
2.2	Gabor Transform	18
2.3	Wavelet Transform	22
2.3.1	Continuous Dyadic Wavelet Transform	25
2.3.2	Discrete Dyadic Wavelet Transform	28
2.3.3	Wavelet Transform Modulus Maxima (WTMM)	30
2.4	Detection of Singularities using Wavelet Transform	31
2.5	Various Wavelets And Their Properties	33
2.5.1	Haar Wavelet	33
2.5.2	Daubechies Wavelets	33
2.5.3	Coiflet Wavelets	35
2.5.4	Symlet Wavelets	35
2.5.5	Biorthogonal Wavelets	37
2.5.6	Meyer Wavelet	37
2.5.7	Mexican Hat Wavelet	37
2.5.8	Morlet Wavelet	39
2.6	Selection of Proper Wavelet	39
3	CORNER DETECTION USING GABOR FILTERS	44
3.1	Introduction	44
3.2	Study of Corners in Frequency Domain	45

3.3	Scale Interaction Model for Corner Detection	50
3.4	Simulation results and parameter selection	61
3.4.1	Extraction of corner points	63
3.4.2	Simulation Study	64
3.4.3	Comparison	79
3.4.4	Detection Under Noise	80
3.4.5	Sensitivity with other parameters	84
3.5	Conclusions	85
4	CORNERS AND SMOOTH JOINS USING WAVELET TRANS-	
	FORM	89
4.1	Introduction	89
4.2	Assumptions Regarding Preprocessing	90
4.3	Computation of Curvature Information	91
4.3.1	Curvature Function	92
4.3.2	Radial Function	92
4.3.3	Orientation Space	93
4.4	Detection of Corners Points	96
4.4.1	The Generalized Single Corner Model	96
4.4.2	The Γ Type Corner Model	99
4.4.3	The <i>END</i> Type Corner Model	99
4.4.4	The <i>STAIR</i> Type Corner Model	101

4.4.5	Properties	102
4.4.6	Corner Detection Algorithm	103
4.4.7	Results and Comparisons	105
4.5	Smooth Joins using Wavelet Transform	107
4.5.1	Algorithm for the Detection of Smooth Joins	115
4.5.2	Results and Comparison	116
4.6	Noise Performance	116
4.7	Suitability of Other Wavelets	122
4.7.1	Haar Wavelet	122
4.7.2	Daubechies Wavelets	124
4.7.3	Coiflet Wavelets	124
4.7.4	Symlet Wavelets	127
4.7.5	Biorthogonal Wavelets	127
4.8	Conclusions	129
5	CONCLUSIONS AND SUGGESTIONS	134
	APPENDIX: MATLAB Code For Algorithms Developed	140
	Bibliography	145
	Vita	161

List of Figures

Figure		Page
2.1	Phase-space representation of Gabor transform. A Gabor transform or windowed Fourier transform $Gf(\omega_0, u_0)$ provides a description of $f(x)$ within the resolution cell of $[u_0 - \sigma_u, u_0 + \sigma_u] \times [\omega_0 - \sigma_\omega, \omega_0 + \sigma_\omega]$	21
2.2	Phase-space representation of a wavelet transform. The shape of each resolution cell depends upon the scale. When the scale increases, the resolution increases in the spatial domain and decreases in the frequency domain. The area of all the resolution cells is the same. . .	25
2.3	Spline wavelet (a) Wavelet $\psi(x)$ and (b) smoothing function $\theta(x)$. . .	42
3.1	Frequency domain study of corners (a) image of a corner (b) input image of lines (c) surface plot of the difference of magnitude of Fourier transforms of (a) and (b)	47

3.2	Frequency domain study of corners (a) contour plot of a small section of the difference of the magnitude of the Fourier transforms (b) contour plot of a mid section of the Fourier transform of the corner model in the image shown in the previous figure	48
3.3	Frequency domain study of corners (a) surface plot of the inverse Fourier transform (b) intensity plot of the inverse Fourier transform .	49
3.4	Frequency domain study of corners (a) image of a corner (b) input image of lines (c) surface plot of the difference of magnitude of Fourier transforms of (a) and (b)	51
3.5	Frequency domain study of corners (a) contour plot of a mid section of the Fourier transform of the corner model in the image shown in the previous figure (b) surface plot of the inverse Fourier transform .	52
3.6	Frequency domain study of corners (a) image of a corner (b) input image of lines (c) surface plot of the difference of magnitude of Fourier transforms of (a) and (b)	53
3.7	Frequency domain study of corners (a) contour plot of a mid section of the fourier transform of the corner model in the image shown in the previous figure (b) surface plot of the inverse Fourier transform .	54
3.8	Recovered corner images (a) intensity plot of the surface plot shown in Fig. 3.5(b), (b) intensity plot of the surface plot shown in Fig. 3.7(b)	55

3.9	Frequency response of the Gabor filter with $\sigma_x = 1, \sigma_y = 4$ and $\theta = \pi/4$ (a) Surface plot (b) Contour plot	57
3.10	Frequency response of the filter with $\sigma_{x_i} = 1, \sigma_{y_i} = 2, \sigma_{x_j} = 3, \sigma_{y_j} = 4$ and $\theta_1 = 0, \theta_2 = \pi/2$	59
3.11	Contour plot of the frequency response of the filter	60
3.12	Flow chart representation of iterative filtering scheme	62
3.13	Results of processing (a) Input image (128×128) (b) Output of the filter after convergence (c) Extracted corners	63
3.14	(a) Input image 128×128 (b) Surface plot of the image	66
3.15	(a) Filtered response with $\sigma_x = 1$ and $\sigma_y = 2$ (b) Filtered response with $\sigma_x = 3$ and $\sigma_y = 6$	67
3.16	(a) Difference response (b) Difference response after the second filtering iteration	68
3.17	(a) Difference response after the third filtering iteration (b) Difference response after the fourth filtering iteration	69
3.18	(a) Gray level input image 256×256 (b) Recall profile for various values of α and β	71
3.19	For the image shown in the previous figure: (c) Precision profile for various values of α and β (d) Goodness profile for various values of α and β	72

3.20 (a) Gray level input image 256×256 (b) Recall profile for various values of α and β	73
3.21 For the image shown in the previous figure: (c) Precision profile for various values of α and β (d) Goodness profile for various values of α and β	74
3.22 (a) Binary line drawing input image 128×128 (b) Recall profile for various values of α and β	75
3.23 For the image shown in the previous figure: (c) Precision profile for various values of α and β (d) Goodness profile for various values of α and β	76
3.24 (a) Binary input image 128×128 (b) Recall profile for various values of α and β	77
3.25 For the image shown in the previous figure: (c) Precision profile for various values of α and β (d) Goodness profile for various values of α and β	78
3.26 Profile of iterations for various values of α and β	79
3.27 (a) Result obtained by Singh and Shneier(b) Result obtained by present approach ($\alpha = 0.6$ and $\beta = 1.1$)	81
3.28 (a) Result obtained by Singh and Shneier(b) Result obtained by present approach ($\alpha = 0.4$ and $\beta = 1.0$)	82

3.29	Probability of Detection with various values of angles and signal to noise ratios (SNR) where (a) and (b) are two views of the same plot .	83
3.30	Probability of Detection with various values of angles and signal to noise ratios (SNR)	84
3.31	Goodness under noise for the gray level image shown in Fig. 3.18(a) .	85
3.32	Goodness under noise for the binary line drawing image shown in Fig. 3.22(a)	86
3.33	Goodness under noise for the binary image shown in Fig. 3.24(a) . .	87
4.1	Orientation-space representation (a) Input image 128×128 (b) orientation profile with $q = 1$ (c) orientation profile with $q = 3$	95
4.2	Corner models: (a) Generalized corner model, (b) Orientation profile of generalized corner model, (c) A Γ type corner, (d) Orientation profile of Γ type corner, (e) An <i>END</i> type corner, (f) Orientation profile of <i>END</i> type corner, (g) <i>STAIR</i> type corner, (h) Orientation profile of <i>STAIR</i> type corner	97
4.3	A demonstration (a) input image 128×128 (b) orientation space $\phi(t)$ (Top), wavelet transform modulus maxima at scales 2^1 , 2^2 , 2^3 and 2^4 thereafter.	104
4.4	Result using wavelet-based corner detection algorithm with $\tau_1 = 0.4$, $\tau_2 = 0.1$ and $\tau_3 = 0.65$	107

4.5	Comparisons: (a)-(c): Corners detected using proposed technique; (d)-(f): Corners detected by Asada and Brady	108
4.6	Comparisons: (a) Corners detected using proposed technique, (b) Corners detected by Asada and Brady	109
4.7	Comparisons: (a) Corners detected using proposed technique, (b) Corners detected by Lee, Sun and Chen	109
4.8	Comparisons (a) Test image (256×256) consists of one large semi- circle and three small semi-circles, (b) corners detected using proposed scheme with $\tau_1 = 0.4$, $\tau_2 = 0.1$ and $\tau_3 = 0.65$, (c) corners detected using proposed scheme with $\tau_1 = 0.9$, $\tau_2 = 0.7$ and $\tau_3 = 0.65$, (d) corners detected by Rattarangsi-Chin	110
4.9	Comparisons (a) corners detected by Sankar-Sharma, (b) corners de- tected by Teh-Chin, (c) corners detected by Freeman-Davis, (d) cor- ners detected by Rosenfeld-Johnson, (e) corners detected by Anderson- Bezdek, (f) corners detected by Rosenfeld-Weazka	111
4.10	Profiles of smooth joins (a) Original image 256×256 with corners(1,2), inflection (3) and smooth join (4) 'S' indicates starting point of bound- ary tracking. (b) Orientation space (top) with corresponding points in the image and three levels of WTMM	113

4.11	Detection of smooth joins (a) WTMMs (at scale 2^3) after the introduction of discontinuities of the segments $start - 1$ (top), $1 - 2$ (middle) and $2 - end$ (bottom)(b) detected corners and smooth joins.	114
4.12	Test images (a) First gray level test image (b) Second gray level test image	117
4.13	Comparisons of the proposed method with Chen <i>et. al.</i> (a),(b) Edge images after thresholding and boundary tracking of the test images (c),(d) Corners and smooth joins detected using proposed scheme (e),(f) Corners and smooth joins using the technique presented by Chen <i>et. al.</i>	118
4.14	Noise performance of the proposed techniques (corner)(a) The test image, (b) $\sigma_N = 0.37$ (c) $\sigma_N = 0.72$ (d) $\sigma_N = 1.06$ (e) $\sigma_N = 1.41$ (f) $\sigma_N = 1.77$	119
4.15	Noise performance of the proposed techniques (corner) (a) $\sigma_N = 2.09$ (b) $\sigma_N = 2.43$ (c) $\sigma_N = 2.82$ (d) $\sigma_N = 3.13$ (e) $\sigma_N = 3.59$ (f) $\sigma_N = 3.85$	120
4.16	Noise performance of the proposed technique (corner and smooth joins) (a) $\sigma_N = 0.72$ (b) $\sigma_N = 1.08$ (c) $\sigma_N = 0.69$ (d) $\sigma_N = 1.04$. . .	121
4.17	Corner detection with Haar wavelet (a) Wavelet function (b) corner detection result	123
4.18	Corner detection with Daubechies wavelets (a)-(c) Wavelet functions of <i>db2</i> to <i>db4</i> (d)-(e) Results using <i>db2</i> to <i>db4</i> wavelets	125

4.19	Corner detection with Coiflet wavelets (a)-(c) Wavelet functions of <i>coif1</i> to <i>coif3</i> (d)-(e) Results using <i>coif1</i> to <i>coif3</i> wavelets	126
4.20	Corner detection with Symlet wavelets (a)-(c) Wavelet functions of <i>sym2</i> to <i>sym4</i> (d)-(e) Results using <i>sym2</i> to <i>sym4</i> wavelets	128
4.21	Corner detection with Biorthogonal wavelets (a)-(c) Wavelet func- tions of <i>bior1.3</i> , <i>bior1.5</i> and <i>bior2.2</i> (d)-(e) Results using <i>bior1.3</i> , <i>bior1.5</i> and <i>bior2.2</i> wavelets	130
4.22	Corner detection with Biorthogonal wavelets (a)-(c) Wavelet func- tions of <i>bior2.4</i> , <i>bior2.6</i> and <i>bior2.8</i> (d)-(e) Results using <i>bior2.4</i> , <i>bior2.6</i> and <i>bior2.8</i> wavelets	131
4.23	Corner detection with Biorthogonal wavelets (a)-(c) Wavelet func- tions of <i>bior3.1</i> , <i>bior3.3</i> and <i>bior3.5</i> (d)-(e) Results using <i>bior3.1</i> , <i>bior3.3</i> and <i>bior3.5</i> wavelets	132
5.1	(a) Result obtained by Gabor filter based scheme (b) Result obtained by wavelet based scheme	137
5.2	(a) Result obtained by Gabor filter based scheme (b) Result obtained by wavelet based scheme	137

List of Tables

Table	Page
2.1 Properties of Haar wavelet	34
2.2 Properties of Daubechies wavelet	34
2.3 Properties of Coiflets wavelet	36
2.4 Properties of Symlets wavelet	36
2.5 Properties of Biorthogonal wavelet	38
2.6 Properties of Meyer wavelet	38
2.7 Properties of Mexican Hat wavelet	39
2.8 Properties of Morlet wavelet	40

List of Symbols

\mathbf{L}	Set of Integer numbers
\mathbf{R}	Set of Real numbers
$\mathbf{L}^2(\mathbf{R})$	Hilbert space of measurable, square-intergrable functions
$f(x)$	Signal representation in time domain
$F(\omega)$	Signal representation in frequency domain
$Gf(\omega, u)$	Gabor transform of a function $f(x) \in \mathbf{L}^2(\mathbf{R})$
$Wf(s, u)$	Wavelet transform of a function $f(x) \in \mathbf{L}^2(\mathbf{R})$
$W_{2^j}f(x)$	Dyadic Wavelet transform of $f(x)$ at scale 2^j
$W_{2^j}^d f$	Discrete Dyadic Wavelet decomposition of $f(x)$ at scale 2^j
$S_{2^j}^d f$	Discrete Dyadic Wavelet approximation of $f(x)$ at scale 2^j
$h(x, y)$	Impulse response of a 2-D Gabor Filter
$H(u, v)$	Fourier Transform of $h(x, y)$
$f(x, y)$	2-D Input Image
$n(x, y)$	2-D noise (same size of input image)
σ_x	Filter bandwidth in x-direction
σ_y	Filter bandwidth in y-direction
$h(\sigma_x, \sigma_y, \theta)$	Gaussian shaped lowpass filter with the orientation θ
\star	Convolution
$y(x, y, \theta)$	Filtered output with $h(\sigma_x, \sigma_y, \theta)$
m	A nonlinear function
$d_{ij}(\theta)$	Difference impulse function with preferred orientation θ
p_{ij}	Filtering function for corner detection with scales 'i' and 'j'
$z(x, y)$	Magnitude of the Output of the filtering function
α	Spatial extent of the filter
β	Extent of Passband of the filter
κ	Aspect Ratio of the elliptical profile
ζ	Lipschitz regularity
CDC	Correctly detected corners
MC	Missing Corners
FC	False Corners
C	Parametric form of the tracked boundary

CF	Curvature Function
$\phi(t)$	Orientation profile along the boundary length t
q	Smoothing parameter
$\Psi(t)$	Wavelet function (derivative of the Gaussian function)
$W_j\phi(t)$	Wavelet transform of $\phi(t)$ when $\Psi(t)$ is the wavelet function

DISSERTATION ABSTRACT

NAME: AZHAR QUDDUS
TITLE: Curvature Analysis Using Multiresolution Techniques
MAJOR FIELD: Electrical Engineering
DATE OF DEGREE: September, 1998

Two computationally efficient and simple to implement schemes for detecting corners are proposed. The first scheme is based on Gabor filtering and the second is based on wavelet transform. The first technique detects only the corners and does not require preprocessing. This technique is suitable for both binary and gray level images and is suitable for both hot and cold objects. It is particularly useful when the image contains multiple objects and/or objects under occlusion. The second scheme detects corners, inflection points as well as smooth joins. This technique was also tested with various well known wavelets and the results are summarized. The two schemes have been successfully tested under noisy conditions. They were compared with currently existing techniques to demonstrate their competitiveness and computational efficiency.

DOCTOR OF PHILOSOPHY DEGREE

KING FAHD UNIVERSITY OF PETROLEUM AND MINERALS
Dhahran, Saudi Arabia

September, 1998

خلاصة الرسالة

اسم الطالب الكامل	: أزهر قدوس
عنوان الدراسة	: تحليل التقوسات باستعمال الطرق ذات الدقة المتعددة
التخصص	: هندسة كهربائية
تاريخ الشهادة	: سبتمبر 1998

في هذا البحث اقترحنا طريقتي فعاليتين من حيث سرعة الحساب، و بسيطة من حيث البرمجة، و ذلك لاكتشاف الزوايا. الطريقة أولا تعتمد على مرشحات "جابر" والثانية تعتمد على التحويلية الموحية. الطريقة الأولى تظهر الزوايا فقط و لا تحتاج لعمليات حسابية مسبقة. و هي تتلاءم مع الصور الثنائية و الصور المتعددة المستويات، و كذلك مع الصورة ذات الخلقة الداكنة أو المضيئة. و الطريقة تشتغل مع الصورة التي تحتوى على أشياء متعددة أو ظاهرة جزئيا. الطريقة الثانية تظهر الزوايا، و الثنائية و كذلك اللحام الخفيفة. لقد تم اختبار هذا الطريقة مع تحويلات موجية معروفة و النتائج مبينة في البحث. الطريقتان تم اختبارهما بنجاح تحت ظروف وضوئية و تم مقارنة نتائجهما، بالطريق المستعملة حاليا لإظهار مقدار منافستهما لهذه الطريق و فعاليتهما من حيث السرعة الحسابية.

درجة الدكتوراه في الهندسة الكهربائية

جامعة الملك فهد للبترول و المعادن

الظهران، المملكة العربية السعودية

سبتمبر 1998

Chapter 1

INTRODUCTION

The visual system of a single human being does more image processing than the entire world's supply of supercomputers! (C.A. Mead [1])

The demand for robots to discriminate, recognize and classify objects has very wide ranging applications. This calls for a highly flexible, robust and intelligent computer vision system. By flexibility, it is meant that the system should allow for the recognition (detection) of objects in random positions, orientations, scales and under partial occlusion. Dominant points (i.e. Corners), having high curvature on the boundary of a planar object, often prove to be useful descriptive primitives. Such corner points, as observed by Attneave [2] in 1954, contain important information about the shape of the object. Since dominant information regarding shape is usually

available at the corners, they provide important features for object recognition, shape representation, image interpretation and classification. Shape characterization and analysis is found to be more difficult than initially thought. This is due to the fact that the digital computer is extremely effective at producing precise answers to well defined problems. In contrast, the biological systems accepts fuzzy, poorly conditioned inputs, performs a computation that is illdefined, and produces fairly good results [3]. Shapes can also be characterized using polygonal approximation [4, 5]. Such a scheme, however, will not be suitable for objects having curved boundaries.

In problems related to computer vision, it is difficult to analyze the information content of an image directly from gray level intensity of image pixels. This is due to the fact that image intensity depends upon lighting conditions. The size of the neighborhood where contrast is computed must be adapted to the size of the objects that needs to be analyzed [6]. This size provides a resolution of reference for detecting local variations of the image. Several researchers [7, 8, 9] have developed pattern matching algorithms which process the image at different resolutions. A multiresolution representation provides a simple hierarchical framework for interpreting the input image information [10]. At different resolutions, the details of an image generally characterize different physical structures of the scene. At a coarse resolution, these details correspond to the larger structures which provide the image context. It is therefore natural to analyze the image first at coarser resolution and

then gradually increase the resolution. Such type of pattern analysis is seen to be utilized by primate visual systems. For example, humans usually detect different objects (such as knife, hammer, etc.) without looking into the details of the objects. When they are asked to differentiate between similar looking objects (such as two different knives or hammers), they recognize by utilizing information at finer resolutions.

A natural candidate for multiresolution analysis is the wavelets. The wavelets, developed mostly over the last 15 years, is connected to older ideas in many other fields, including pure and applied mathematics, physics, computer science, and engineering. The Wavelet theory provides a unified framework for a number of techniques which had been developed independently for various signal processing applications. For example, multiresolution signal processing, used in computer vision [11], computer graphics [12], subband coding (developed for speech and image compression) [13], and wavelet series expansions (developed in applied mathematics) [14] have been recently recognized as different views of a single theory. In fact, wavelet theory covers the continuous and the discrete-time cases [15]. Hence, it provides very general techniques that can be applied to many tasks in signal processing, and has numerous potential applications.

Applications of Gabor filters in image processing is well known. Gabor transform [16] was first introduced by Gabor in 1946 to analyse 1-D signals in joint time-frequency scales. Applications of Gabor transform to image processing started

only when its 2-D extension was introduced in 1985 by Daughman [17]. By definition, Gabor filter is a filter whose impulse response is the Gabor elementary function (GEF), where GEF is a Gaussian modulated by a complex sinusoid. GEFs possess three desirable properties for image analysis. Firstly, The GEFs are the only functions that achieve lower bound of the space-bandwidth product as specified by the uncertainty principle [18]. This means that they can simultaneously be optimally localized in both the spatial and spatial-frequency domains. Thus, GEFs can be designed to be highly selective in frequency while enjoying good spatial localization. Secondly, the shapes of GEFs resemble the receptive field profiles of simple cells in visual pathways [17]. Finally, they are tunable bandpass filters. Thus, GEFs can be configured to extract a specific band of frequency components from an image [19].

In this chapter, a literature review is provided in the area of feature extraction, multiresolution analysis and the corner detection of planar objects in images. Based on the observations from the literature review, research objectives are stated.

1.1 Literature Review

A typical computer vision system for shape analysis consists of several important modules such as image acquisition, feature extraction and shape analysis. There is satisfactory development in the area of image acquisition as images of required resolution can be obtained from almost all types of environments. But the devel-

opment of the remaining subsystems proved to be more difficult than was initially thought [1]. Hence, before working on a computer vision system it is imperative to study existing systems available in the literature. In the literature survey that follows, feature extraction techniques will be discussed, and followed by multiresolution analysis and corner detection techniques.

1.1.1 Feature Extraction

Endlich and Wolf [20] presented a method based on pattern recognition that uses both infrared and visible satellite images to measure cloud displacement. First, landmarks are matched using cross-correlation after eliminating clouds by thresholding. This landmark matching is used to detect translation between pictures. Then, clouds are separated from the background by a variable brightness threshold. Groups of trackable clouds are then identified. They used the infrared value to detect clouds at different heights. For the groups selected, the following descriptors were computed: size, location of the center, average brightness, average infrared value and rms dispersion along the x and y axes. As can be seen, all these parameters will not be available from a traditional camera.

Yen and Huang [21, 22] used straight line correspondence of rigid objects and the geometrical properties of their projections on the unit sphere. Ishikawa et al. [23] used the projection of the intensity function onto the coordinate axes as a description of a given shape. Gambitto [24] measured the correspondence based on

the distance between objects in consecutive images and the difference in their areas. Since these geometrical properties change during occlusion, these techniques are not suitable under such circumstances.

Kories and Zimmermann [25] evaluated five different feature detectors. Among point, line and blob detectors, they found that the best results are obtained by combining a blob and a line detector. The method classifies the image into regions with constant gray values, regions where gray values are monotonically sloped, and local maxima. However, finding these regions is not computationally efficient. Moreover, this detection will lead to bad results when the input image is noisy.

For the occlusion caused by one object on another, the techniques based on global features (such as area, perimeter, etc.) would perform unreliably because occlusion causes change in these features. Local features such as corners [26], protrusions, holes [27], lines [28, 29], curves [30] and textures [31] can recognize and identify objects even in the presence of occlusion. Koch and Kashyap [4] provided a robust feature extraction scheme using polygonal approximation. Liu and Srinath [5] later proposed a scale-space based polygon approximation technique for pattern recognition. However, techniques using polygon approximation will not perform reliably with objects of curve shaped boundary.

1.1.2 Multiresolution Analysis

Before the advent of multiresolution techniques, the Fourier transform was the main mathematical tool for analyzing transients and singularities. The Fourier transform is global and provides a description of the overall regularity of signals, but it is not well-suited for finding the location and spatial distributions of singularities. This limitation motivated researchers to use multiresolution transforms such as Gabor Transform, Scale Space Filtering and Wavelet Transform to deal with various computer vision problems.

The technique of multiresolution analysis is quite old and was used with different names and variations. Hall *et.al.* (1976) [7] devised image matching technique using hierarchical feature extraction. Burt and Adelson [32], Keoderink [10], Marr [33], and Rosenfeld *et. al.* [9, 6] established the necessity to extract multiscale image information. These ideas were later refined by the wavelet theory [34].

Gabor Transform

As already discussed, Gabor transform [16] was first introduced by Gabor in 1946 to analyse 1-D signals in joint time-frequency scales. Applications of Gabor transform to image processing started only when its 2-D extension was introduced in 1985 by Daughman [17]. Porat and Zeevi [35] supported Gabor transform on neurophysiological evidence that the early processing of simple cortical cells in the human visual system resemble Gabor profiles. Since then many applications of Ga-

bor transform in the area of image processing and computer vision were explored. *Gabor functions have the unique property that these are the only functions that achieve lower bound of the space-bandwidth product as specified by the uncertainty principle* [18]. Hence, they can simultaneously be optimally localized in both the spatial and spatial-frequency domains. In the area of texture segmentation, Gabor Transform proved to be very useful due to its above stated property [19, 18, 36]. Daughman [37] used Gabor Transform in image compression where Gabor basis functions were computed using neural network.

Since spatial and frequency resolution of a Gabor transform is constant [34], it is mostly suitable for analyzing signals where all patterns appear approximately at the same scale. On the other hand, if the signal has important features of very different sizes, an optimal resolution for analyzing the signal cannot be defined [38]. This is particularly the case with images.

Scale space filtering

The notion of scale space filtering was first proposed by Witkin [39]. Here, the idea is to smooth the input signal with a Gaussian shaped smoothing function with different scales. The zero crossings of a function of a signal are mapped onto scale versus location space. Witkin named this representation space as *finger prints*. Application of this approach has been applied to solve various problems of computer vision [5, 40, 41, 42]. Theoretically, scale space filtering requires that decomposition be

computed at all possible scales. Hence, it requires a lot of computations. Moreover, this representation is not orthogonal (hence inverse transform does not exist) [39].

Wavelet Transform

In computer vision, generally, the structures that we want to recognize have very different sizes. Hence, it is not possible to define *a priori* an optimal resolution for analyzing images. This is the disadvantage of using Gabor/windowed Fourier transform in computer vision applications. Wavelet theory has been developed as a unifying framework only recently, although similar ideas and constructions took place as early as the beginning of the century [43, 44, 45]. Interested reader can go through the work of Daubechies [46]. Wavelet transform is computed by expanding the signal into a family of functions which are the dilations and translations of a unique function $\psi(x)$. Grossmann and Morlet [47] have shown that any function in $L^2(\mathbf{R})$ can be characterized from its decomposition on the wavelet family $(\sqrt{s}\psi(s(x-u)))_{(s,u)\in\mathbf{R}^2}$. A wavelet transform can be interpreted as a decomposition into a set of frequency channels having the same bandwidth on logarithmic scale. Good tutorials are available in [14, 48, 13].

The discretization of wavelet transform was carried out by Daubechies [49]. Discrete wavelet transform decomposes the signal into a set of frequency channels of constant bandwidth on a logarithmic scale. The model proposed by Mallat [34] provides a mathematical interpretation of the concept of resolution. There is, par-

ticularly a large class of wavelet orthonormal bases which can be computed from quadrature mirror filters [50]. Subsequently, discrete wavelet transform turned out to be well known in signal processing community as subband coding and filter banks [51, 52, 53, 54]. This understanding of wavelets turned out to be a new avenue in developing fast algorithms for wavelet transform. Mallat and Hwang [55] presented the analysis and detection of singularities in signals. Mallat and Zhong [56] presented an elegant technique to characterize signals from multiscale edges. For a review of wavelet applications one can go through [57, 58, 11, 12, 59, 60, 61].

1.1.3 Corner Detection

Corners in digital images give important clues for shape representation and analysis [2]. Since dominant information regarding shape is usually available at the corners, they provide important features for object recognition, shape representation, image interpretation [62, 63, 64] and motion analysis [65]. Moreover, corners are advantageous to use because the two velocity components can easily be determined at these points. Corners are the robust features in the sense that they provide important information regarding objects under translation, rotation and scale change [66]. Moreover, they provide reliable clues regarding objects even under occlusion and varying background levels [63].

Many algorithms have been developed for the corner detection problem. Corner detection schemes can be broadly divided into two categories based on their appli-

cations (a) binary (suitable for binary images) and (b) gray level (suitable for gray level images) [67]. Corner detection approaches for binary images usually involve segmenting the image into regions and extracting boundaries from those regions which contain them. The goal here is to obtain a piecewise linear polygon approximation of the digital curve subject to the specified constraints on the goodness of fit. A good survey of such schemes could be found in [68] and comparison in [69]. A few sample works could be found in [70, 71, 72, 73, 74].

The techniques suitable for gray level images can be further categorized into two classes (a) Template-based, and (b) gradient-based. The template-based technique utilizes correlation between a subimage and a template of a given angle. A corner point is selected by finding the maximum of the correlation output [75]. The template-based technique is computationally expensive because all possible templates are to be applied to each subimage. A similar approach can also be found in [76]. Gradient-based techniques require computing curvature of an edge that passes through a neighborhood in a gray level image [77, 78, 79, 80]. Gradient-based techniques, however, are sensitive to noise.

Recently, Manjunath et al. [81] proposed scale-interaction model for feature extraction. Similar model was also studied in [82]. These models are based on the observation that the response to curvature and line endings results from the difference of two low-pass responses of different bandwidths. This difference is further passed through a nonlinearity. Hence, these models are highly nonlinear.

The most common approach for the detection of dominant points is via boundary information [83, 84]. Here, points which have high curvature at the boundary are detected as corners [85, 86, 87, 66, 88, 89]. Teh and Chin [66] provided a good comparison of their approach with techniques in [90, 83, 91, 92, 84]. An improvement to traditional curvature based techniques has been achieved by using multiscale analysis. The idea is to observe the curvature at various scales. Asada and Brady [40] observed that curvature changes that are only found at multiple scales are most reliably localized at the finest scale at which they are discovered. Curvature changes that are only found at fine scales are less compelling determiners of the global shapes than those found across many scales. All of the scale space techniques use the Gaussian kernel to smooth the curvature profile at different scales. A few well known scale space based techniques could be found in [42, 93, 40, 41, 94]. Another multiscale approach is wavelet transform which is more computationally efficient than its scale space counterpart. Not much research, however, has been reported regarding the using the wavelet transform based approach for corner detection [95, 96]. The boundary-based corner detection methods, based on curvature changes are robust but require to compute curvature at the boundary. There are other techniques based on facet model [97], neural networks [98], cost minimization [99], mean field annealing [100] and morphological description [67]. However, the technique based on facet model requires to use approximation theory, neural network based technique requires training and morphological description requires nonlinear approximation.

On the other hand, cost minimization and mean field annealing based technique require optimization.

1.1.4 Observations from Literature Review

From the given literature review the following is observed:

1. Corners, inflection points and smooth joins are very important features for the recognition objects. They are also robust under rotation, translation, scale change and partial occlusion.
2. Currently, available corner detection schemes lack robustness with respect to the nature of images (binary and gray level), types of objects (hot and cold) and varying background.
3. Frequency domain study of corners is lacking in the literature.
4. The enormous amount of data in images renders template based techniques impractical.
5. Effort is needed to develop corner detection schemes which do not require elaborate preprocessing such as edge detection, boundary tracking and tangent or curvature computation.
6. Wavelet transform is very efficient, robust and insensitive to noise. Detection of corners and smooth joins using wavelet transform is still at its early stages

and deserves further research.

1.2 Research Objectives and Organization

The objective of this dissertation is to develop simple and fast algorithms for the detection of corners, inflection and smooth joins in the images.

This dissertation is organized as follows. Chapter 2 gives an introduction to multiresolution analysis. Here two multiresolution techniques are introduced, Gabor Transform and Wavelet transform. Care is taken to keep this introduction brief without sacrificing the technical depth.

In Chapter 3, a corner detection technique is proposed using Gabor filters. Gabor filters are known to have optimum localization both in spatial and spatial frequency domain. In order to develop a filtering based technique for corner detection, a brief frequency domain study of the corners is presented. Here a flexible technique, suitable for both binary and gray level images, to detect dominant points is proposed. We use a combination of a set of Gabor filters in a scale interaction model to detect corners in the image. This approach has another advantage of not using the preprocessing (such as boundary tracking and tangent or curvature computation). Comparisons are provided with the available techniques in the literature. This scheme is also tested under Additive White Gaussian Noise (AWGN).

In Chapter 4 we propose a wavelet transform based scheme for the detection of

both corners and smooth joins. Here effort is exerted to develop a computationally efficient scheme for the detection of corners, inflection points and smooth joins from single wavelet transform modulus maxima. Since the modulus maxima of wavelet transform provides quite a significant amount of information with less storage or processing requirements, the techniques based on wavelet transform modulus maxima are expected to be computationally efficient. Comparisons are provided with various test images. This scheme has also been tested under AWGN noise.

In Chapter 5 we present the conclusions of this research together with proposals for future work.

Chapter 2

MULTIRESOLUTION TECHNIQUES

In this chapter, a brief introduction is provided to introduce the concept of multiresolution analysis. Multiresolution decomposition provides a scale-invariant interpretation of the image. The scale of an image varies with the distance between the scene and the optical center of the camera [34]. When the image scale is changed, the interpretation of the scene should not change. A multiresolution representation can be partially scale-invariant if the sequence of resolution parameters $(r_j)_{j \in \mathbb{Z}}$ varies exponentially. Let us suppose that there exists a resolution step $\lambda \in \mathbb{R}$ such that for all integers j , $r_j = \lambda^j$. If the camera gets λ times closer to the scene, each object of the scene is projected on an area λ^2 times bigger in the focal plane of the camera. Hence, the object is measured at a resolution λ times bigger. Hence, the details of

this new image at the resolution λ^j correspond to the details of the previous image at the resolution λ^{j+1} . Rescaling the image by λ translates the image details along the resolution axis. Here, resolution axis is the axis at which the scale changes [34].

Multiresolution representation provides a simple hierarchical framework for interpretation of image information. At different resolutions, the details of an image generally characterize different physical structures of the scene. At a coarse resolution, these details correspond to the larger structures which provide the image "context". It is therefore natural to analyze first the image details at a coarse resolution and then gradually increase the resolution. Such a coarse-to-fine strategy is useful for pattern recognition algorithms [101].

In the following, an introduction of Gabor transform and wavelet transform is presented. Then a study of singularities under wavelet transform follows.

2.1 Notation

The set of integers and real numbers are represented by \mathbf{Z} and \mathbf{R} respectively. $L^2(\mathbf{R})$ denotes the Hilbert space of measurable, square-integrable 1-D functions $f(x)$. For $f(x) \in L^2(\mathbf{R})$ and $g(x) \in L^2(\mathbf{R})$, the inner product of $f(x)$ with $g(x)$ is written as

$$\langle g(u), f(u) \rangle = \int_{-\infty}^{+\infty} g(u) f(u) du$$

The norm of $f(x)$ in $L^2(\mathbf{R})$ is given by

$$\|f\|^2 = \int_{-\infty}^{+\infty} |f(u)|^2 du$$

Convolution of two functions $f(x) \in L^2(\mathbf{R})$ and $g(x) \in L^2(\mathbf{R})$ is given as

$$f \star g(x) = \int_{-\infty}^{+\infty} f(u) g(x-u) du$$

Fourier transform of $f(x) \in L^2(\mathbf{R})$ is written as

$$\hat{f}(\omega) = \int_{-\infty}^{+\infty} f(x) e^{-j\omega x} dx$$

$l^2(\mathbf{Z})$ is the vector space of square-summable sequences

$$l^2(\mathbf{Z}) = \left\{ (\alpha_i)_{i \in \mathbf{Z}} : \sum_{i=-\infty}^{+\infty} |\alpha_i|^2 < \infty \right\}$$

Let $L^2(\mathbf{R}^2)$ be the vector space of measurable, square-integrable two dimensional functions $f(x, y)$. For $f(x, y) \in L^2(\mathbf{R}^2)$ and $g(x, y) \in L^2(\mathbf{R}^2)$, the inner product of $f(x, y)$ with $g(x, y)$ is written as

$$\langle f(x, y), g(x, y) \rangle = \int_{-\infty}^{+\infty} \int_{-\infty}^{+\infty} f(x, y) g(x, y) dx dy$$

The Fourier transform of $f(x, y) \in L^2(\mathbf{R}^2)$ is written as

$$\hat{f}(\omega_x, \omega_y) = \int_{-\infty}^{+\infty} \int_{-\infty}^{+\infty} f(x, y) e^{-j(\omega_x x + \omega_y y)} dx dy$$

2.2 Gabor Transform

The Fourier transform of a function $f(x)$ gives a measure of the irregularities (high frequencies), but this information is not spatially localized. However, the Fourier

transform $\hat{f}(\omega)$ is defined through an integral which covers the whole spatial domain. It is therefore difficult to find the positions of the irregularities. In order to localize the information provided by the Fourier transform, Gabor [16] defined a new decomposition using a spatial window $g(x)$ in the Fourier integral. This window is translated along the spatial axis in order to cover the whole signal. At a position u and for a frequency ω , the Gabor transform of a function $f(x) \in L^2(\mathbb{R})$ is defined by

$$Gf(\omega, u) = \int_{-\infty}^{+\infty} f(x) g(x - u)^* e^{-j\omega x} dx \quad (2.1)$$

where the function $g(x)$ is a Gaussian function and * indicates its biorthogonal function. Hence the synthesis equation becomes

$$f(x) = \frac{1}{2\pi} \int_{-\infty}^{+\infty} \int_{-\infty}^{+\infty} Gf(\omega, u) g(u - x) e^{i\omega x} d\omega du \quad (2.2)$$

Since the window function $g(x)$ is real and even function and the energy of its Fourier transform is concentrated in the low frequencies, it can be viewed as the impulse response of a low-pass filter. Let us denote

$$g_{\omega_0, u_0}(x) = e^{j\omega_0 x} g(x - u_0)$$

If $g(x)$ is any window, the above equation of Gabor transform can be generalized as *windowed Fourier transform* [38]. This can also be interpreted as the inner products of the function $f(x)$ with the family of functions $(g_{\omega, u}(x))_{(\omega, u) \in \mathbb{R}^2}$:

$$Gf(\omega, u) = \langle f(x), g_{\omega, u}(x) \rangle \quad (2.3)$$

In quantum physics, such a family of functions is called a family of coherent states.

The Fourier transform of $g_{\omega_0, u_0}(x)$ is given as

$$\hat{g}_{\omega_0, u_0}(\omega) = e^{-j u_0 \omega} \hat{g}(\omega - \omega_0) \quad (2.4)$$

where $\hat{g}(\omega)$ is the Fourier transform of $g(x)$. A family of coherent states thus corresponds to a translation in the spatial domain (parameter u) and in the frequency domain (parameter ω) of the function $g(x)$. This double translation is represented in a phase-space where one axis corresponds to the spatial parameter u and other to the frequency parameter ω . This is shown in Fig. 2.1. Families of coherent states have found many applications in quantum physics because they make it possible to analyze simultaneously a physical phenomenon in both the spatial and frequency domains [38].

Now we describe how a Gabor Transform and the Windowed Fourier Transform relates to a spatial or a frequency representation. Let σ_u be the standard deviation of $g(x)$

$$\sigma_u^2 = \int_{-\infty}^{+\infty} x^2 |g(x)|^2 dx \quad (2.5)$$

and the standard deviation of the Fourier transform of $g(x)$

$$\sigma_\omega^2 = \int_{-\infty}^{+\infty} \omega^2 |\hat{g}(\omega)|^2 d\omega \quad (2.6)$$

The function $g_{\omega_0, u_0}(x)$ is centered in u_0 and has a standard deviation σ_u in the spatial domain. Its Fourier transform given by (2.4) is centered in ω_0 and has a standard deviation σ_ω .

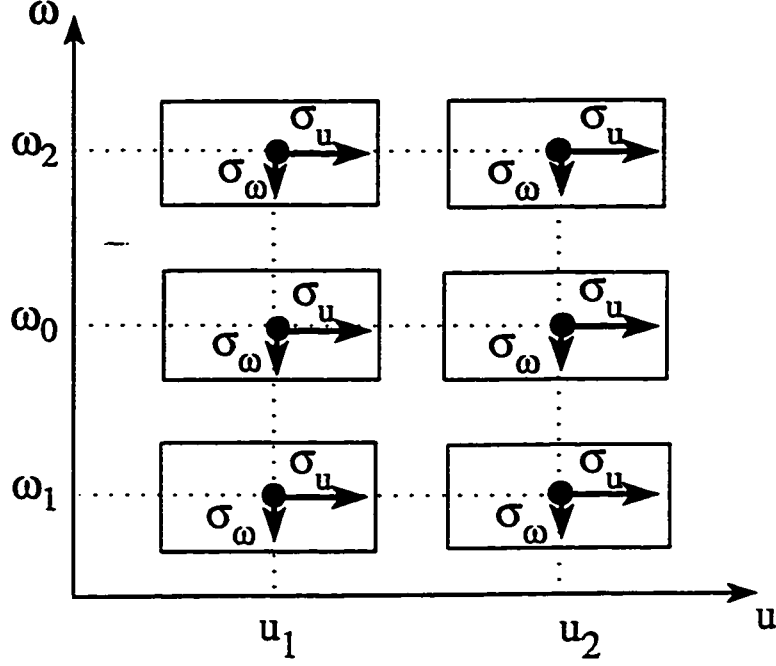


Figure 2.1: Phase-space representation of Gabor transform. A Gabor transform or windowed Fourier transform $Gf(\omega_0, u_0)$ provides a description of $f(x)$ within the resolution cell of $[u_0 - \sigma_u, u_0 + \sigma_u] \times [\omega_0 - \sigma_\omega, \omega_0 + \sigma_\omega]$

By applying the Parseval theorem to (2.3), we get

$$Gf(\omega_0, u_0) = \int_{-\infty}^{+\infty} f(x) \overline{g_{\omega_0, u_0}(x)} dx \quad (2.7)$$

$$= \int_{-\infty}^{+\infty} \hat{f}(\omega) \overline{\hat{g}_{\omega_0, u_0}(\omega)} d\omega \quad (2.8)$$

where $\overline{}$ indicates *Complex Conjugation*. The first integral shows that in the spatial domain, $Gf(\omega_0, u_0)$ essentially depends upon the values of $f(x)$ for $x \in [u_0 - \sigma_u, u_0 + \sigma_u]$. The second integral proves that in the frequency domain, $Gf(\omega_0, u_0)$ depends

upon the values of $\hat{f}(\omega)$ for $\omega \in [\omega_0 - \sigma_\omega, \omega_0 + \sigma_\omega]$. The spatial frequency domain which is covered by $Gf(\omega_0, u_0)$ can thus be represented in the phase-space by the resolution cell $[u_0 - \sigma_u, u_0 + \sigma_u] \times [\omega_0 - \sigma_\omega, \omega_0 + \sigma_\omega]$ as shown in Fig. 2.1. The surface and shape of the resolution cell is independent from u_0 and ω_0 . The uncertainty principle applied to the function $g(x)$ implies that

$$\sigma_u^2 \sigma_\omega^2 \geq \frac{\pi}{2} \quad (2.9)$$

Thus, the resolution cell can not be smaller than $2\sqrt{2\pi}$. The uncertainty inequality reaches its upper limit if and only if $g(x)$ is Gaussian, which is the case for *Gabor Transform*. Hence, with the Gabor Transform, the resolution in the phase-space is maximized. This is the most important property of the Gabor transform [18].

2.3 Wavelet Transform

Grossmann and Morlet [47] defined the wavelet transform by decomposing the signal into a family of functions which are the translation and dilation of a unique function $\psi(x)$, called *wavelet*. The corresponding wavelet family is given by

$$\left(\sqrt{s} \psi(s(x - u)) \right)_{(s,u) \in \mathbb{R}^2}$$

The wavelet transform of a function $f(x) \in L^2(\mathbb{R})$ is defined as

$$Wf(s, u) = \int_{-\infty}^{+\infty} f(x) \sqrt{s} \psi(s(x - u)) dx \quad (2.10)$$

Let the dilation of $\psi(x)$ by a factor of s be denoted as

$$\psi_s(x) = \sqrt{s} \psi(sx) \quad (2.11)$$

A wavelet transform can be rewritten as an inner product in $L^2(\mathbb{R})$

$$Wf(s, u) = \langle f(x), \psi_s(x - u) \rangle$$

Hence, wavelet transform corresponds to a decomposition of $f(x)$ on the family of functions $(\psi_s(x - u))_{(s,u) \in \mathbb{R}^2}$. In the following, both the signal $f(x)$ and wavelet $\psi(x)$ are assumed to have real values. In order to reconstruct $f(x)$ from its wavelet transform, the Fourier transform $\hat{\psi}(\omega)$ of $\psi(x)$ must satisfy

$$C_\psi = \int_0^{+\infty} \frac{|\hat{\psi}(\omega)|^2}{\omega} d\omega < +\infty \quad (2.12)$$

This condition implies that $\hat{\psi}(0) = 0$, and that $\hat{\psi}(\omega)$ is small enough in the neighborhood of $\omega = 0$. The function $\psi(x)$ can be interpreted as the impulse response of a bandpass filter.

The reconstruction of $f(x)$ from $Wf(s, u)$ is given by

$$f(x) = \frac{1}{C_\psi} \int_{-\infty}^{+\infty} \int_0^{+\infty} Wf(s, u) \psi_s(x - u) ds du \quad (2.13)$$

For normalization purpose it is assumed that the energy of $\psi(x)$ be equal to 1. Let $\tilde{\psi}_s(x) = \psi_s(-x)$. Hence, the wavelet transform at a point u and a scale s can be written as

$$Wf(s, u) = f \star \tilde{\psi}_s(u) \quad (2.14)$$

Hence, a wavelet transform can be viewed as filtering $f(x)$ with a bandpass filter whose impulse response is $\tilde{\psi}_s(x)$. Now, the Fourier transform of $\psi(x)$ is given by

$$\hat{\psi}_s(\omega) = \frac{1}{\sqrt{s}} \hat{\psi}\left(\frac{\omega}{s}\right)$$

In contrast with the Gabor transform (or windowed Fourier transform) here the resolution of the wavelet transform varies with the scale parameter s . Since $\psi(x)$ is real, $|\hat{\psi}(\omega)| = |\hat{\psi}(-\omega)|$. Let ω_0 be the center of the passband of $\hat{\psi}(\omega)$ hence,

$$\int_0^{+\infty} (\omega - \omega_0) |\hat{\psi}(\omega)|^2 d\omega = 0$$

Let σ_ω be the rms bandwidth around ω_0 hence,

$$\sigma_\omega^2 = \int_0^{+\infty} (\omega - \omega_0)^2 |\hat{\psi}(\omega)|^2 d\omega$$

The center of the passband of $\hat{\psi}_s(\omega)$ is $s\omega_0$ and that its rms bandwidth is $s\sigma_\omega$. On the logarithmic scale, the rms bandwidth of $\hat{\psi}_s(\omega)$ is the same for all $s \in \mathbb{R}^+$ [38]. In this way, a wavelet transform decomposes the signal into a set of frequency bands having a constant size on the logarithmic scale.

Let σ_u be the standard deviation of $|\psi(x)|^2$ around zero. It can be shown that the wavelet $\psi_s(x - u_0)$ has an energy concentrated around u_0 within a standard deviation σ_u/s . In the frequency domain, it can be seen that its energy is concentrated around $s\omega_0$ within a standard deviation $s\sigma_\omega$. In the phase-space, the resolution cell of this wavelet is therefore equal to $[u_0 - (\sigma_u/s), u_0 + (\sigma_u/s)] \times [s\omega_0 - s\sigma_\omega, s\omega_0 + s\sigma_\omega]$. In contrast with the Gabor transform, here the shape of the resolution cell varies

with the scale s . This is shown in Fig. 2.2. When the scale s is small, the resolution is coarse in the spatial domain and fine in the frequency domain. If the scale s increases, the resolution increases in the spatial domain and decreases in the frequency domain.

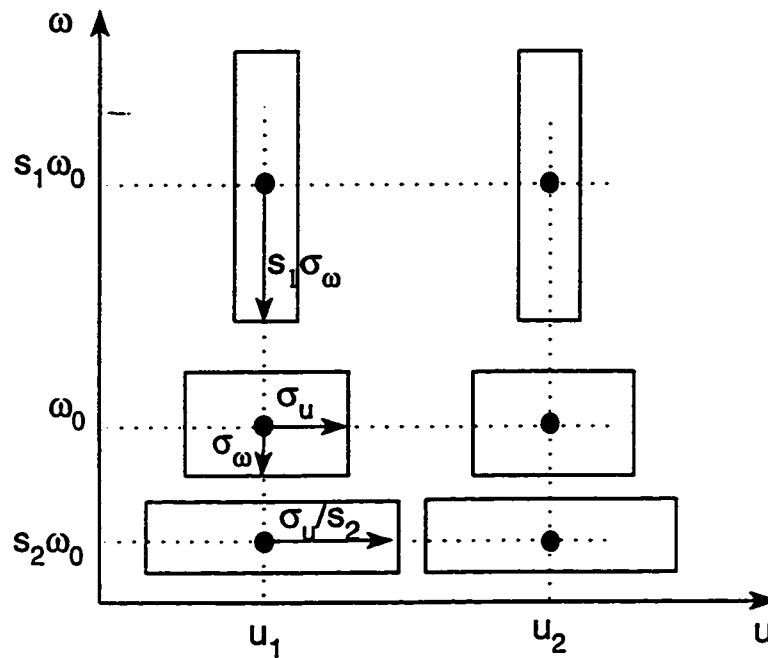


Figure 2.2: Phase-space representation of a wavelet transform. The shape of each resolution cell depends upon the scale. When the scale increases, the resolution increases in the spatial domain and decreases in the frequency domain. The area of all the resolution cells is the same.

2.3.1 Continuous Dyadic Wavelet Transform

For most purposes, the wavelet model is not required to keep continuous scale parameters. To allow fast numerical implementations, it is imposed that the scale

varies only along the dyadic sequence $(2^j)_{n \in \mathbb{Z}}$. Here a review is presented of the main properties of a dyadic wavelet transform and the conditions under which it is complete and stable. A thorough presentation can be found in [38]. Wavelet is a function $\psi(x)$ whose average is zero [56]. We denote by $\psi_{2^j}(x)$ the dilation of $\psi(x)$ by a factor 2^j

$$\psi_{2^j}(x) = \frac{1}{2^j} \psi\left(\frac{x}{2^j}\right) \quad (2.15)$$

The wavelet transform of $f(x)$ at scale 2^j and at position x is defined by the convolution product

$$W_{2^j} f(x) = f \star \psi_{2^j}(x) \quad (2.16)$$

We refer to the *dyadic wavelet transform* as the sequence of functions

$$\mathbf{W}f = (W_{2^j} f(x))_{j \in \mathbb{Z}} \quad (2.17)$$

and \mathbf{W} is the dyadic wavelet transform operator.

Now, a brief study of completeness and stability is provided. The Fourier transform of $W_{2^j} f(x)$ is

$$\hat{W}_{2^j} f(\omega) = \hat{f}(\omega) \hat{\psi}(2^j \omega) \quad (2.18)$$

By imposing that there exists two strictly positive constant A_1 and B_1 such that

$$\forall \omega \in \mathbb{R}, A_1 \leq \sum_{j=-\infty}^{+\infty} |\hat{\psi}(2^j \omega)|^2 \leq B_1 \quad (2.19)$$

we ensure that the whole frequency axis is covered by dilation of $\hat{\psi}(\omega)$ by $(2^j)_{j \in \mathbb{Z}}$ so that $\hat{f}(\omega)$, and thus $f(\omega)$, can be recovered from its dyadic wavelet transform.

The reconstruction wavelet $\chi(x)$ is any function whose Fourier transform satisfies

$$\sum_{j=-\infty}^{+\infty} \hat{\psi}(2^j \omega) \hat{\chi}(2^j \omega) = 1 \quad (2.20)$$

If property (2.19) is valid, there exists an infinite number of functions $\hat{\chi}(\omega)$ that satisfy (2.20). The function $f(x)$ is recovered from its dyadic wavelet transform with the summation

$$f(x) = \sum_{j=-\infty}^{j=+\infty} W_{2^j} f \star \chi_{2^j}(x) \quad (2.21)$$

This equation is proved by computing its Fourier transform and inserting (2.18) and (2.20). With the Parseval theorem, we derive from (2.18) and (2.19) a norm equivalence relation

$$A_1 \|f\|^2 \leq \sum_{j=-\infty}^{j=+\infty} \|W_{2^j} f(x)\|^2 \leq B_1 \|f\|^2 \quad (2.22)$$

This proves that the dyadic wavelet transform is more than complete, but still stable as $\frac{B_1}{A_1}$ is closer to 1, it becomes more stable.

A dyadic wavelet transform is more than complete; it is redundant. Any sequence $(g_j(x))_{j \in \mathbb{Z}}$, with $g_j(x) \in L^2(\mathbb{R})$, is not necessarily the dyadic wavelet transform of some function in $L^2(\mathbb{R})$. Let W^{-1} be the operator defined by

$$W^{-1}(g_j(x))_{j \in \mathbb{Z}} = \sum_{j=-\infty}^{j=+\infty} g_j \star \chi_{2^j}(x) \quad (2.23)$$

The reconstruction formula (2.21) shows that $(g_j(x))_{j \in \mathbb{Z}}$ is the dyadic wavelet transform of some function in $L^2(\mathbb{R})$, if and only if

$$W(W^{-1}(g_l(x))_{l \in \mathbb{Z}}) = (g_j(x))_{j \in \mathbb{Z}} \quad (2.24)$$

If we replace the operators \mathbf{W} and \mathbf{W}^{-1} by their expressions given in (2.16) and (2.17), we obtain

$$\sum_{l=-\infty}^{+\infty} g_l \star K_{l,j}(x) = g_j(x), \quad \forall j \in \mathbb{Z} \quad (2.25)$$

where

$$K_{l,j}(x) = \chi_{2^l} \star \psi_{2^j}(x) \quad (2.26)$$

These equations are known as reproducing kernel equations [38]. The energy of the kernel $K_{l,j}(x)$ measures the redundancy of the wavelet transform at the scales 2^j and 2^l .

2.3.2 Discrete Dyadic Wavelet Transform

Input signal is measured at a finite scale in practical applications. Hence, the wavelet transform at an arbitrary fine scale cannot be computed. Let the finest resolution be normalized to 1. In order to model this limitation, a real function $\phi(x)$ is introduced whose Fourier transform is an aggregation of $\hat{\psi}(2^j\omega)$ and $\hat{\chi}(2^j\omega)$ at scales 2^j larger than 1

$$|\hat{\phi}(\omega)|^2 = \sum_{j=1}^{+\infty} \hat{\psi}(2^j\omega) \hat{\chi}(2^j\omega) \quad (2.27)$$

It is supposed here that the reconstructing wavelet $\chi(\omega)$ is such that $\hat{\psi}(\omega) \hat{\chi}(\omega)$ is a positive, real, even function. It can be proved that property (2.20) implies that the integral of $\phi(x)$ is equal to 1 and, hence, it is a smoothing function. Let S_{2^j} be

the smoothing operator defined by

$$S_{2^j} f(x) = f \star \phi_{2^j}(x) \quad (2.28)$$

where

$$\phi_{2^j}(x) = \frac{1}{2^j} \phi\left(\frac{x}{2^j}\right)$$

If the scale 2^j is larger, the more details of $f(cx)$ are removed by S_{2^j} . For any scale $2^J > 1$, (4.27) yields

$$|\hat{\phi}(\omega)|^2 - |\hat{\phi}(2^J \omega)|^2 = \sum_{j=1}^J \hat{\psi}(2^j \omega) \hat{\chi}(2^j \omega) \quad (2.29)$$

Hence, the higher frequencies of $S_1 f(x)$, which have disappeared in $S_{2^J} f(x)$, can be recovered from the dyadic wavelet transform $(W_{2^j} f(x))_{1 \leq j \leq J}$ between the scales 2^1 and 2^J .

Let us suppose that the original signal is a discrete sequence $D = (d_n)_{n \in \mathbb{Z}}$ of finite energy. If there exists two constants $C_1 > 0$ and $C_2 > 0$ such that $\hat{\phi}(\omega)$ satisfies

$$\forall \omega \in \mathbb{R}, C_1 \leq \sum_{n=-\infty}^{+\infty} |\hat{\phi}(\omega + 2n\pi)|^2 \leq C_2 \quad (2.30)$$

then it can be proved [101] that there exists a function $f(x) \in L^2(\mathbb{R})$ (not unique) such that

$$S_1 f(n) = d_n, \quad \forall n \in \mathbb{Z} \quad (2.31)$$

The input signal can thus be rewritten as $D = (S_1 f(n))_{n \in \mathbb{Z}}$. Let us denote

$$W_{2^j}^d f = (W_{2^j} f(n + \omega))_{n \in \mathbb{Z}} \quad (2.32)$$

and

$$S_{2^j}^d f = (S_{2^j} f(n + \omega))_{n \in \mathbb{Z}} \quad (2.33)$$

where ω is the sampling shift that depends only on the wavelet $\psi(x)$. For any coarse scale 2^J , the sequence of discrete signals

$$\left\{ S_{2^j}^d, (W_{2^j}^d f)_{1 \leq j \leq J} \right\} \quad (2.34)$$

is called the *discrete dyadic wavelet transform* of $D = (S_1 f(n))_{n \in \mathbb{Z}}$.

2.3.3 Wavelet Transform Modulus Maxima (WTMM)

From the discrete wavelet transform, at each scale 2^j , we detect the modulus maxima by finding the points where $|W_{2^j} f(n + \omega)|$ is larger than its two closest neighbor values and strictly larger than at least one of them. The abscissa $n + \omega$ and the value $W_{2^j} f(n + \omega)$ at the corresponding locations are recorded.

One signal sharp variation produces modulus maxima at different scales 2^j . It is known that the value of a modulus maximum at a scale 2^j measures the derivative of the signal smoothed at the scale 2^j [56]. Wavelet theory shows that the evolution across scales of the wavelet transform depends on the local Lipschitz regularity of the signal.

2.4 Detection of Singularities using Wavelet Transform

A remarkable property of the wavelet transform is its ability to characterize the local regularity of functions [55]. In mathematics, local regularity is often measured with Lipschitz exponents.

Definition:

- Let n be a positive integer and $n \leq \zeta \leq n + 1$. A function $f(x)$ is said to be Lipschitz ζ , at x_0 , if and only if there exists two constants A and $h_0 > 0$, and a polynomial of order n , $P_n(x)$, such that for $h < h_0$

$$|f(x_0 + h) - P_n(h)| \leq A |h|^\zeta \quad (2.35)$$

- The function $f(x)$ is uniformly Lipschitz ζ over the interval $]a, b[$, if and only if there exists a constant A and for any $x_0 \in]a, b[$ there exists a polynomial of order n , $P_n(h)$, such that equation (2.35) is satisfied if $x_0 + h \in]a, b[$.
- Lipschitz regularity of $f(x)$ and x_0 , the superior bound of all values ζ such that $f(x)$ is Lipschitz ζ at x_0 .
- Function is singular at x_0 , if it is not Lipschitz 1 at x_0 .

A function $f(x)$ that is continuously differentiable at a point is Lipschitz 1 at this point. If the derivative of $f(x)$ is bounded but discontinuous at x_0 , $f(x)$ is still

Lipschitz 1 at x_0 . It follows from the above Definition that $f(x)$ is not singular at x_0 . It can be proved that if $f(x)$ is Lipschitz ζ , for $\zeta > n$, then $f(x)$ is n times differentiable at x_0 and the polynomial $P_n(h)$ is the first $n + 1$ terms of the Taylor series of $f(x)$ at x_0 . The Lipschitz regularity ζ_0 gives an indication of the differentiability of $f(x)$ but it is more precise. If the Lipschitz regularity ζ_0 of $f(x)$ satisfies $n < \zeta_0 < n + 1$, then it is known that $f(x)$ is n times differentiable at x_0 but its n th derivative is singular at x_0 and ζ_0 characterizes this singularity.

Theorem(due to [56]): Let $0 \leq \zeta \leq 1$. A function $f(x)$ is uniformly Lipschitz ζ over $]a, b[$ if and only if there exists a constant $K > 0$ such that for all $x \in]a, b[$, the wavelet transform satisfies

$$|W_{2^j} f(x)| \leq K (2^j)^\zeta \quad (2.36)$$

From the above equation we derive that

$$\log_2 |W_{2^j} f(x)| \leq \log_2(K) + \zeta j \quad (2.37)$$

Hence, if the uniform Lipschitz regularity is positive, the amplitude of the wavelet transform modulus maxima should decrease when the scale decreases. On the other hand, if the uniform Lipschitz regularity is negative, the wavelet transform modulus maxima increases. This means that such singularities are more singular than discontinuities. The signal is then viewed as tempered distribution. If the signal has uniform Lipschitz regularity ζ_0 equal to zero, then maxima values of $|W_{2^j} f(x)|$ remain constant over a large range of scales. At this stage one might wonder how

to choose a particular wavelet to estimate uniform Lipschitz regularity. In the following, this issue is discussed.

2.5 Various Wavelets And Their Properties

Here, we discuss various wavelets and their properties. Details regarding different types of wavelets are given in [102]. In the following, we discuss various well known wavelets and their properties.

2.5.1 Haar Wavelet

This is compactly supported, oldest and the simplest wavelet. This is a special case of Daubechies wavelet [102] with one vanishing moment [15]. In other words this is the same as *db1*. This is shown in Fig. 4.17(a)¹ and its main properties are illustrated in Table 2.1.

2.5.2 Daubechies Wavelets

These are compactly supported wavelets with extremal phase and highest number of vanishing moments for a given support width. Associated scaling filters are minimum-phase filters. The wavelet function ([102], p. 115, 132, 194, 242) for *db2*, *db3* and *db4* is shown in Fig. 4.18²(a), (b) and (c) respectively. These wavelets

¹see page 123

²see page 125

Table 2.1: Properties of Haar wavelet

Items	Properties
Family	Haar
Short name	haar
Examples	haar is the same as db1
Orthogonal	yes
Biorthogonal	yes
Compact support	yes
DWT	possible
CWT	possible
Support width	1
Filters length	2
Regularity	haar is not continuous
Symmetry	yes
Vanishing moments	1

Table 2.2: Properties of Daubechies wavelet

Items	Properties
Family	Daubechies
Short name	db
Order	N (strictly positive integer)
Examples	db1 or haar, db4, db15
Orthogonal	yes
Biorthogonal	yes
Compact support	yes
DWT	possible
CWT	possible
Support width	$2N-1$
Filters length	$2N$
Regularity	about $0.2 N$ for large N
Symmetry	far from
Vanishing moments	N

have vanishing moments 2, 3 and 4 respectively [15]. Its main properties [15] are illustrated in Table 2.2.

2.5.3 Coiflet Wavelets

These are compactly supported wavelets with highest number of vanishing moments for both ϕ and ψ for a given support width. These were built by Daubechies at the request of R. Coifman [102]. The wavelet function for *coif1*, *coif2* and *coif3* is shown in Fig. 4.19³(a), (b) and (c) respectively. These wavelets are more symmetrical than *dbN* family. Its main properties [15] are illustrated in Table 2.3.

2.5.4 Symlet Wavelets

These are compactly supported wavelets with least assymetry and highest number of vanishing moments for a given support width. Associated scaling filters are near linear-phase filters. These wavelets were built by Daubechies and are more symmetrical than the *dbN* [102] family. These wavelets are implemented using "minimum phase filter" [15]. The wavelet function for *sym2*, *sym3* and *sym4* is shown in Fig. 4.20⁴(a), (b) and (c) respectively. Its main properties [15] are illustrated in Table 2.4.

³see page 126

⁴see page 128

Table 2.3: Properties of Coiflets wavelet

Items	Properties
Family	Coiflets
Short name	coif
Order N	$N = 1, 2, \dots, 5$
Examples	coif2, coif4
Orthogonal	yes
Biorthogonal	yes
Compact support	yes
DWT	possible
CWT	possible
Support width	$6N-1$
Filters length	$6N$
Symmetry	near from
Vanishing moments for psi	$2N$
Vanishing moments for phi	$2N-1$

Table 2.4: Properties of Symlets wavelet

Items	Properties
Family	Symlets
Short name	sym
Order N	$N = 2, 3, \dots, 8$
Examples	sym2, sym8
Orthogonal	yes
Biorthogonal	yes
Compact support	yes
DWT	possible
CWT	possible
Support width	$2N-1$
Filters length	$2N$
Symmetry	near from
Vanishing moments	N

2.5.5 Biorthogonal Wavelets

These are compactly supported biorthogonal spline wavelets for which symmetry and exact reconstruction are possible with FIR filters (in orthogonal case it is impossible). These were built by Cohen *et. al.* [103]. It is well known that symmetry and exact reconstruction are incompatible, if the same FIR filters are used for both decomposition and reconstruction [15]. Hence they used different FIR filters for reconstruction and decomposition. This wavelet family is labeled as $biorNr.Nd$, where Nr is the filter lengths for reconstruction and Nd is the filter length for decomposition. The wavelet function for $bior1.3$, $bior1.5$ and $bior2.2$ is shown in Fig. 4.21⁵(a), (b) and (c) respectively. Its main properties [15] are illustrated in Table 2.5.

2.5.6 Meyer Wavelet

This is infinitely regular orthogonal wavelet. This wavelet and scaling function are defined in frequency domain. Its main properties [15] are illustrated in Table 2.6.

2.5.7 Mexican Hat Wavelet

This is second derivative of the Gaussian probability density function. This wavelet has no scaling function [102]. It has close form analytical expression. Its main

⁵see page 130

Table 2.5: Properties of Biorthogonal wavelet

Items	Properties
Family	Biorthogonals
Short name	bior
Order N_r, N_d	$N_r = 1, N_d = 1, 3, 5$
Examples	bior3.1, bior5.5
Orthogonal	no
Biorthogonal	yes
Compact support	yes
DWT	possible
CWT	possible
Support width	$2N_r+1$ for rec., $2N_d+1$ for dec.
Symmetry	yes
Vanishing moments for ψ	N_r-1

Table 2.6: Properties of Meyer wavelet

Items	Properties
Family	Meyer
Short name	meyr
Orthogonal	yes
Biorthogonal	yes
Compact support	no
DWT	possible but without FWT
CWT	possible
Support width	infinite
Effective support	$[-8, 8]$
Regularity	indefinitely derivable
Symmetry	yes

properties [15] are illustrated in Table 2.7.

Table 2.7: Properties of Mexican Hat wavelet

Items	Properties
Family	Mexican hat
Short name	mexh
Orthogonal	no
Biorthogonal	no
Compact support	no
DWT	no
CWT	possible
Support width	infinite
Effective support	$[-5 \ 5]$
Symmetry	yes

2.5.8 Morlet Wavelet

This is a symmetrical wavelet and has no scaling function [102]. It has closed form analytical expression. Its main properties [15] are illustrated in Table 2.8.

2.6 Selection of Proper Wavelet

It was found [55] that the number of vanishing moments of the wavelet plays a major role in detecting the required singularity from wavelet transform modulus maxima. Where a wavelet is said to have n vanishing moments, if and only if for all

Table 2.8: Properties of Morlet wavelet

Items	Properties
Family	Morlet
Short name	morl
Orthogonal	no
Biorthogonal	no
Compact support	no
DWT	no
CWT	possible
Support width	infinite
Effective support	$[-4 \ 4]$
Symmetry	yes

positive integer $k < n$, it satisfies

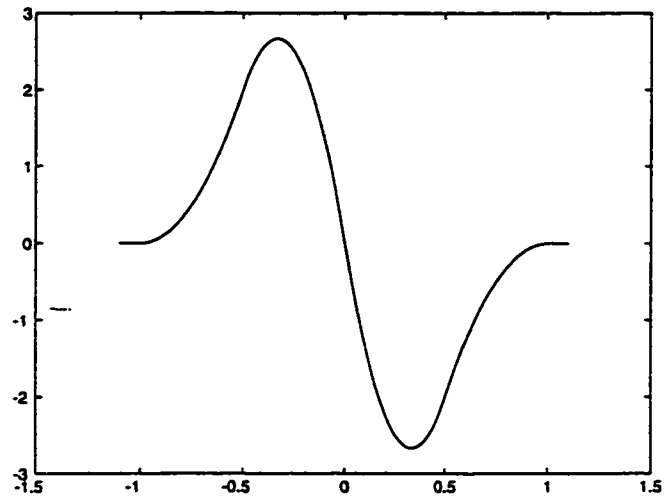
$$\int_{-\infty}^{+\infty} x^k \psi(x) dx = 0 \quad (2.38)$$

If it is needed to estimate Lipschitz exponents up to a maximum value n , a wavelet with at least n vanishing moments is needed [55]. Using wavelets with more than one vanishing moments has the advantage of being able to measure the Lipschitz regularity up to a higher order, but it also increases the maxima lines. The number of maxima at a given scale often increases linearly with the number of moments of the wavelet. In order to minimize the amount of computation, the minimum number of maxima necessary to detect the irregular behavior of the signal [55] should be known. This means that a wavelet with as few vanishing moments as possible should be selected, with enough moments, to detect the Lipschitz exponents of highest order of interest. Another related property that influences the number of modulus maxima

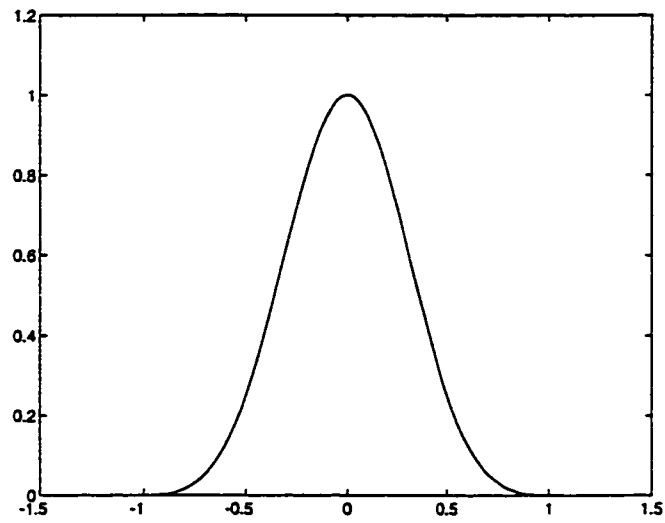
is the number of oscillations of the wavelet $\psi(x)$. For most types of singularities, the number of maxima lines converging to the singularity depends upon the number of local extrema of the wavelet itself. A wavelet with n vanishing moments has at least $n + 1$ local extrema. For numerical computations, it is better to choose a wavelet with exactly $n + 1$ local extrema [55].

It has been proved [56] that if a signal is singular at a point x_0 , there exists a sequence of wavelet transform modulus maxima that converge to x_0 when the scale decreases. Hence, the detection of all the singularities from the positions of the wavelet transform modulus maxima is possible. Moreover, the decay of the wavelet transform is bounded by the decay of these modulus maxima, and we can thus measure the local uniform Lipschitz regularity from this decay [56].

In image processing applications, it is often required to detect discontinuities and peaks that have Lipschitz exponents smaller than 1 [56]. It is, therefore, sufficient to use a wavelet with only one vanishing moment. Moreover, edges in the images sometimes have ramp profile. Hence we can model a smooth variation at x_0 as a singularity convolved with a Gaussian. Mallat and Zhong [56] proved that Lipschitz regularity in such cases can be obtained if the wavelet is derivative of Gaussian. However, derivative of Gaussian is not orthogonal. Hence, they developed a new wavelet which is very close to the derivative of Gaussian. They reported an error of less than 10 percent due to the approximation. This wavelet has one vanishing moment, and is a quadratic spline of compact support and is continuously



(a)



(b)

Figure 2.3: Spline wavelet (a) Wavelet $\psi(x)$ and (b) smoothing function $\theta(x)$.

differentiable. Fig. 2.3 shows graphical representation of the wavelet $\psi(x)$ which is a quadratic spline and its integral $\theta(x)$ which is cubic spline. Fast computational algorithms, based on Quadrature Mirror Filters (QMF), for this wavelet can be found in [56].

Chapter 3

CORNER DETECTION USING GABOR FILTERS

3.1 Introduction

As discussed in the literature review, corners in digital images give important clues for shape representation and analysis. Since dominant information regarding shape is usually available at the corners, they provide important features for object recognition, shape representation and image interpretation.

According to the requirements stated in the objectives (section 1.2), a new corner detection scheme using Gabor filters is proposed here. In this scheme the scale interaction model discussed in [81, 82] is used after being modified by deleting the nonlinearity at each filtering stage. The exclusion of the nonlinearity permits

combining the filtering functions before the filtering operation, resulting in a huge amount of computational saving. The only nonlinearity present in our model is at the final output in the form of magnitude operation. These models are based on the observation that the response to curvature and line endings results from the difference of two low-pass responses of different bandwidths. In our approach [104], we first apply the input image to the filter and then allow it to iteratively filter the previous output until the current output stabilizes. For all the test images the convergence is achieved within ten iterations.

3.2 Study of Corners in Frequency Domain

Before designing any filtering based technique for corner detection it is imperative to study corners in the spatial frequency domain. In this section, we provide the study on where to find corners in the spatial frequency domain.

Fig. 3.1(a) and (b) show images of a corner and lines, respectively. As can be seen here, both images consist of two lines of the same length and angles. There are two differences between them. First, the first image forms a corner and the second one does not form a corner. Second, the first image has two line endings while the second image has four line endings. Hence, the Fourier transform of both the images (with dc removed) are quite similar. The difference of the magnitude of their Fourier transform is computed, as shown in Fig. 3.1(c). Here, we observe that

the maximum of the difference is concentrated very close to the dc. The central part of this difference is zoomed and is shown in Fig. 3.2(a). Hence, we infer that the frequencies related to corners and line endings are concentrated very close to dc. In order to further demonstrate this point we consider the central part of the Fourier transform of the corner model of the previous figure which is shown in Fig. 3.2(b). The inverse Fourier transform was applied to this part (shown in Fig. 3.2(b)) and the result is shown as a surface plot and as intensity image in Fig. 3.3(a) and (b), respectively. Here, we observe that the recovered image has high amplitudes at corners and line endings. This proves our inference that the corners and line endings generate low frequencies which are very close to dc.

We conducted similar study with corners at larger angles. Fig. 3.4(a) shows a corner at a wider angle than the previous case and Fig. 3.4(b) shows these lines without forming a corner. Fig. 3.4(c) shows the difference of the magnitude of their Fourier transform. Here, we observe that the difference is maximum near dc, but its magnitude is less than the previous case. Fig. 3.5(a) shows the the central part of Fourier transform of corner model of the previous figure. Fig. 3.5(b) shows the surface plot of the inverse Fourier transform was applied to the part (shown in Fig. 3.5(b)). Fig. 3.6(a) shows a corner at still a wider angle than the previous case and Fig. 3.6(b) shows these lines without forming a corner. Fig. 3.6(c) shows the difference of the magnitude of their Fourier transform. Here we observe that the difference is not maximum near dc. Fig. 3.7(a) shows the central part of the

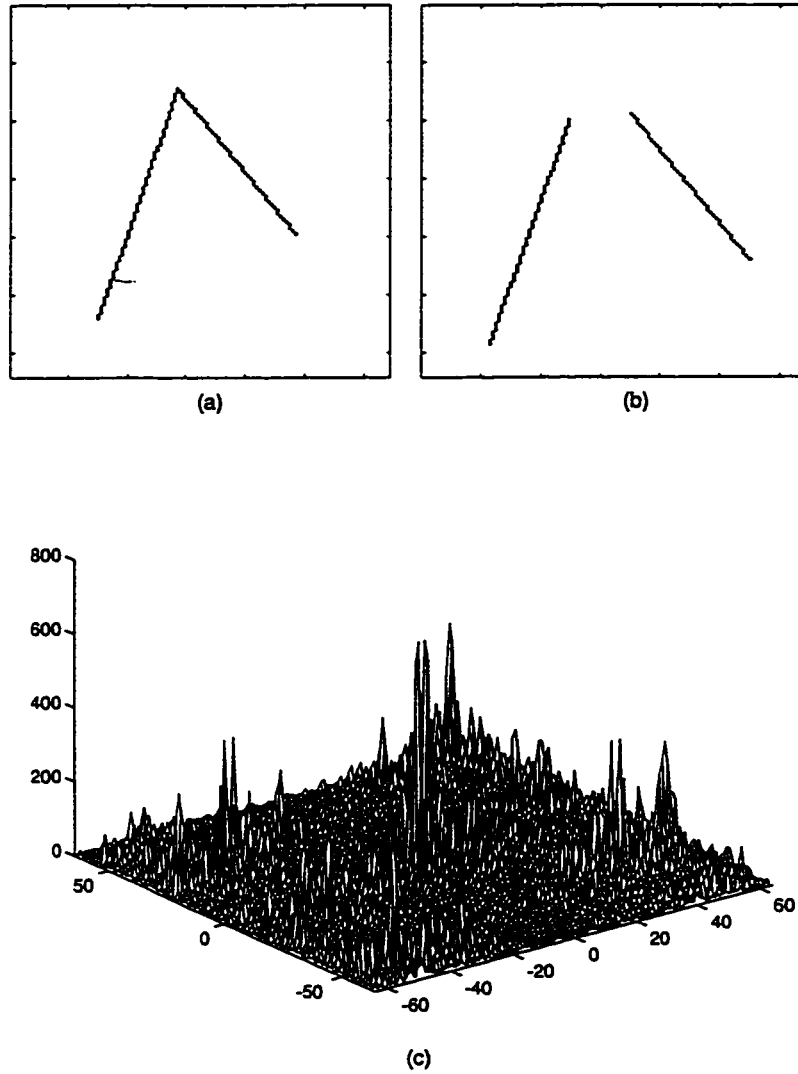


Figure 3.1: Frequency domain study of corners (a) image of a corner (b) input image of lines (c) surface plot of the difference of magnitude of Fourier transforms of (a) and (b)

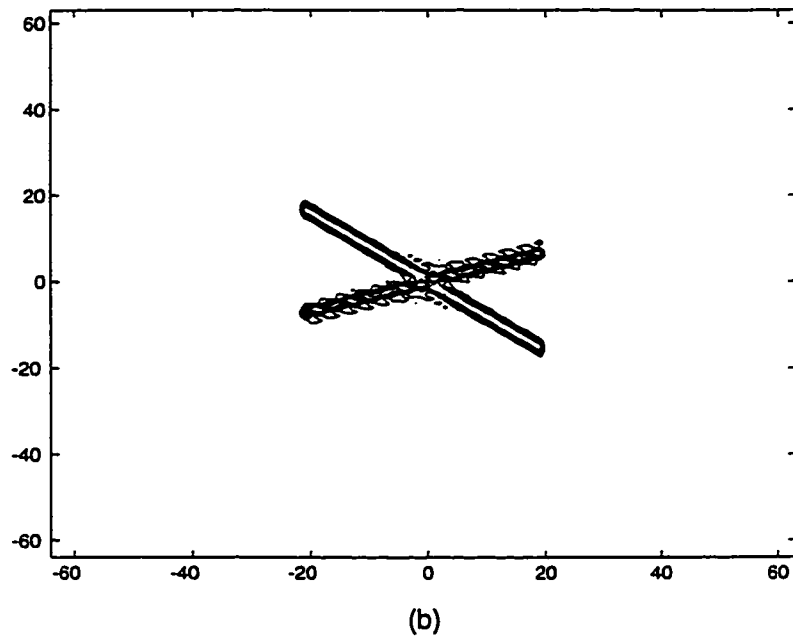
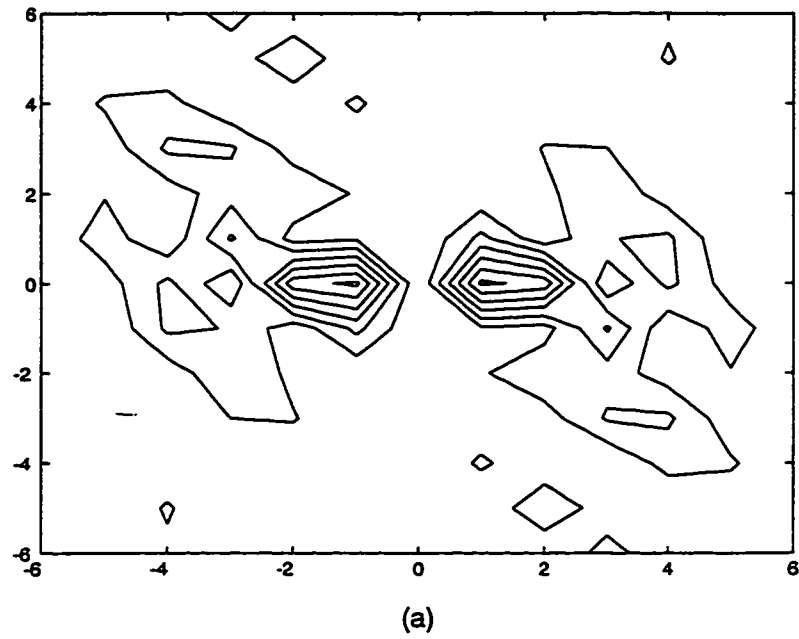
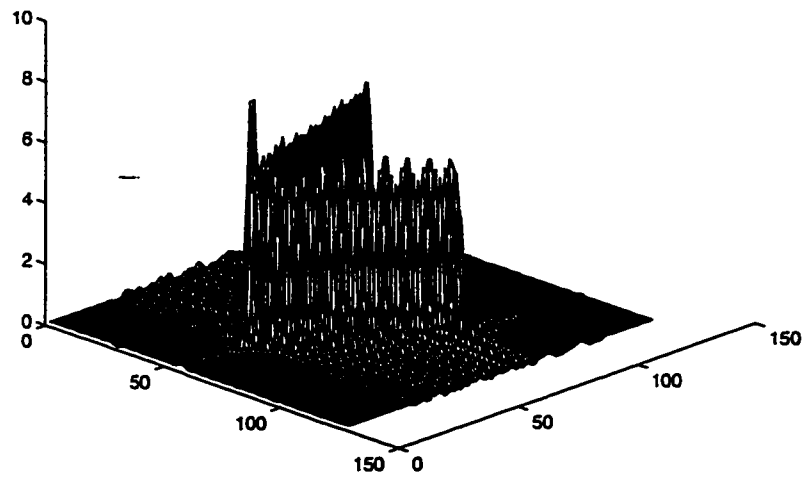
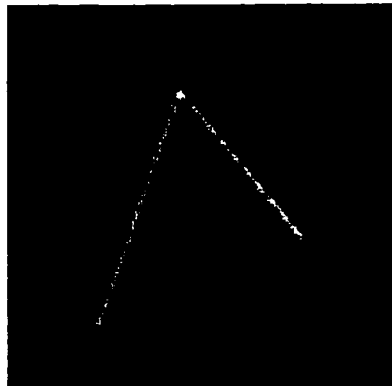


Figure 3.2: Frequency domain study of corners (a) contour plot of a small section of the difference of the magnitude of the Fourier transforms (b) contour plot of a mid section of the Fourier transform of the corner model in the image shown in the previous figure



(a)



(b)

Figure 3.3: Frequency domain study of corners (a) surface plot of the inverse Fourier transform (b) intensity plot of the inverse Fourier transform

Fourier transform of the corner model of the previous figure. Fig. 3.7(b) shows the surface plot of the inverse Fourier transform of the part shown in Fig. 3.5(b). Fig. 3.8(a) and (b) shows the intensity plots of the surface plots shown in Fig. 3.5(b) and 3.7(b), respectively.

From Figs. 3.1, 3.4 and 3.6 we observe that as the angle at the corner increases, the frequencies near dc get diminished. Hence at larger angles it is difficult to detect corners. Moreover, frequencies at the corners are mixed up with those of the edges. Hence, one has to design a filter which neither passes dc nor high frequencies. Such a filter should however, respond to edges. Hence a filtering mechanism has to be devised so that we can have responses only at the corners. In the following section this is precisely what was successfully done using scale interaction of Gabor filters.

3.3 Scale Interaction Model for Corner Detection

In this section, we introduce Gabor filter based scale interaction model to detect corners in images. We also introduce an iterative filtering scheme to detect only the corners from the images.

In its general form, the Gabor filter is a bandpass filter having impulse response $h(x,y)$ [92]:

$$h(x,y) = g(x',y') \exp[-j2\pi(Ux + Vy)] \quad (3.1)$$

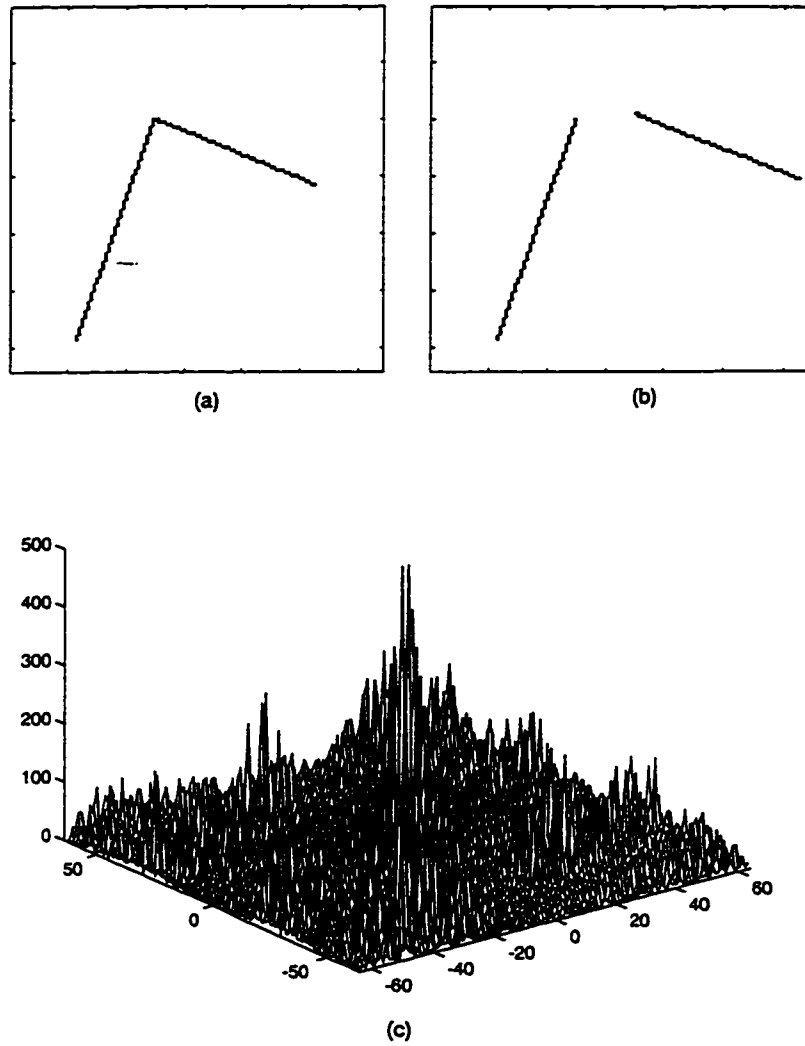


Figure 3.4: Frequency domain study of corners (a) image of a corner (b) input image of lines (c) surface plot of the difference of magnitude of Fourier transforms of (a) and (b)

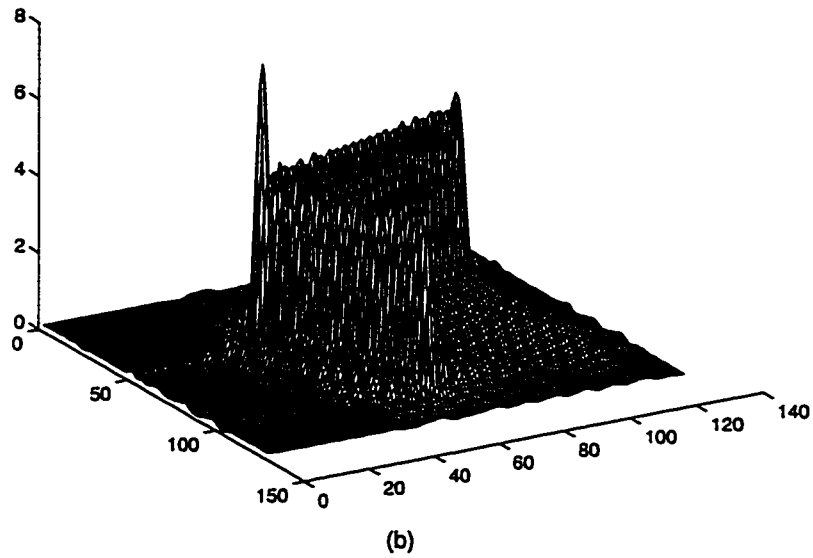
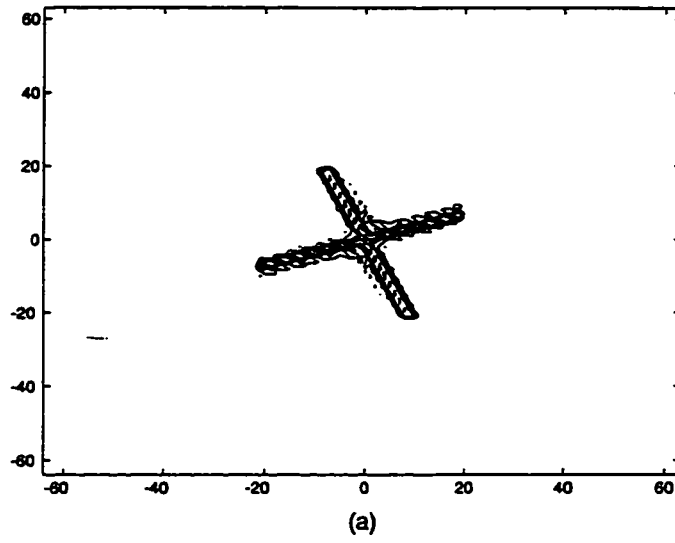


Figure 3.5: Frequency domain study of corners (a) contour plot of a mid section of the Fourier transform of the corner model in the image shown in the previous figure (b) surface plot of the inverse Fourier transform

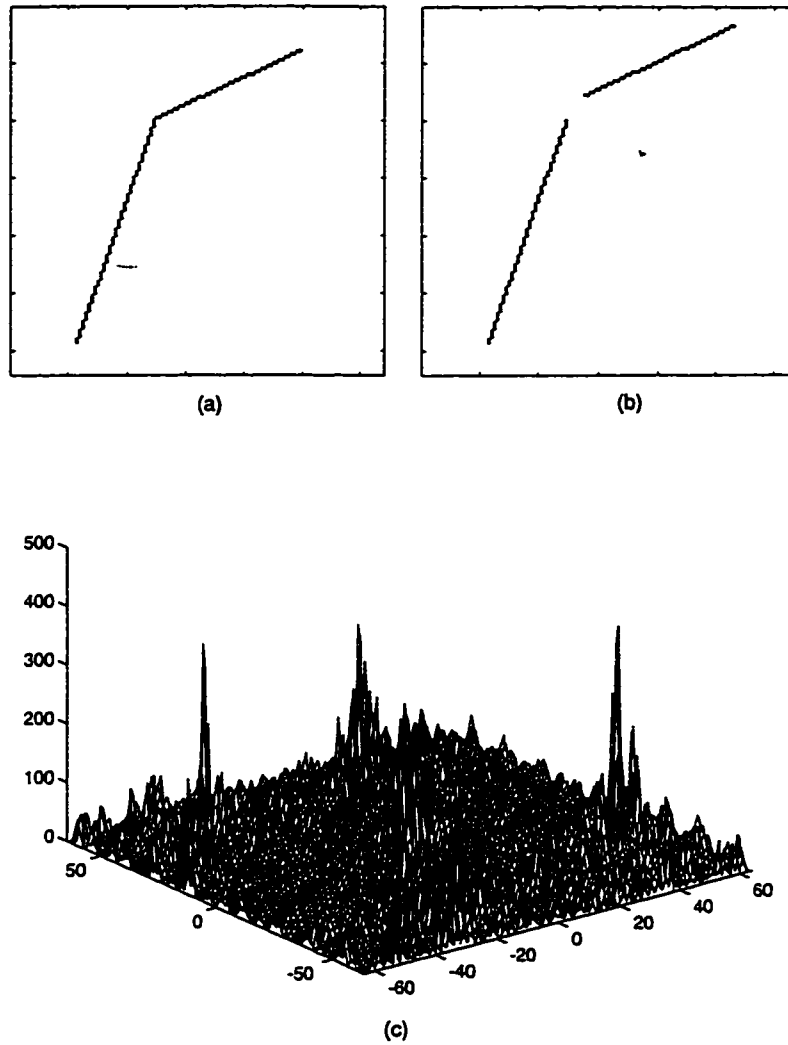


Figure 3.6: Frequency domain study of corners (a) image of a corner (b) input image of lines (c) surface plot of the difference of magnitude of Fourier transforms of (a) and (b)

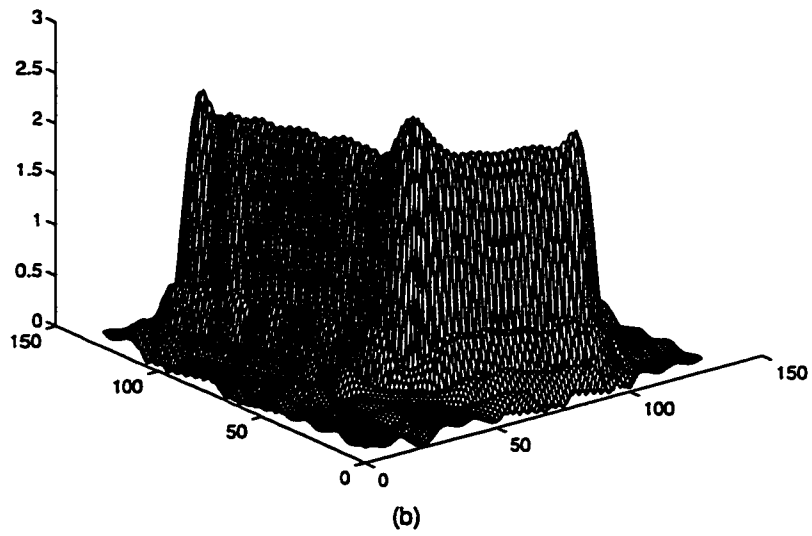
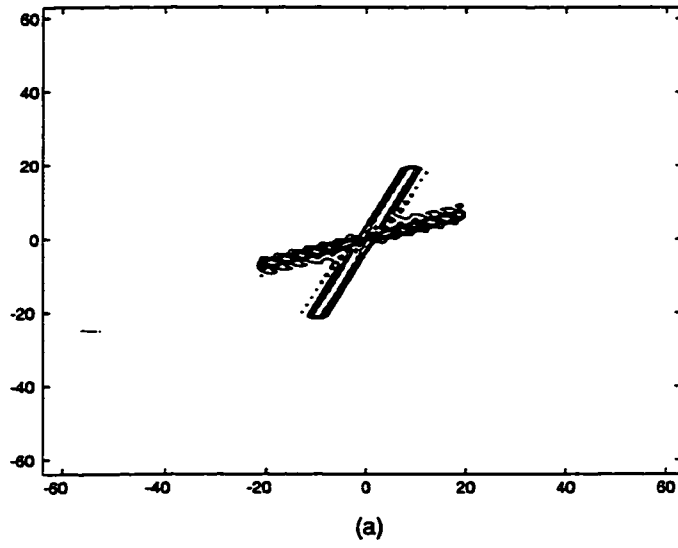


Figure 3.7: Frequency domain study of corners (a) contour plot of a mid section of the fourier transform of the corner model in the image shown in the previous figure (b) surface plot of the inverse Fourier transform

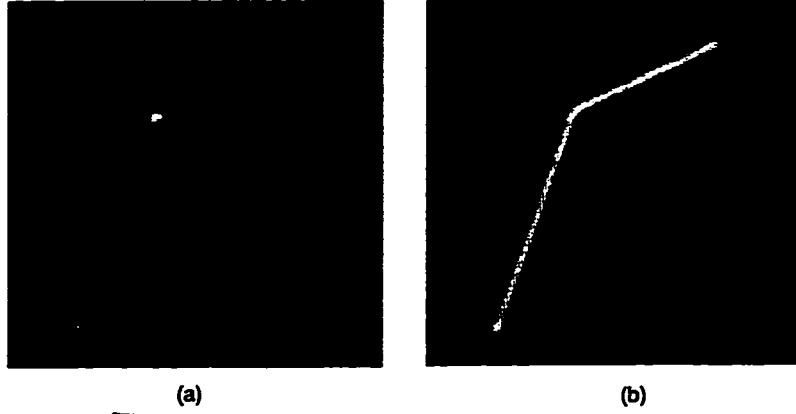


Figure 3.8: Recovered corner images (a) intensity plot of the surface plot shown in Fig. 3.5(b), (b) intensity plot of the surface plot shown in Fig. 3.7(b)

where $(x', y') = (x \cos \theta + y \sin \theta, -x \sin \theta + y \cos \theta)$ are rotated spatial-domain rectilinear coordinates and (U, V) give the particular 2-D frequency of the complex sinusoid $g(x, y)$, where

$$g(x, y) = \frac{1}{2\pi\sigma_x\sigma_y} \exp \left\{ -\frac{1}{2} \left[\left(\frac{x}{\sigma_x} \right)^2 + \left(\frac{y}{\sigma_y} \right)^2 \right] \right\} \quad (3.2)$$

where (σ_x, σ_y) characterizes the spatial extent and the bandwidth of $h(x, y)$. The Fourier transform of $h(x, y)$ is given as:

$$H(u, v) = \exp \left\{ -2\pi^2 \left[(\sigma_x [u - U]')^2 + (\sigma_y [v - V]')^2 \right] \right\} \quad (3.3)$$

where $([u - U]', [v - V]') = ((u - U) \cos \theta + (v - V) \sin \theta, -(u - U) \sin \theta + (v - V) \cos \theta)$ are rotated frequency-domain rectilinear coordinates, (U, V) is the center frequency of the complex sinusoid and (u, v) are frequency-domain rectilinear coordinates. When σ_x and σ_y are the same, the resulting filter is circularly symmetric and θ need

not be specified. When $\sigma_x \neq \sigma_y$, the resulting filter is elliptic and its major axis is oriented at an angle θ from the x-axis. Fig.3.9 shows surface plot and contour plot of one such filter with $\sigma_x = 1$, $\sigma_y = 4$ and $\theta = \pi/4$.

There are two important properties of the functions given in (3.1) and (3.3). First, these are the only functions that achieve minimum possible joint resolution in space and frequency. Second, the shapes of these functions resemble the receptive field profiles of the simple cells in the visual pathways [105].

This bandpass filter can easily be converted to a lowpass filter by substituting $U = V = 0$. Hence (3.1) and (3.3) results in a Gaussian shaped lowpass filter with the orientation according to θ . Now we drop the index x and y , and denote such a filter as $h(\sigma_x, \sigma_y, \theta)$. The response of the filter $y(x, y, \theta)$ is given as

$$y(x, y, \theta) = h(\sigma_x, \sigma_y, \theta) \star f(x, y) \quad (3.4)$$

where \star indicates 2-D convolution operation and $f(x, y)$ is the input image.

The Scale Interaction model requires that filter response be computed at two different scales and the difference between the responses will be the required output [82]. This makes the responses sensitive to line endings and, in general, changes in the curvature [81]. Such type of processing can be related to the behavior of endstopped (hypercomplex) cells in the visual cortex [81, 82]. In [82], the following model is used

$$q_{ij} = m(c_l.m(y_i(x, y, \theta)) - c_g.m(y_j(x, y, \theta))) \quad (3.5)$$

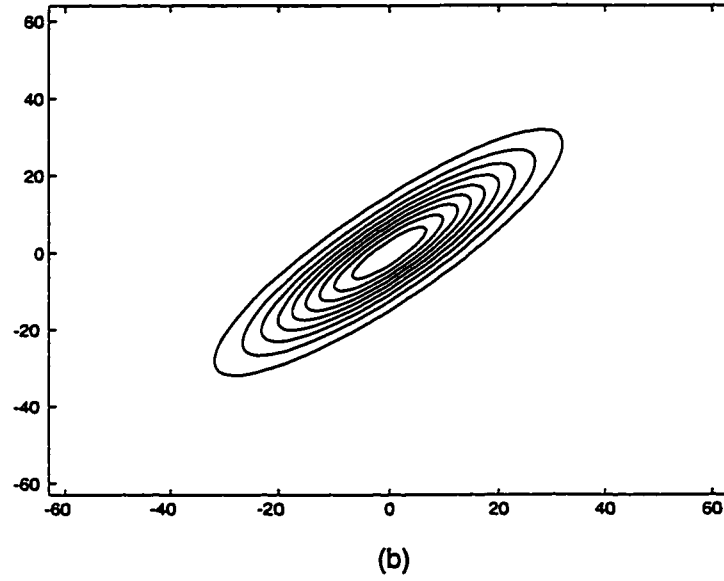
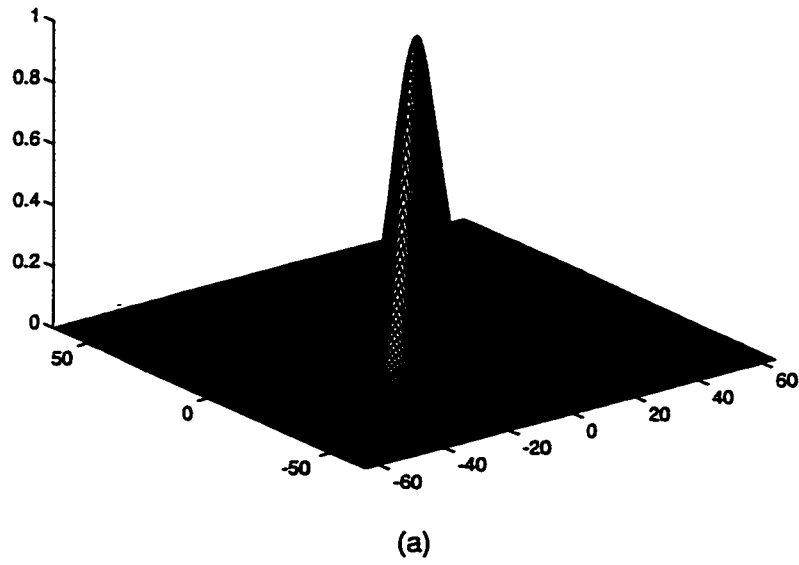


Figure 3.9: Frequency response of the Gabor filter with $\sigma_x = 1$, $\sigma_y = 4$ and $\theta = \pi/4$
(a) Surface plot (b) Contour plot

where $y_i(x, y, \theta)$ and $y_j(x, y, \theta)$ are the output of the filter at two scales 'i' and 'j'. $m()$ is the halfwave rectification function which is nonlinear and hence the model is highly nonlinear. The constants c_l and c_g are called gain constants. It is to be noted that in [81] a somewhat simplified model is used as

$$q_{ij} = m(y_i(x, y, \theta) - y_j(x, y, \theta)) \quad (3.6)$$

where $m()$ is a nonlinear function similar to a sigmoid function. Now, we define the difference impulse function, in the preferred orientation θ , as,

$$d_{ij}(\theta) = h(\sigma_{x_i}, \sigma_{y_i}, \theta) - h(\sigma_{x_j}, \sigma_{y_j}, \theta) \quad (3.7)$$

where $\sigma_{x_i}, \sigma_{y_i}, \sigma_{x_j}, \sigma_{y_j}$ determine various values of filter bandwidth. To ensure proper filtering, the filter characteristics of the two filtering function must be selected such that $\sigma_{x_i} < \sigma_{x_j}$ and $\sigma_{y_i} < \sigma_{y_j}$. In the proposed model, we do not employ nonlinearity and hence instead of filtering at two scales we simply compute the difference between the two impulse functions at different scales, and do the convolution only once. Here we intend to filter the input image with $d_{ij}(\theta)$ (where θ varies from 0 to π with equal intervals) and sum up the responses. Instead of filtering with different values of θ in $d_{ij}(\theta)$, we compute $d_{ij}(\theta)$ at different value of θ and linearly combine them into one filter function, which is possible due to the linearity property of our model. This gives us a huge amount of computational savings. Hence we end up with the single filter function p_{ij}

$$p_{ij} = \frac{1}{N} \sum_{k=1}^N d_{ij}(\theta_k) \quad (3.8)$$

where θ_k varies as $\theta_1, \theta_2, \dots, \theta_N$ in the orientation interval $[0, \pi]$. One such filter (p_{ij}) is shown in Fig. 3.10 in the frequency domain and its contour plot is shown in Fig. 3.11.

It should be noted here that p_{ij} is complex (since $h(x, y)$ is complex in (3.1)) and its frequency domain counterpart is real (from (3.3)). The magnitude response of this filter is given as

$$z(x, y) = | p_{ij} \star f(x, y) | \quad (3.9)$$

where, $f(x, y)$ is the input image. The only nonlinearity introduced by our model is the magnitude operator ($| \cdot |$) at the final output of the filter.

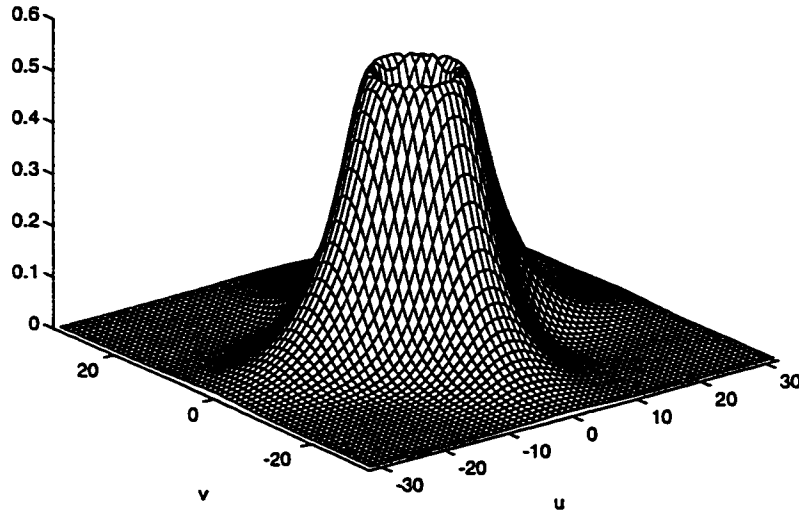


Figure 3.10: Frequency response of the filter with $\sigma_{x_i} = 1, \sigma_{y_i} = 2, \sigma_{x_j} = 3, \sigma_{y_j} = 4$ and $\theta_1 = 0, \theta_2 = \pi/2$

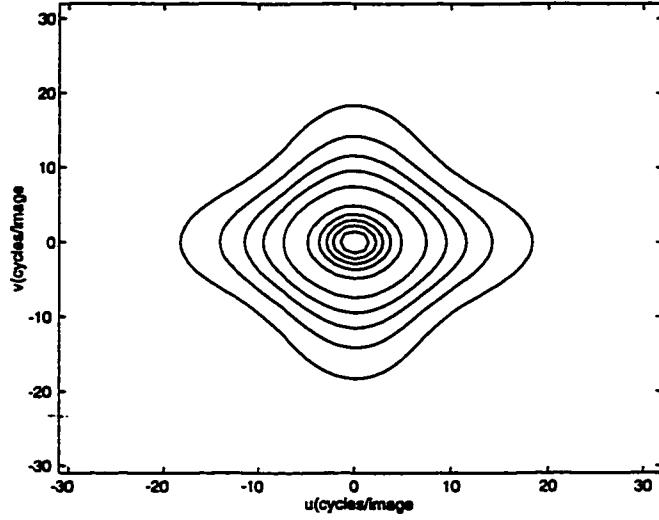


Figure 3.11: Contour plot of the frequency response of the filter

Since our objective here is to detect corners and since the filter function p_{ij} has a larger response at the curvature changes than at the straight edges [81], we do filtering iteratively in order to extract only the corners in the input image. Based on the study in Section 3.2, it follows that corners consist of frequencies very close to DC. The magnitude operator ($|\cdot|$) creates dc and high frequency components in a zero-crossing signal. It can be seen from Fig. 3.10 that the filter is designed to restrict DC as well as signals of high frequencies. Hence, repeated filtering and magnitude operation effectively removes signal at the edges much faster than at the corners. Hence, as the number of iteration increases, the change in the output gets progressively smaller. Thus, after applying the input image only once, the output is allowed to be fed back at the input and the process is repeated until the change in

the output is below a certain threshold. A flow chart representation of this iterative filtering scheme is illustrated in Fig. 3.12.

3.4 Simulation results and parameter selection

In this section we present the results of our scheme implemented using Matlab with an input image of size 128×128 . We took the input image, shown in Fig. 3.13(a), which consists of different angles at the corners with different sizes of edges. The filter was designed with $\sigma_{x_i} = 1, \sigma_{x_j} = 2, \sigma_{y_i} = 3, \sigma_{y_j} = 4$ and $\theta_1 = 0, \theta_2 = \pi/4, \theta_3 = \pi/2, \theta_4 = 3\pi/4$ with a region of support of size 128×128 . The 2-D convolution operation was implemented in frequency domain utilizing the power of FFT. The stopping criterion for the iterative filtering operation was assumed to be reached when the mean square value of the change in the output image was less than 0.001. The result after the convergence is shown in Fig. 3.13(b) where it can be observed that outputs at the corners are in the form of circular bright spots. The exact locations of the corners are at the center of these circular bright spots. In order to get these center-spots, we used the algorithm discussed in the following subsection.

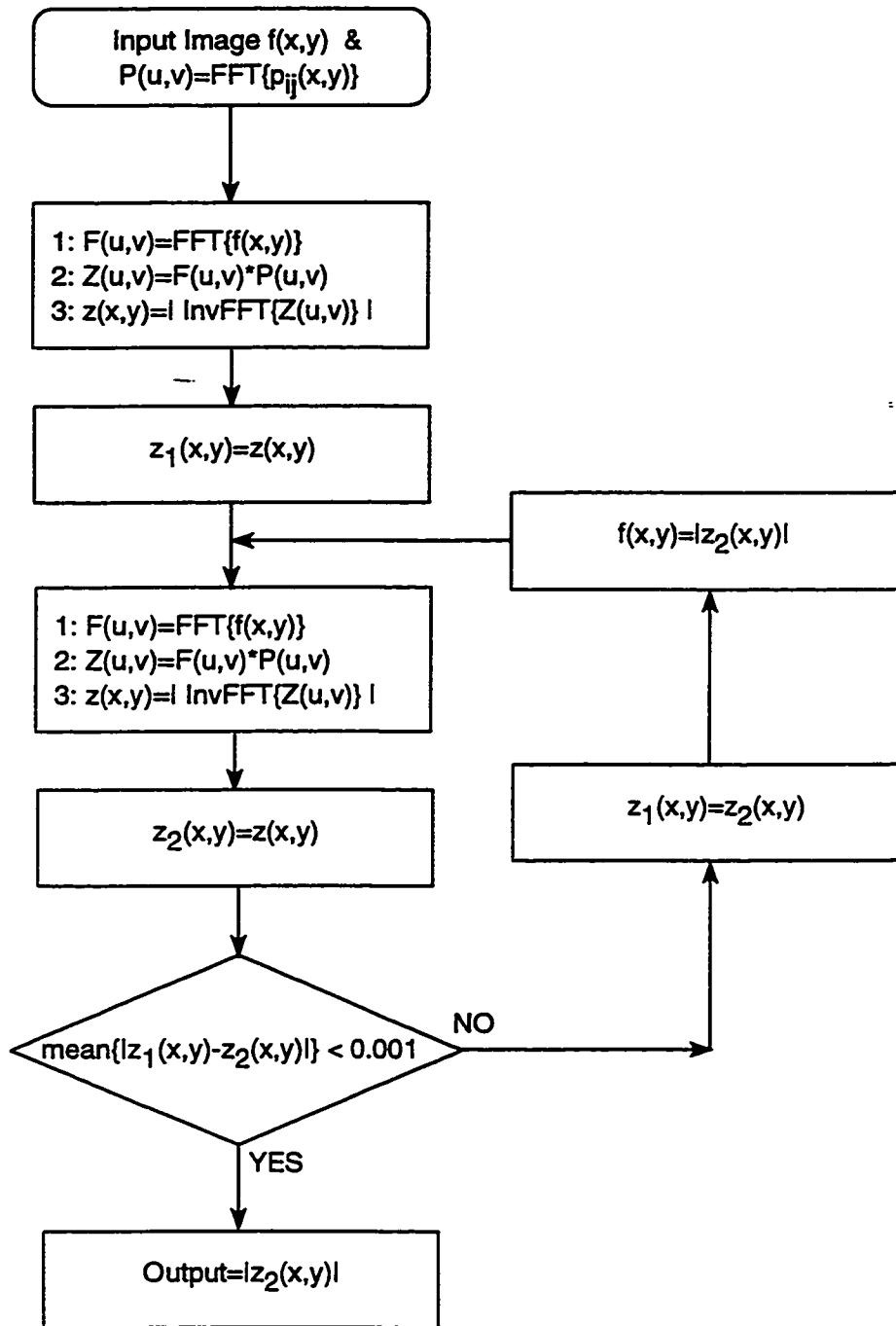


Figure 3.12: Flow chart representation of iterative filtering scheme

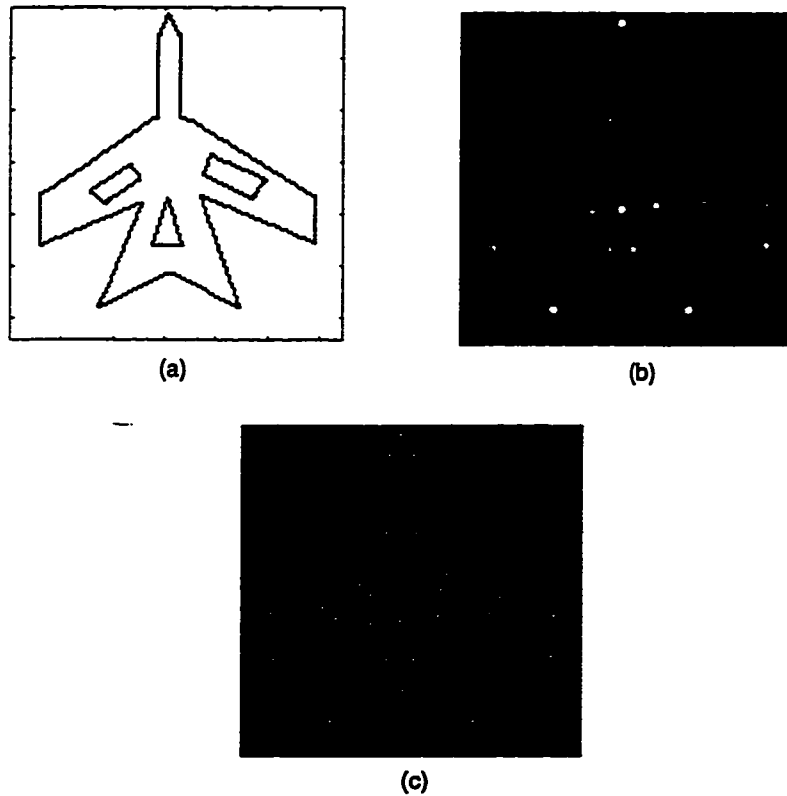


Figure 3.13: Results of processing (a) Input image (128×128) (b) Output of the filter after convergence (c) Extracted corners

3.4.1 Extraction of corner points

Fig. 3.13(b) shows that corner points are located at the center of the circular bright spots. Another point to be noted here is that the response is not the same for all corners. In this algorithm we consider a spot to be a correct representative of the corner if its amplitude is greater than 40% of the maximum peak in the response. This threshold is selected after testing with large number of test images. There are various techniques to locate the center points from these bright spots. Here, we have

used a technique similar to maxima filtering as follows:

Step 1: Find the maximum value of the output and let it be M .

Step 2: Find the location of the maximum output and let it be (x_m, y_m) .

Step 3: If the response at this point is greater than the $0.4M$ consider this point a valid corner. Otherwise, exit the algorithm.

Step 4: Replace a neighborhood of the corner detected in Step 2 with zeros in the output of the filter. (In our case we took ± 3 pixels of the corner point).

Step 5: Goto Step 2.

The result of the above algorithm is shown in Fig. 3.13(c).

3.4.2 Simulation Study

In order to study the behavior of this technique, a comprehensive simulation is provided here. Now we provide step by step operation of the filtering operation. For the sake of explanation, the filter response is computed at two different scales and the difference between the two responses is taken as the final output. In actual practice, however, we compute the difference impulse function and do the filtering once. Fig. 3.14 shows the input image and its surface plot. Fig. 3.15 shows the responses (using (3.4)) with two different values of σ 's. Fig. 3.16(a) shows the difference of the responses shown in Fig. 3.15(a) and (b). Fig. 3.16(b) shows the difference response after the second filtering iteration. Fig. 3.17(a) and (b) shows the difference response after the third and fourth iteration, respectively. Here, we

observe that the ratio between responses at the corners and the responses at the edges increases with more filtering. The overall response, however, decreases with more filtering which is due to the loss of gray levels. This problem can be tackled by rescaling the filtered response after each iteration.

Since there are four parameters ($\sigma_{x_i}, \sigma_{x_j}, \sigma_{y_i}$ and σ_{y_j}) involved, these parameters will lead to a huge number of filters to be tried. In order to reduce this problem, we define two new parameters as

$$\alpha = \sigma_{x_i} \quad (3.10)$$

and

$$\beta = \sigma_{y_j} - \sigma_{y_i} \quad (3.11)$$

And we take

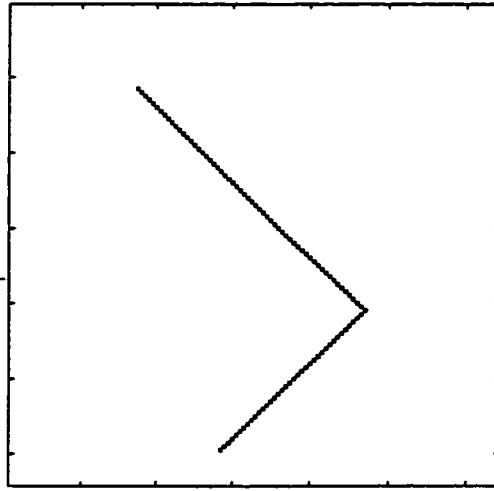
$$\frac{\sigma_{y_i}}{\sigma_{x_i}} = \frac{\sigma_{y_j}}{\sigma_{x_j}} = \kappa$$

where κ is a constant.

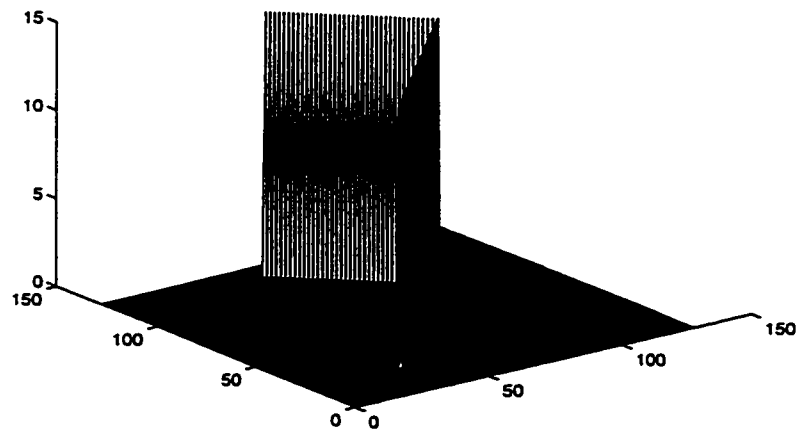
Hence, all the four parameter can now be calculated from various values of α and β thereby reducing the dimensionality of the parameters. More precisely, here α provides a measure of the spatial extent of the filter and β provides a measure of the difference between the bandwidths.

Now, in order to measure the performance of our corner detection scheme we further define (similar to [106]):

$$Recall = \frac{CDC}{(CDC + MC)} \quad (3.12)$$

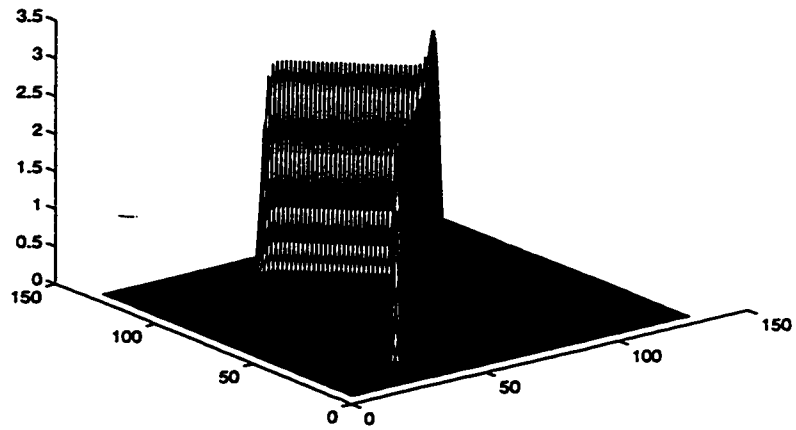


(a)

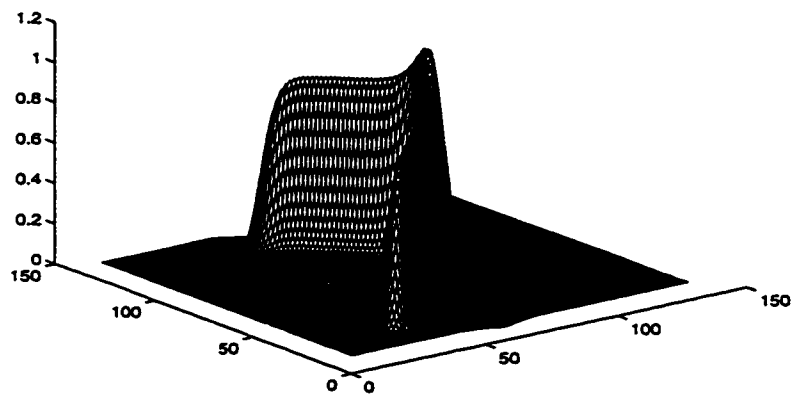


(b)

Figure 3.14: (a) Input image 128×128 (b) Surface plot of the image



(a)



(b)

Figure 3.15: (a) Filtered response with $\sigma_x = 1$ and $\sigma_y = 2$ (b) Filtered response with $\sigma_x = 3$ and $\sigma_y = 6$

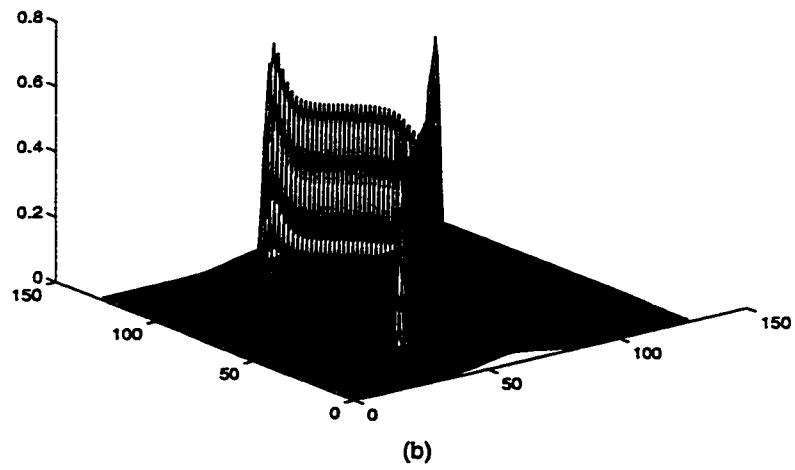
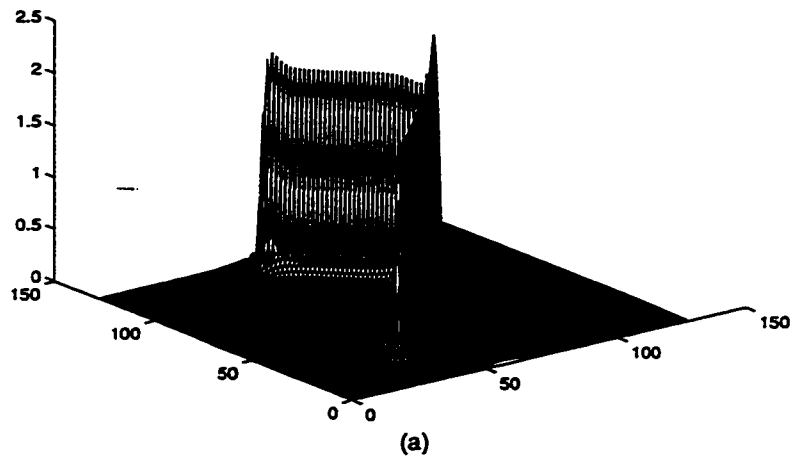


Figure 3.16: (a) Difference response (b) Difference response after the second filtering iteration

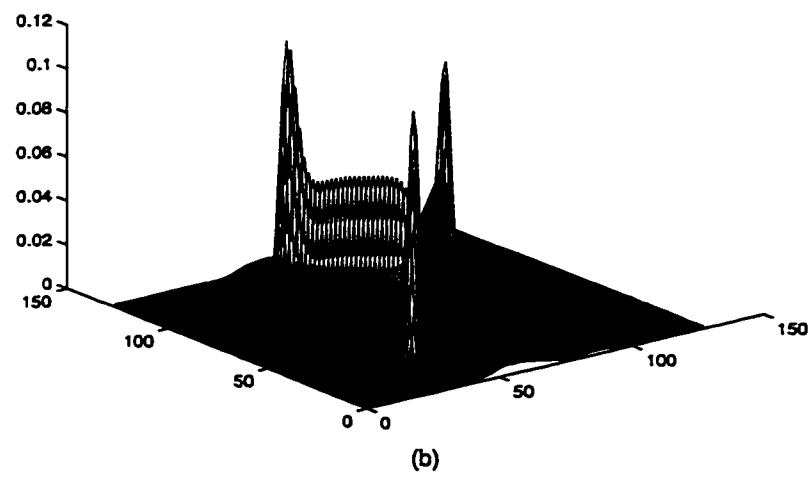
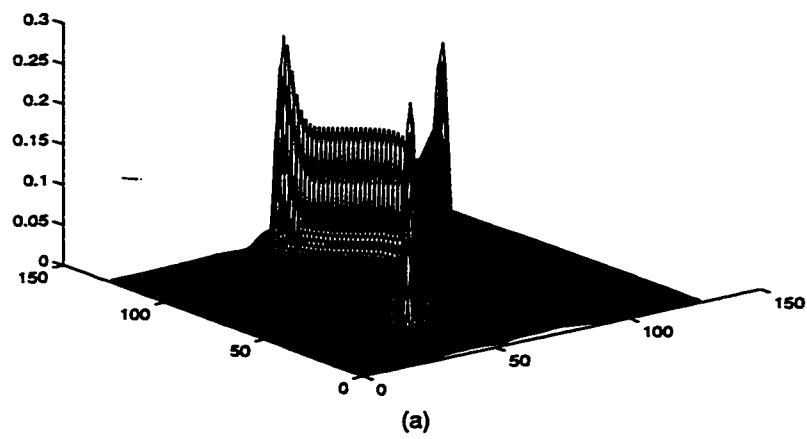


Figure 3.17: (a) Difference response after the third filtering iteration (b) Difference response after the fourth filtering iteration

and

$$Precision = \frac{CDC}{(CDC + FC)} \quad (3.13)$$

where *CDC* is the number of **C**orrectly **D**etected **C**orners, *MC* is the number of **M**issing **C**orners and *FC* is the number of **F**alse **C**orners. Here, the overall performance measure of the corner detection scheme will be taken as

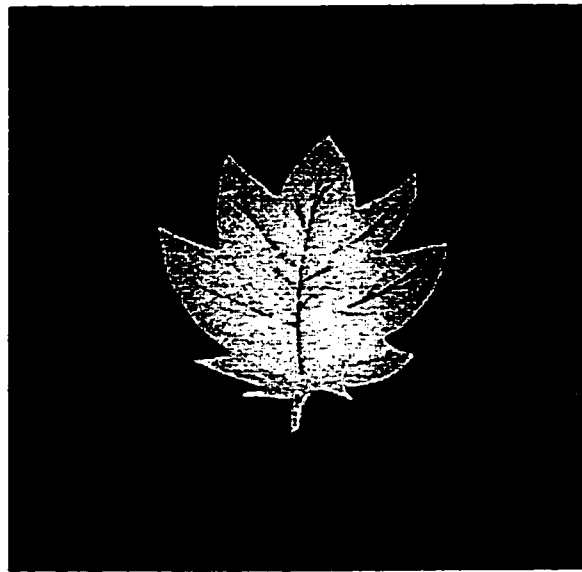
$$Goodness = \frac{Recall + Precision}{2} \quad (3.14)$$

The variation of the Goodness measure with varying values of α and β with $\kappa = 2$. Here for each image α and β are varied from 0.1 to 4 in steps of 0.1. Hence sixteen hundred experimants were carried out for each image and the results are reported as follows:

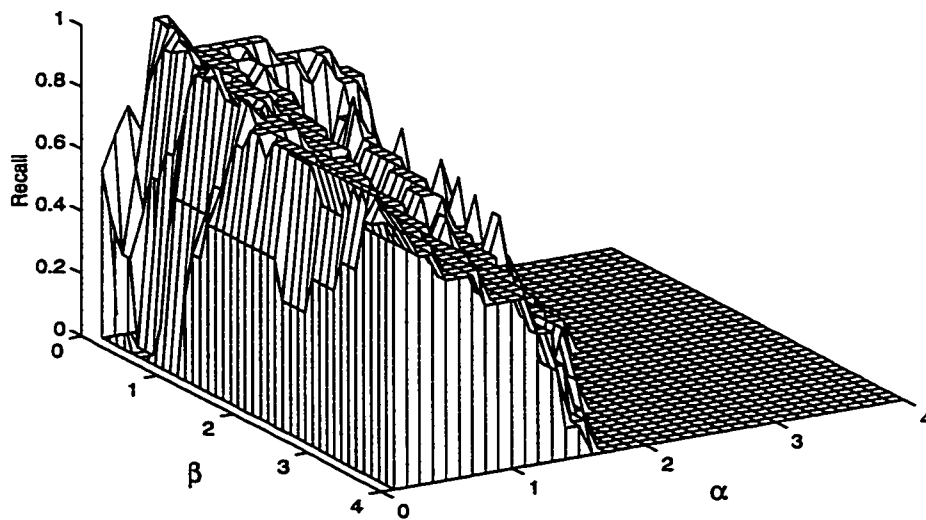
For the gray level image (256×256) shown in Fig.3.18(a), the profiles of *Recall*, *Precision* and *Goodness* are shown in Figures 3.18(b), 3.19(c) and 3.19(d), respectively, with various values of α and β . Another set of these profiles for gray level image (Fig. 3.20(a)) is shown in figures 3.20 and 3.21.

For the binary line drawing image (128×128) shown in Fig.3.22(a), the profiles of *Recall*, *Precision* and *Goodness* are shown in Figures 3.22(b), 3.23(c) and 3.23(d) respectively, with various values of α and β .

For the binary image (128×128) shown in Fig.3.24(a), the profiles of *Recall*, *Precision* and *Goodness* are shown in Figures 3.24(b), 3.25(c) and 3.25(d) respectively, with various values of α and β .



(a)



(b)

Figure 3.18: (a) Gray level input image 256×256 (b) Recall profile for various values of α and β

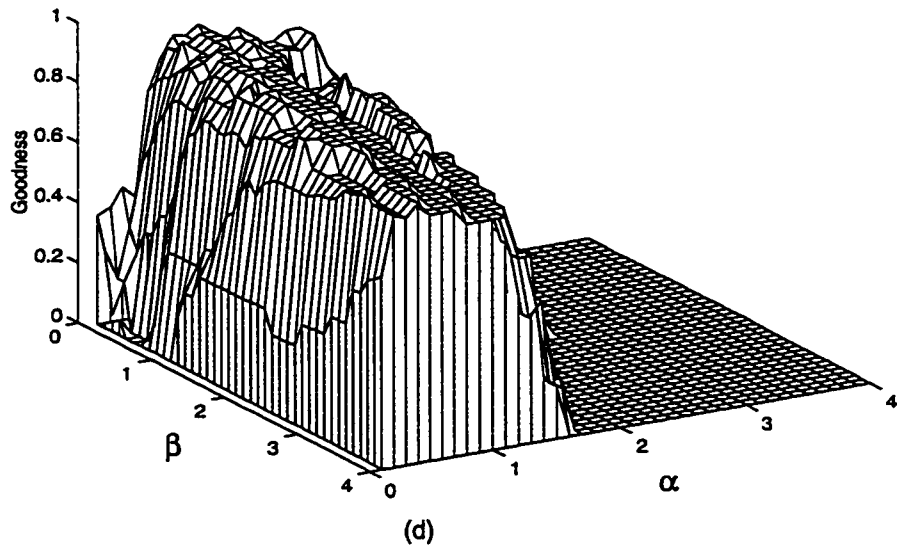
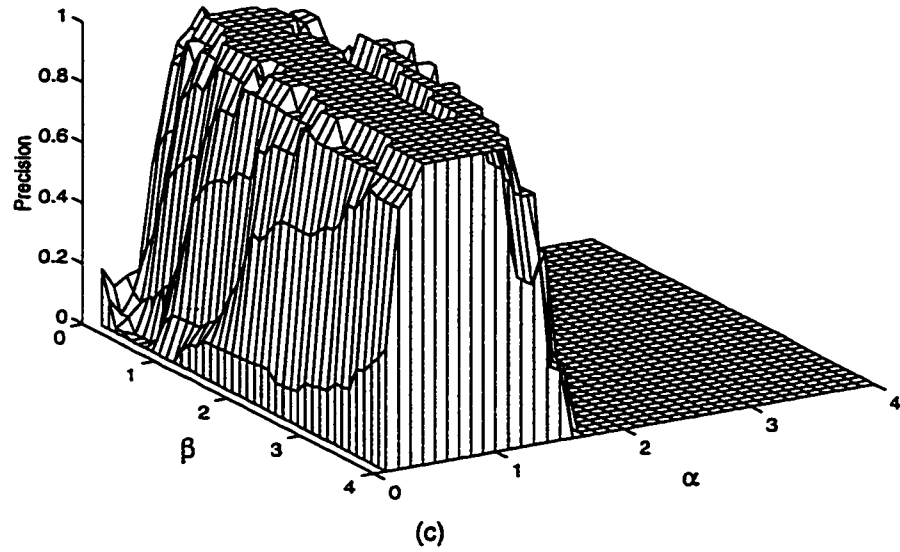
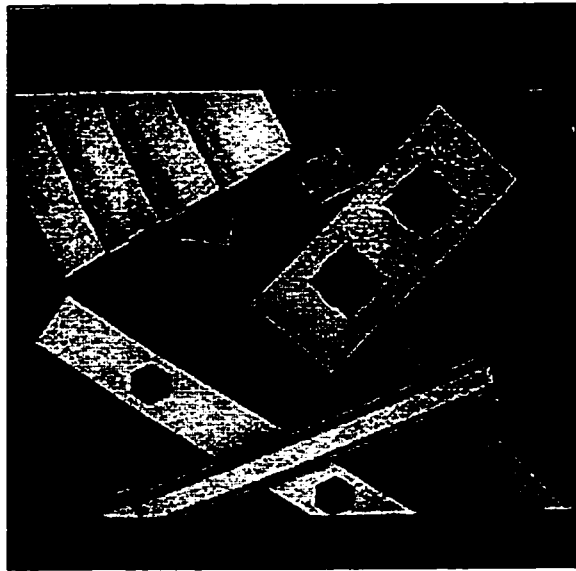
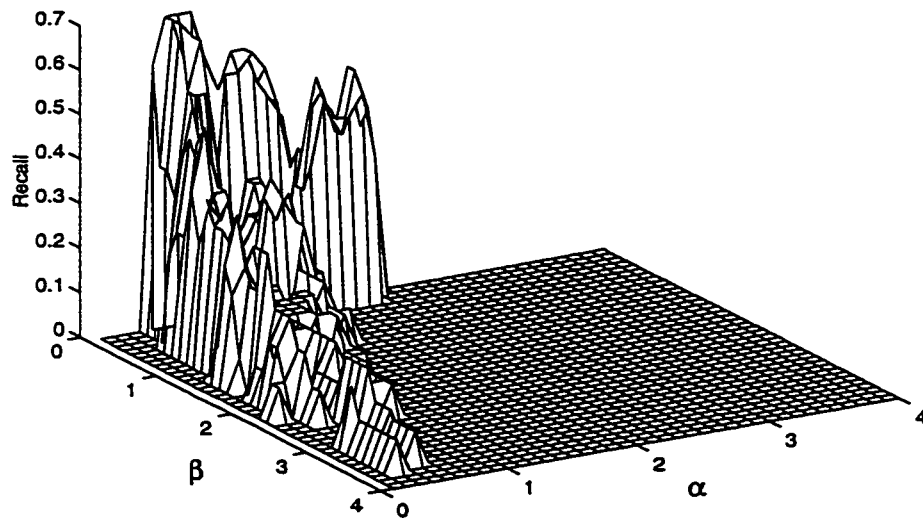


Figure 3.19: For the image shown in the previous figure: (c) Precision profile for various values of α and β (d) Goodness profile for various values of α and β



(a)



(b)

Figure 3.20: (a) Gray level input image 256×256 (b) Recall profile for various values of α and β

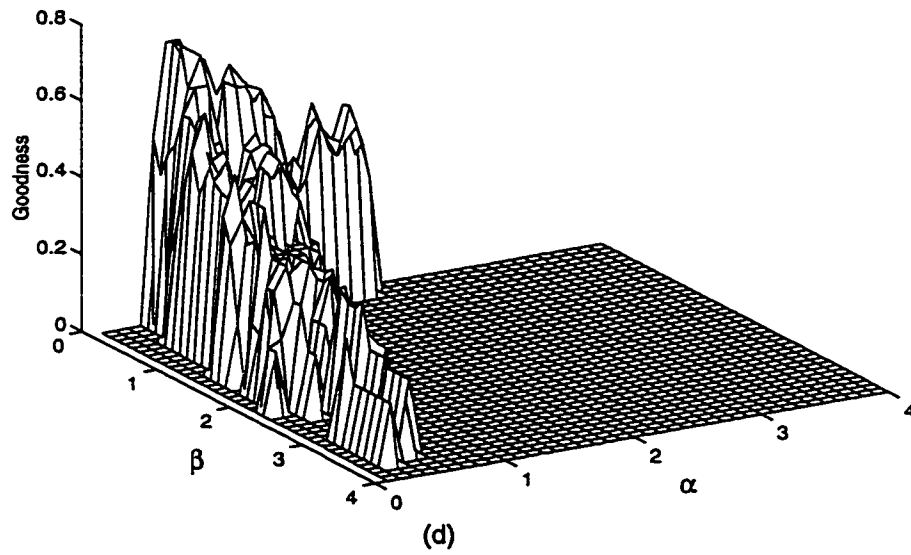
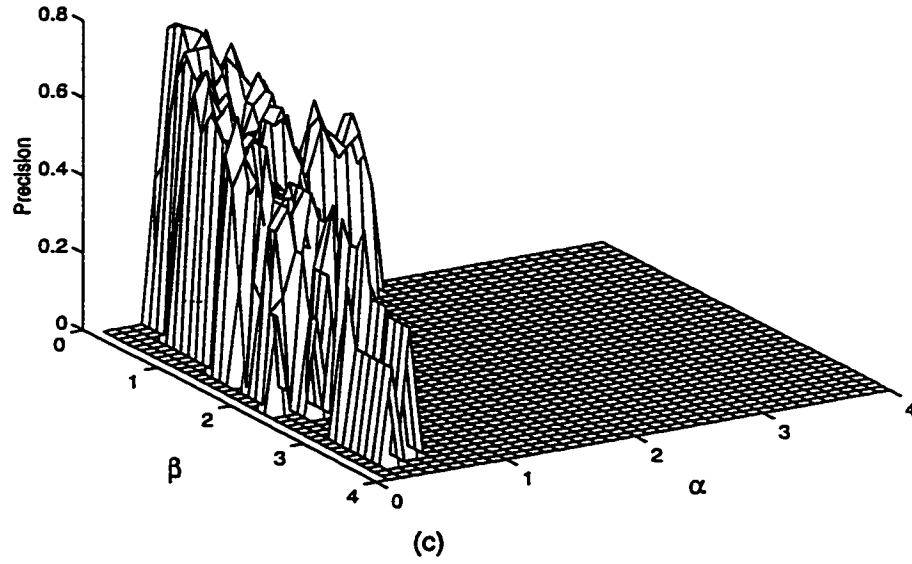
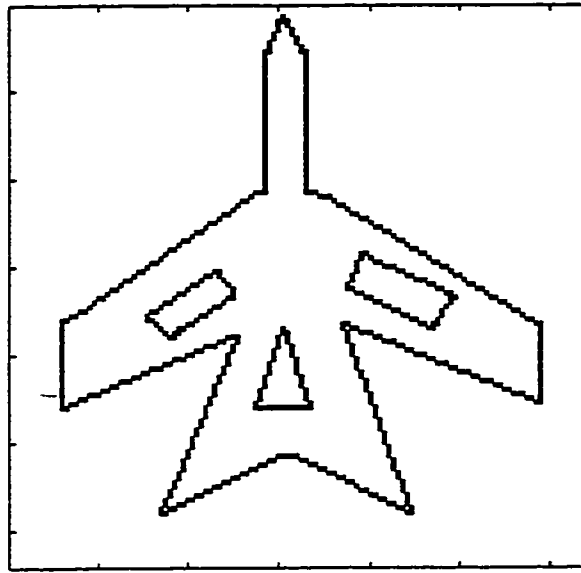
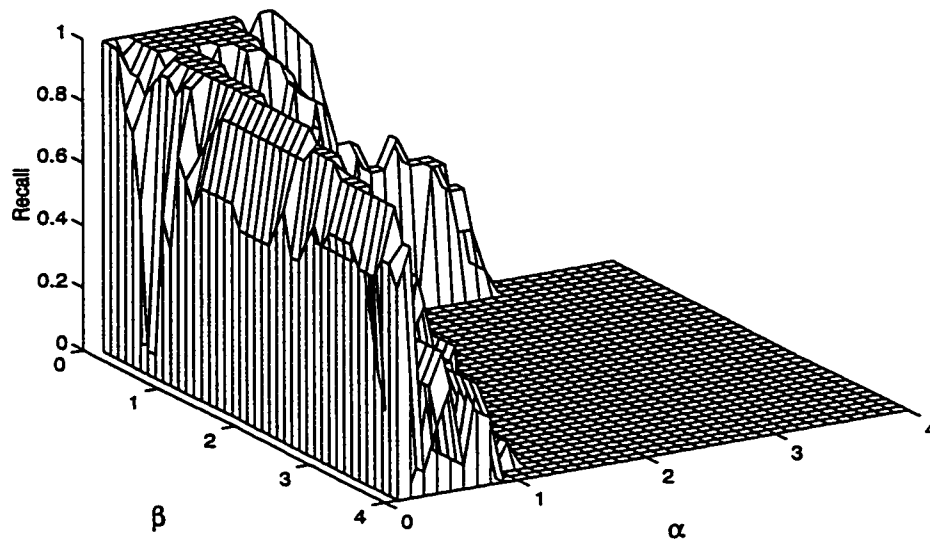


Figure 3.21: For the image shown in the previous figure: (c) Precision profile for various values of α and β (d) Goodness profile for various values of α and β



(a)



(b)

Figure 3.22: (a) Binary line drawing input image 128×128 (b) Recall profile for various values of α and β

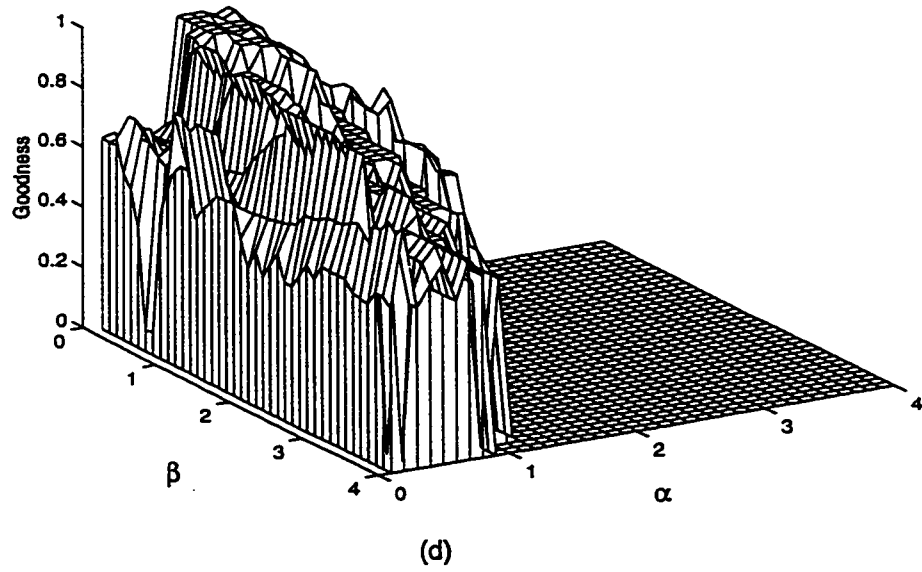
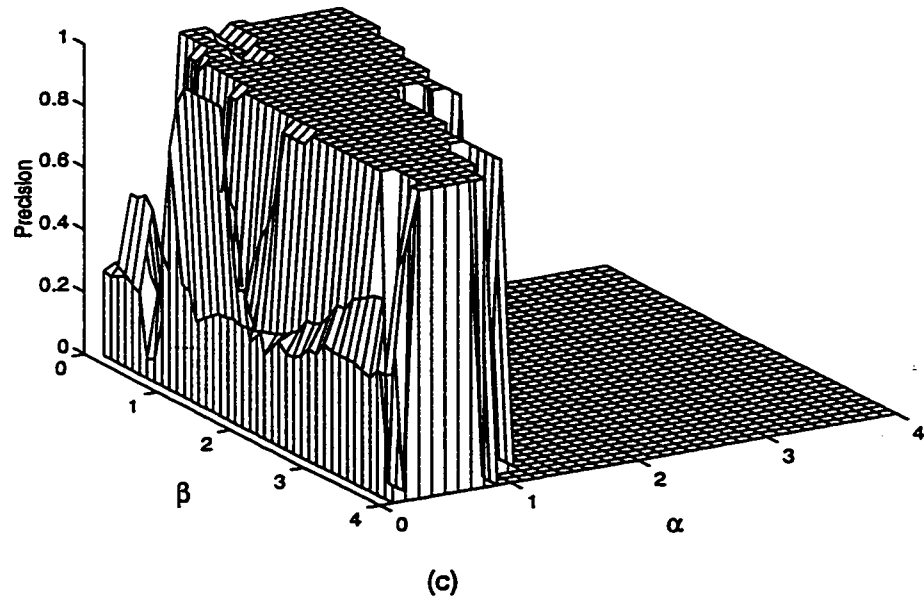
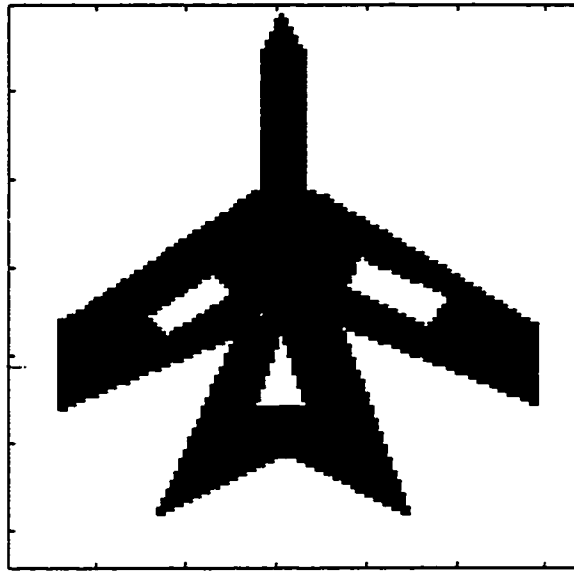
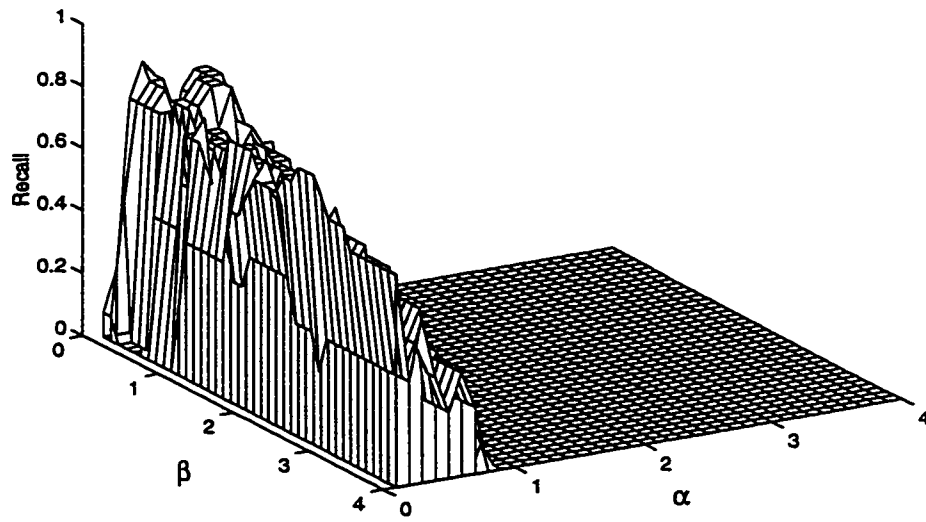


Figure 3.23: For the image shown in the previous figure: (c) Precision profile for various values of α and β (d) Goodness profile for various values of α and β



(a)



(b)

Figure 3.24: (a) Binary input image 128×128 (b) Recall profile for various values of α and β

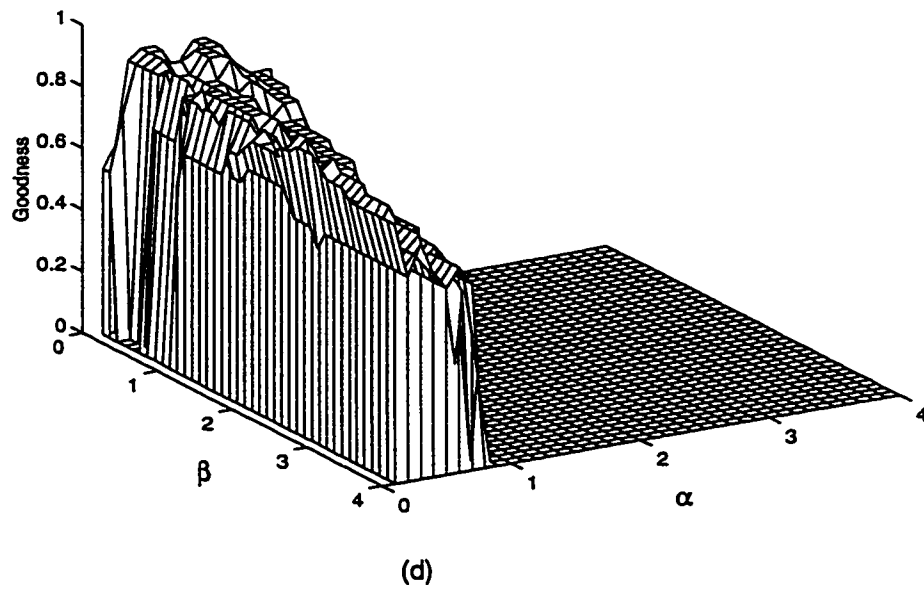
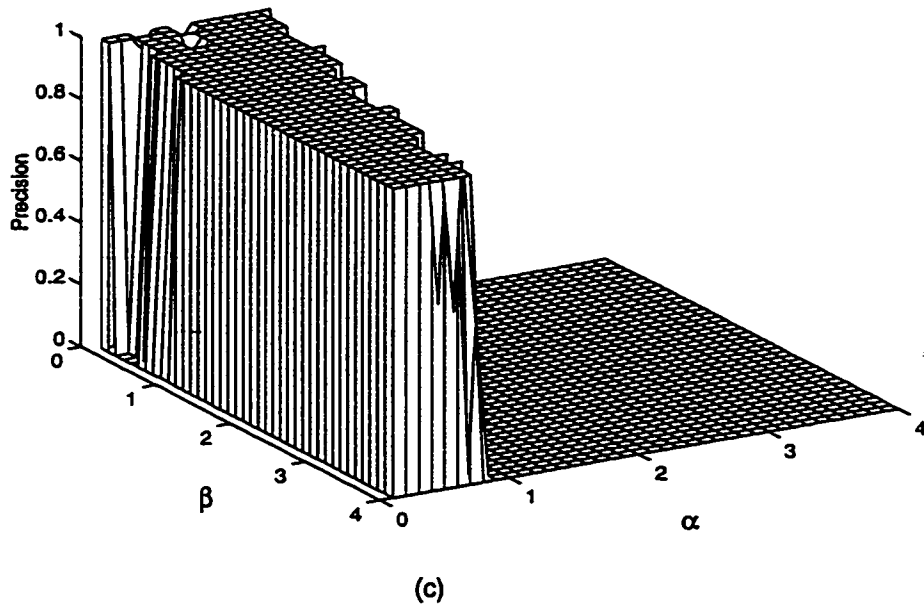


Figure 3.25: For the image shown in the previous figure: (c) Precision profile for various values of α and β (d) Goodness profile for various values of α and β

For all the test images, maximum performance is achieved for α and β somewhere between 0.2 and 1.0.

Profile of iterations for various values of α and β for line drawing image (Fig. 3.22(a)) is shown in Fig. 3.26. Similar profile were observed for other sample images.

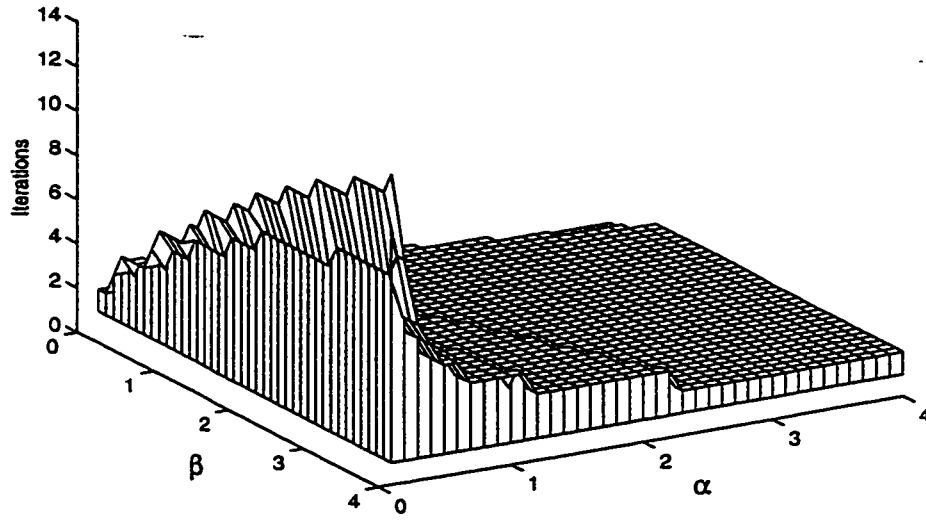


Figure 3.26: Profile of iterations for various values of α and β

3.4.3 Comparison

Singh and Shneier [78] proposed a good corner detection scheme using a novel combination of both template and gradient based approach. They also used practical gray level images for evaluation. Here we used the same images to compare our results with their results. From Fig.3.27 and Fig.3.28, we observe that the proposed

technique outperforms the technique [78] in terms of positional accuracy and false detection.

3.4.4 Detection Under Noise

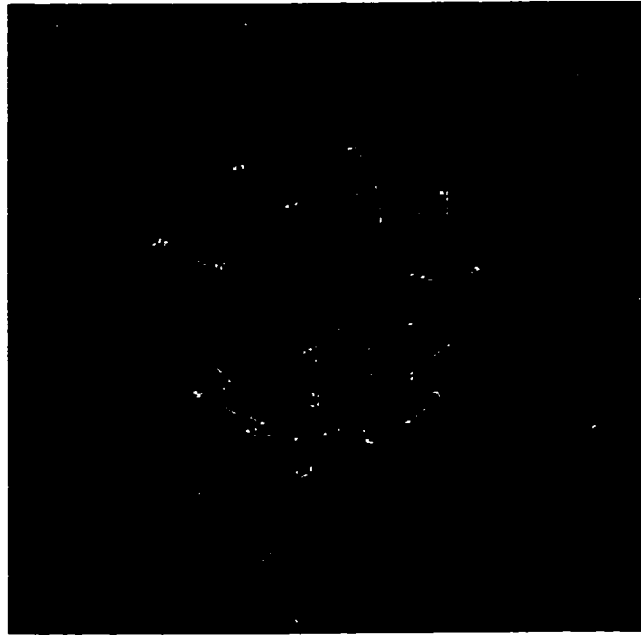
Proposed corner detection scheme has also been tried for noisy images with AWGN noise. Fifteen images were synthesized with corners at varying angles (at 10, 20, 30, 45, 60, 70, 80 90, 100, 110, 120, 135, 150, 160 and 170 degrees). Each one was subjected to varying degree of noise. For each value of signal to noise ratio (SNR) and angle ten experiments with proposed corner detection algorithm were conducted. Fig. 3.29 shows the results of these experiments. Here we observe that at smaller angles (sharp corners) the performance is best but as the angle increases the performance deteriorates. This is also demonstrated in Fig. 3.30. Here *Probability of Detection* is defined as the probability of the correct detections in 100 experiments. For the sake of reader's information, Fig. 3.29 was obtained after 69000 experiments!!

Here SNR is measured as

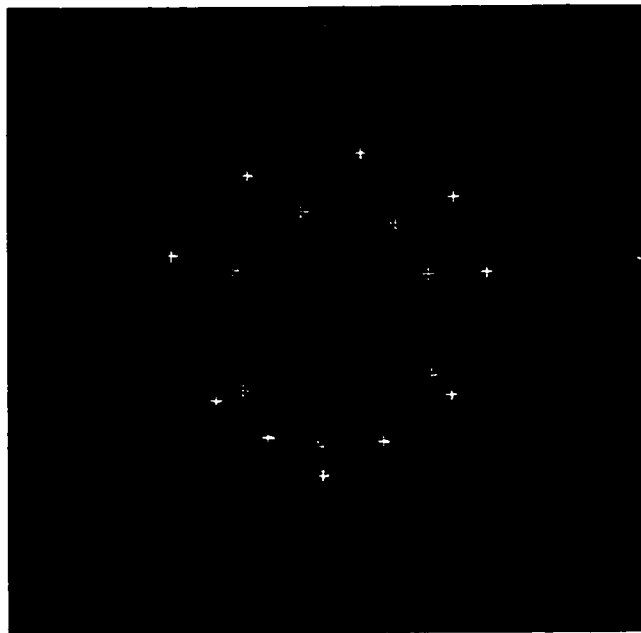
$$SNR = 10\log_{10} \left(\frac{\text{Power of signal}}{\text{Power of noise}} \right) \quad (3.15)$$

$$= 10\log_{10} \left(\frac{\sum_x \sum_y f(x,y)^2}{\sum_x \sum_y n(x,y)^2} \right) \quad (3.16)$$

Fig. 3.31 shows the *Goodness* with respect to the signal to noise ratio (SNR) of the gray level image shown in Fig. 3.19(a). Here we observe that, in general, the

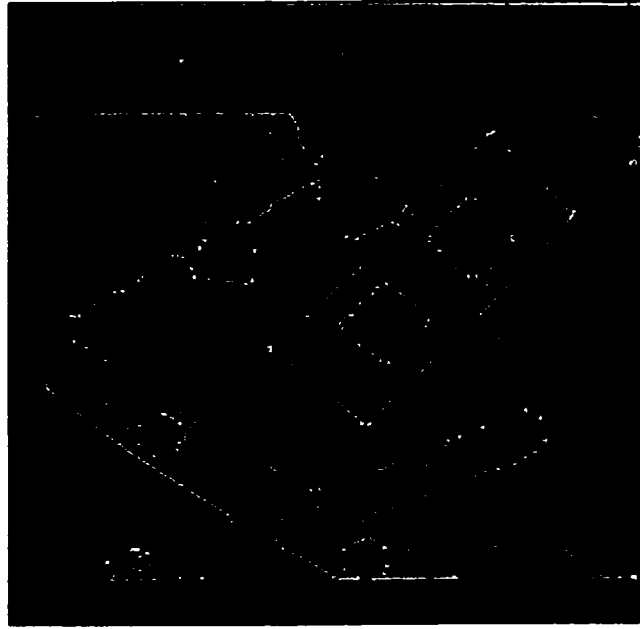


(a)

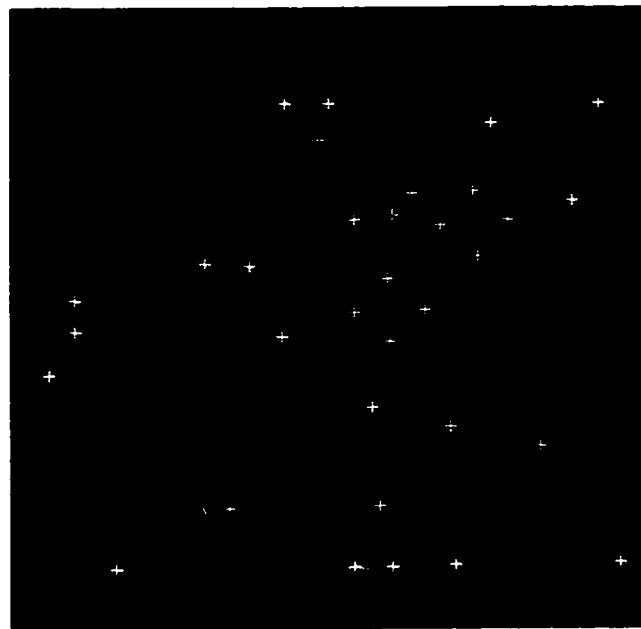


(b)

Figure 3.27: (a) Result obtained by Singh and Shneier (b) Result obtained by present approach ($\alpha = 0.6$ and $\beta = 1.1$)

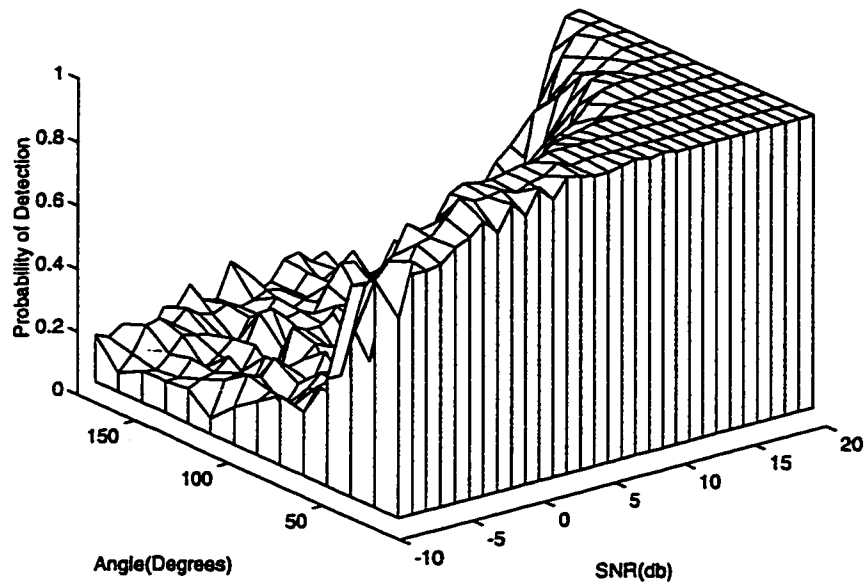


(a)

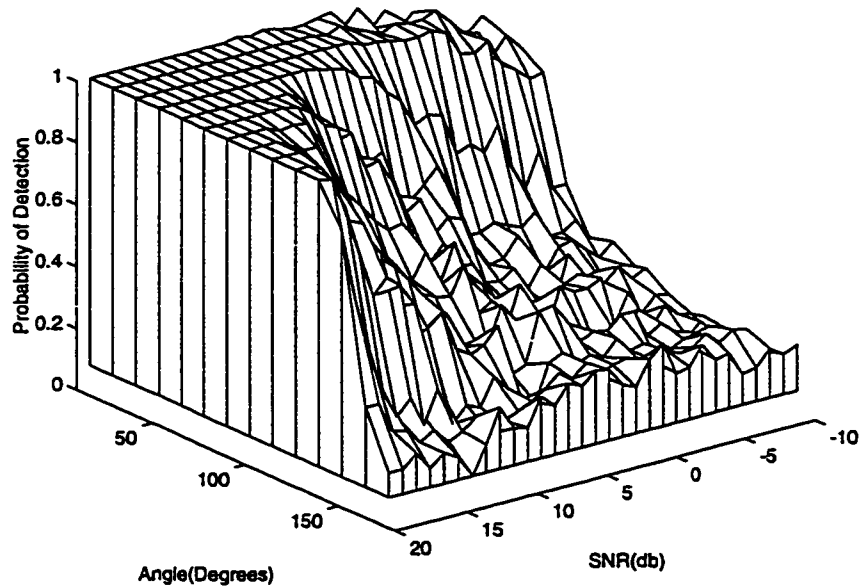


(b)

Figure 3.28: (a) Result obtained by Singh and Shneier (b) Result obtained by present approach ($\alpha = 0.4$ and $\beta = 1.0$)



(a)



(b)

Figure 3.29: Probability of Detection with various values of angles and signal to noise ratios (SNR) where (a) and (b) are two views of the same plot

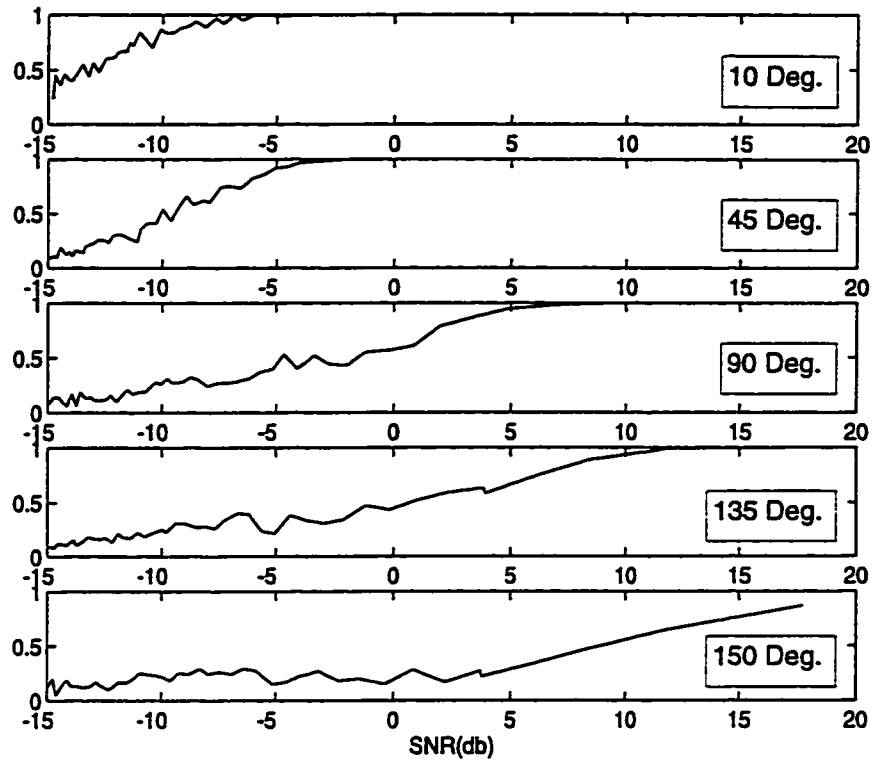


Figure 3.30: Probability of Detection with various values of angles and signal to noise ratios (SNR)

Goodness improves with higher SNR. *Goodness* reaches its maximum when SNR is above 15 db level. For the binary line drawing image (Fig. 3.22(a)), the best performance is achieved when SNR is above 5 db. For the similar binary image (Fig. 3.24(a)) the best performance is achieved when SNR is above 14 db.

3.4.5 Sensitivity with other parameters

Here we briefly describe the results of the variations with other parameters as follows:

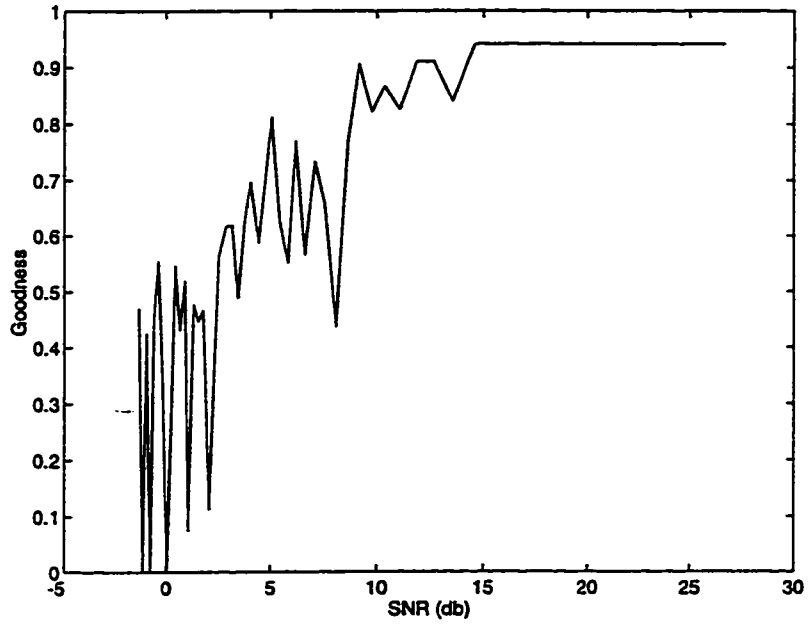


Figure 3.31: Goodness under noise for the gray level image shown in Fig. 3.18(a)

1. The ratio between major and minor axis of the elliptical profile (κ) is tested with other values (than 2) and no noticeable variation in the overall result is observed.
2. The interval between the different values of θ is varied and no noticeable variation in the overall result is observed.

3.5 Conclusions

A corner detection technique which is suitable for both binary and gray level images, without requiring tracking the object contour, has been proposed. It is directly

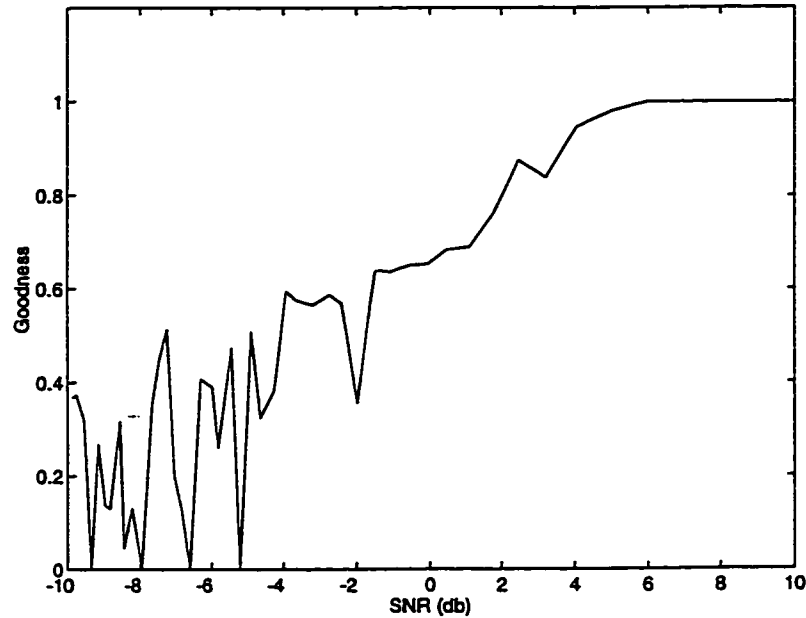


Figure 3.32: Goodness under noise for the binary line drawing image shown in Fig. 3.22(a)

applicable to multiple objects and under occlusion (see Fig. 3.28(b)). It also detects line intersections and line endings. This technique gives acceptable results under noise with SNR more than 10 db. It is robust in the sense that it is suitable for both hot and cold objects in addition to being suitable for both binary and grey level images. This technique has the limitation that it misses the corner points when angle at the corner is large (see Fig. 3.28(b)). We have also studied its performance under AWGN noise. We have defined a new performance measure with respect to missing and false corners. As far as speed is concerned, this technique took only 1 to 2 sec to process the image of size 256×256 on Pentium Pro Processor (166MHz) running under Matlab (version 4.2C) environment. Significant improvement in the

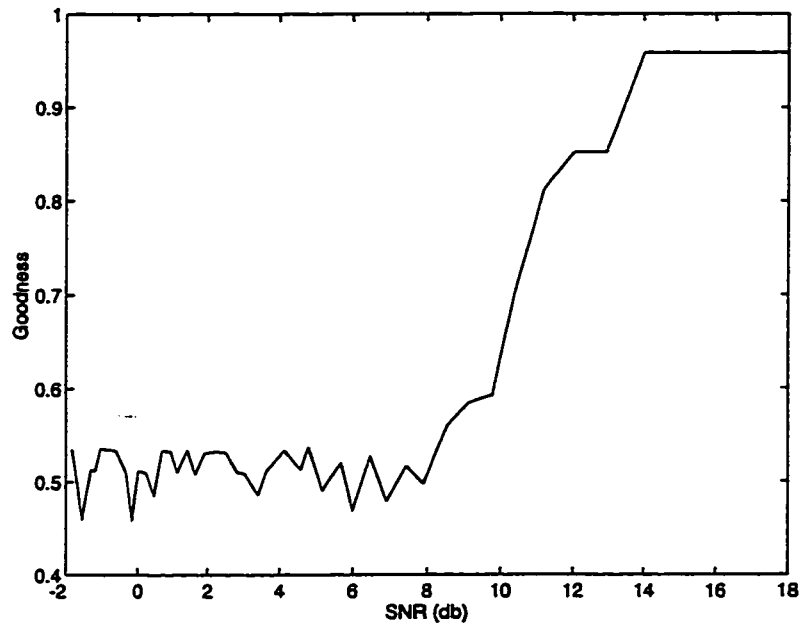


Figure 3.33: Goodness under noise for the binary image shown in Fig. 3.24(a)

speed is expected when this technique is implemented as a stand alone application. Part of this work has already been presented in [104]. Following is the list of contributions:

1. *A study of corners in frequency domain is presented.*
2. *A novel Gabor Filter-based corner detection algorithm is proposed which is computationally efficient.*
3. *A technique is also presented to extract corners from filtered image.*
4. *Extensive simulation results with the proposed technique is presented.*
5. *This technique does not require preprocessing.*

6. *This technique is suitable for both binary and gray level images and also can be applied directly to images containing multiple and occluded objects. This technique does not require any changes for both hot and cold objects.*
7. *New performance measures are also given for the evaluation of corner detection schemes.*
8. *Performance under AWGN noise is also presented.*

Chapter 4

CORNERS AND SMOOTH JOINS USING WAVELET TRANSFORM

4.1 Introduction

A multiresolution representation provides a simple hierarchical framework for interpreting the input image information [10]. In the literature, scale-space based techniques are used for developing multiscale corner detection algorithms [42, 93, 40, 94]. Wavelet theory provides a unified framework for a number of techniques which had been developed independently for various signal processing applications. Also there exist efficient algorithms to compute wavelet transforms using subband filtering

techniques. Despite its advantages, it has not been fully explored in the area of computer vision. Recently, some work has been reported on boundary and surface representation using wavelet transform [107, 108, 109]. Few results have also been reported regarding the use of wavelets for corner detection such as [95, 96]. The detection of corners, inflection and smooth joins together using single wavelet, however, has not been attempted by previous authors. There have been attempts to solve this problem using linear approximation [74]. These techniques, however, lack the advantages of multiresolution analysis.

4.2 Assumptions Regarding Preprocessing

All techniques for feature detection from the shape of the object boundary require some preprocessing of the input image. This preprocessing includes

- extraction of object silhouettes,
- edge detection,
- thresholding,
- separating objects (if there are multiple objects), and
- boundary tracking.

In addition to the considerable computation involved, these steps require selection of appropriate algorithms. This selection depends upon the expected background

noise, the operating environment (lighting arrangements and nature of the objects etc.), the quality and setting of camera (mono/stereo, contrast, viewing angles etc.) and the computational overhead, which is again constrained by the overall speed requirement of the system. The speed requirement again heavily depends upon the available computing platform which along with the other subsystems determine a significant part of the cost of the overall system.

Here it is assumed, as has been done by almost all the authors, that these preprocessing steps have been done properly and with the least possible cost. Hence, after tracking the boundary of the planar object, the boundary information is represented in parametric form as

$$C = \{x(t), y(t), t = 1, \dots, n\} \quad (4.1)$$

where t is the index of the boundary pixels.

4.3 Computation of Curvature Information

The boundary information in parametric form is useful only when proper information of the boundary curvature is obtained. In the literature, there are mainly three types of measures that are employed for the curvature analysis of planar 2-D objects. These representations reduce the dimensionality of the problem from a 2-D object contour to a 1-D signal that has the rotation invariance property.

4.3.1 Curvature Function

The *curvature function* is defined as the derivative of the slope with respect to the arc length (t). It can be defined in terms of the derivative of the functions $x(t)$ and $y(t)$ as [42]

$$CF(x, y) = \frac{\frac{\partial^2 y}{\partial x^2}}{\left[1 + \left(\frac{\partial y}{\partial x}\right)^2\right]^{3/2}} \quad (4.2)$$

Furthermore, the functions $x(t)$ and $y(t)$ must be related by

$$\frac{\partial x}{\partial t} = \cos\psi \quad \frac{\partial y}{\partial t} = \sin\psi$$

where ψ indicates the orientation of the tangent along the curvature. Hence, after few mathematical manipulations, it yields the curvature expression given by

$$CF(x, y) = \left(\frac{\partial x}{\partial t}\right) \left(\frac{\partial^2 y}{\partial t^2}\right) - \left(\frac{\partial y}{\partial t}\right) \left(\frac{\partial^2 x}{\partial t^2}\right) \quad (4.3)$$

Since the curvature function depends on the first and second derivatives of the parametric curve $C(x, y)$, it is highly sensitive to boundary noise. Approximate digital computation of the derivatives of (4.3) is described in [42].

4.3.2 Radial Function

Here the boundary is approximated by an ordered sequence of angularly equispaced vectors projected between an arbitrary reference point (such as centroid) and the boundary points. This is often called the radial representation or the radial function. This way, the boundary of an object is described in polar form as $r(\phi)$, where r

represents the length of a line joining a point on the boundary with the reference point, and ϕ is the angle that this line makes with the reference axis. To make the representation invariant to translation and independent of the object contour starting point, the centroid of the object is selected as the reference point.

If, however, any of the radial vectors intersects the object more than once, the function $r(\phi)$ will be multivalued and cannot be directly used to represent the contour. To overcome this restriction, Tieng and Boles [107] proposed a modification to the radial function. The main feature of this representation is that it directly facilitates the reconstruction of the object contour. Its main drawback is that the representation is very sensitive to the occlusion because occlusion changes the location of the centroid and hence the overall representation.

4.3.3 Orientation Space

This function relates the orientation of the tangent to the curve to the arc length t along the curve. The orientation is defined as [5]

$$\phi(t) = \tan^{-1} \frac{\Delta_y}{\Delta_x} \quad (4.4)$$

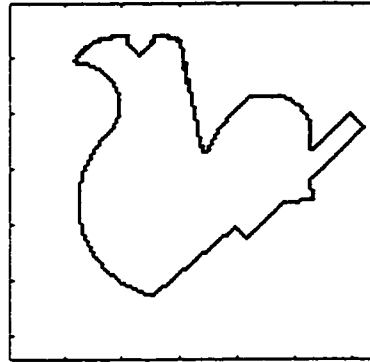
where $\Delta_y = \partial y / \partial t \approx dy/dt$ and $\Delta_x = \partial x / \partial t \approx dx/dt$. Since the arctangent function only returns an angle in the range of $(-\pi, \pi)$, any angle direction outside this range is wrapped around, thus resulting in artificial discontinuity in the edge gradient direction. The normalization step traces the function and searches for local

discontinuity greater than π or less than $-\pi$. An offset of $\pm 2\pi$ is added to the function at the following point to correct the wraparound. This will result in a continuous function along the entire contour, with the exception of the initial and final points of the contour. For a closed contour, these points will always have an artificial discontinuity of 2π [5].

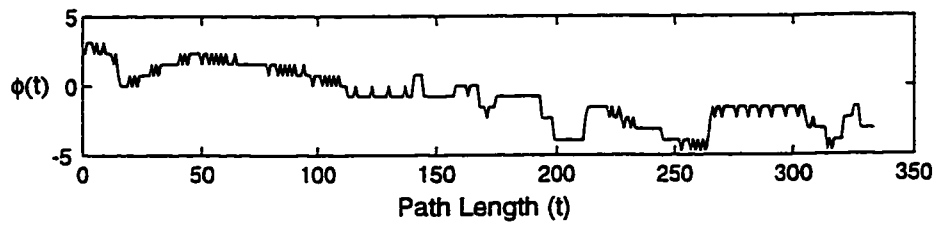
If the orientation at some point is defined by simply replacing the derivative above by the first difference, the orientation resolution, is only $\pi/4$. To improve the orientation resolution, the orientation at a point P_i is defined as

$$\phi(t) = \tan^{-1} \{(y_{i+q} - y_{i-q}) / (x_{i+q} - x_{i-q})\} \quad (4.5)$$

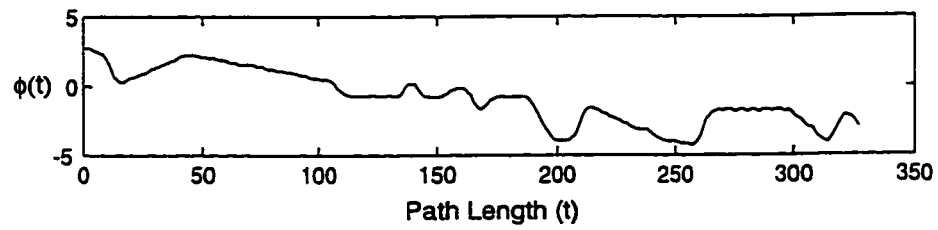
for some $q > 1$ to obtain a smoothed version of orientation. The parameter q depends on two conflicting factors, namely, the orientation resolution and the corner discrimination capability. The larger q is, the higher is the orientation resolution and the less is the corner discrimination ability. This is because two corners may be merged if they are separated with less than the smoothing length. The proper choice is to select the smallest q that can provide acceptable orientation resolution. It has been found that $q = 3$ is a reasonable choice [96]. This choice causes the orientation profile of a corner to become a ramp-like profile instead of a step with a variation interval equal to the smoothing length ($2q + 1 = 7$). Fig. 4.1(b) and 4.1(c) show the orientation profiles of the image shown in Fig. 4.1(a) for $q = 1$ and $q = 3$, respectively. Here, we continue to take $q = 3$.



(a)



(b)



(c)

Figure 4.1: Orientation-space representation (a) Input image 128×128 (b) orientation profile with $q = 1$ (c) orientation profile with $q = 3$

4.4 Detection of Corners Points

In this section, the derivation of some corner indicators based on the evolution of the wavelet transform magnitudes across scales at the corner positions is presented. Here, the results are summarized and will be used to derive certain properties that will be exploited in developing an algorithm for corner detection. Consider the wavelet function $\Psi(t) = \frac{d\theta(t)}{dt}$ where, $\psi(t)$ and $\theta(t)$ are shown in Fig. 2.3(a) and 2.3(b). For simplicity, $\theta(t)$ is considered to be the Gaussian function. Hence

$$\theta(t) = \frac{1}{\sqrt{2\pi}\sigma} \exp\left(-\frac{t^2}{2\sigma^2}\right)$$

Lee *et al.* [110] presented an analysis of the behavior of wavelet transform modulus maxima with different corner models. A summary of this analysis is presented from which several properties will be observed.

4.4.1 The Generalized Single Corner Model

Fig. 4.2(a) shows a generalized single corner, consisting of two arcs having curvatures k_1 and k_2 , enclosing an angular discontinuity of ϕ . Fig. 4.2(b) shows smoothed version of its orientation profile where $d = 2q + 1$. This smoothed corner model is defined as

$$\phi(t) = \begin{cases} k_1 t + c & -d/2 > t \\ c - dk_1/2 + [(k_1 + k_2)/2 + \delta/d](t + d/2) & -d/2 < t < d/2 \\ k_2 t + c + \delta & d/2 < t \end{cases} \quad (4.6)$$

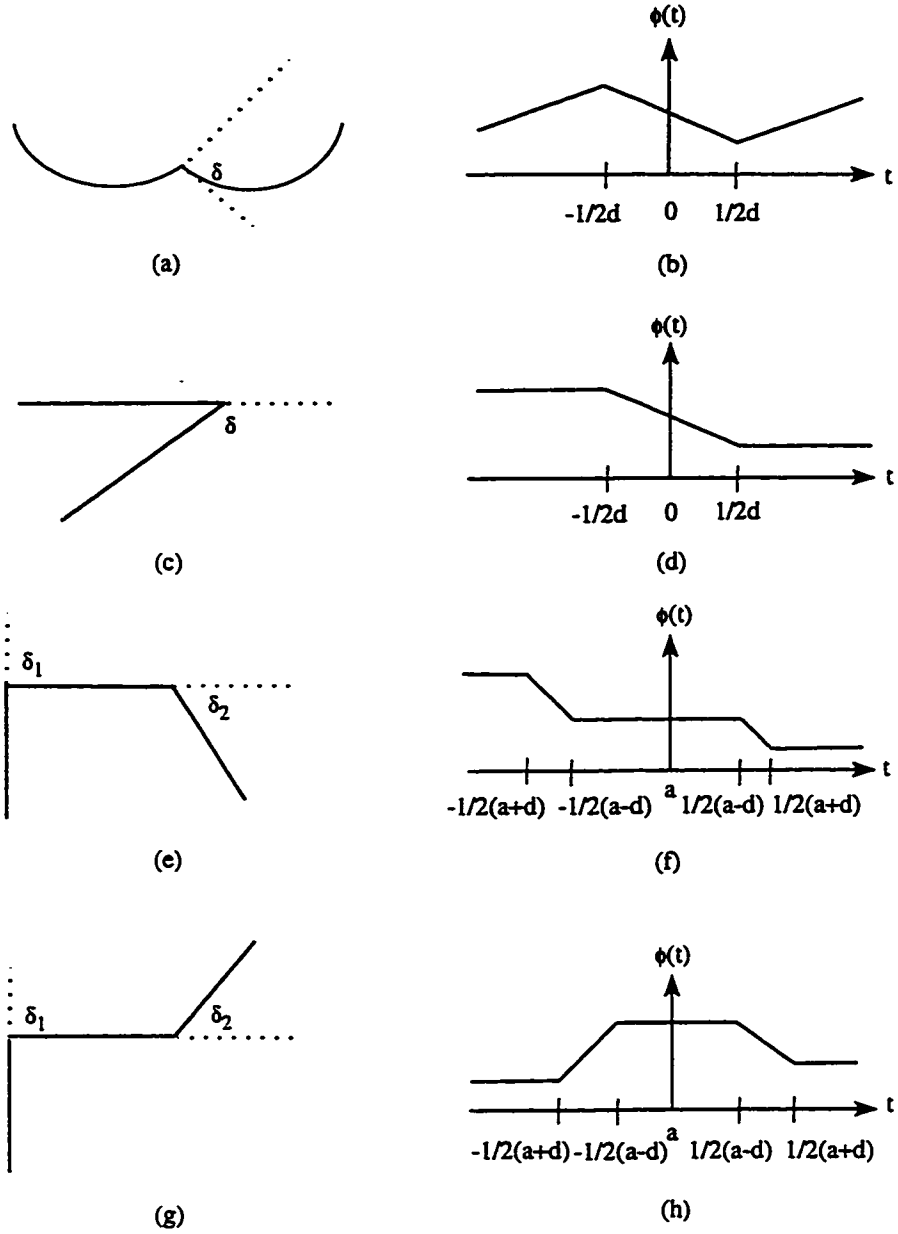


Figure 4.2: Corner models: (a) Generalized corner model, (b) Orientation profile of generalized corner model, (c) A Γ type corner, (d) Orientation profile of Γ type corner, (e) An *END* type corner, (f) Orientation profile of *END* type corner, (g) *STAIR* type corner, (h) Orientation profile of *STAIR* type corner

The wavelet transform of $\phi(t)$ at scale 2^j is the convolution of $\phi(t)$ with the wavelet function $\Psi(t)$ and is given by,

$$\begin{aligned} W_j\phi(t) = & \left(1/(2^j\sqrt{2\pi}\sigma)\right) \left\{ k_2 \int_{-\infty}^{t-d/2} \exp(-s^2/2^{2j+1}\sigma^2) ds \right. \\ & + k_1 \int_{t+d/2}^{\infty} \exp(-s^2/2^{2j+1}\sigma^2) ds \\ & \left. + [(k_1 + k_2)/2 + \delta/d] \int_{t-d/2}^{t+d/2} \exp(-s^2/2^{2j+1}\sigma^2) ds \right\} \end{aligned} \quad (4.7)$$

Differentiating (4.7) with respect to t with the limit $d \rightarrow 0$ we get,

$$\begin{aligned} \frac{dW_j\phi(t)}{dt} = & \left(1/(2^j\sqrt{2\pi}\sigma)\right) \left\{ (3/2)[k_1 + k_2] \exp(-t^2/2^{2j+1}\sigma^2) \right. \\ & \left. + [\delta/d] \exp(-t^2/2^{2j+1}\sigma^2) \right\} \end{aligned} \quad (4.8)$$

From (4.8) one can observe that the local maximum of $W_j\phi(t)$ exists at $t = 0$ and this maximum position is independent of the corner angle δ , the curvature k and the scale factor j . Hence, the local extremum will produce a consistent peak in the wavelet transform. Following [110], one can show that *Inter - Scale Difference Decay Rate* (ISDDR) is given by

$$ISDDR_j = \frac{(1 - 1/\sqrt{2}) - (d^2/96.2^2j.\sigma^2)(2 - 1/\sqrt{2})}{(\sqrt{2} - 1/2) - (d^2/48.2^2j.\sigma^2)(2\sqrt{2} - 1/2)} \quad (4.9)$$

Here, we observe that ISDDR does not change much across the scales (j). Hence a corner survives through most of the scales.

4.4.2 The Γ Type Corner Model

We now consider another corner model as shown in Fig. 4.2(c). Clearly this corner model is just a special case of the generalized single corner model (if $k_1 = k_2 = 0$). This corner model is very important since it is encountered frequently in practical applications, e.g. robot vision and industrial inspection. Fig. 4.2(d) shows the smoothed corner model in the orientation space. This smoothed corner model is defined by

$$\phi(t) = \begin{cases} c & -d/2 > t \\ c + (\delta/d)(t + d/2) & -d/2 < t < d/2 \\ c + \delta & d/2 < t \end{cases} \quad (4.10)$$

Following [110], one can obtain the indicator for this corner model, *Inter-Scale Decay Rate* (ISDR), which is defined as

$$\begin{aligned} ISDR_j &= W_{j+1/2}\phi(0) / W_j\phi(0) \\ &= \frac{24 \cdot 2^2 j \cdot \sigma^2 - d^2/2}{24\sqrt{2} \cdot 2^2 j \cdot \sigma^2 - \sqrt{2}d^2} \end{aligned} \quad (4.11)$$

Here, also we observe that ISDR does not change much with the change of the scales (j). Hence, a Γ type corner survives through most of the scales.

4.4.3 The *END* Type Corner Model

The *END* type corner model consists of two corners whose angle changes are with the same sign and separated by a width of d as shown in Fig. 4.2(e). The profiles of

this type of corner model in the orientation space are sketched in Fig. 4.2(f). The corresponding definition of Fig. 4.2(e) is given as

$$\phi(t) = \begin{cases} c & -(a+d)/2 > t \\ c + (\delta_1/d)[t + (a+d)/2] & -(a+d)/2 < t < -(a-d)/2 \\ c + \delta_1 & -(a-d)/2 < t < (a-d)/2 \\ c + \delta_1 + (\delta_2/d)[t - (a-d)/2] & (a-d)/2 < t < (a+d)/2 \\ c + \delta_1 + \delta_2 & (a+d)/2 < t \end{cases} \quad (4.12)$$

The wavelet transform of $\phi(t)$ is given as

$$\begin{aligned} W_j \phi(t) = & \left(1/2^j \sqrt{2\pi}\sigma\right) \left\{ (\delta_2/d) \int_{t-(a+d)/2}^{t-(a-d)/2} \exp(-s^2/2^{2j+1}\sigma^2) ds \right. \\ & \left. + (\delta_1/d) \int_{t+(a-d)/2}^{t+(a+d)/2} \exp(-s^2/2^{2j+1}\sigma^2) ds \right\} \end{aligned} \quad (4.13)$$

Following [110], one can obtain the indicator of this corner model, *Spatial Difference Decay Rate* (SDDR), which is defined as ($\delta_1 \neq \delta_2$)

$$SDDR_j = (1/\sqrt{2}) \frac{IT_{j+1/2} - OT_{j+1/2}}{IT_j - OT_j} \quad (4.14)$$

where

$$IT_j = \int_{-d/2}^{+d/2} \exp(-s^2/2^{2j+1}\sigma^2) ds$$

and

$$OT_j = \int_{a-d/2}^{a+d/2} \exp(-s^2/2^{2j+1}\sigma^2) ds$$

We also observe here that ISDR does not change much with the scales (j). Hence, an *END* type corner survives through most of the scales. Now if $j \gg d$ then $IT_j \approx OT_j$ and hence *END* type corner converges to a single corner.

4.4.4 The *STAIR* Type Corner Model

The *STAIR* type corner is like *END* type corner except that the changes in the corner angles are of opposite signs as shown in Fig. 4.2(g). Its corresponding orientation profile is shown in Fig. 4.2(h). Mathematically it is given as

$$\phi(t) = \begin{cases} c & -(a+d)/2 > t \\ c + (\delta_1/d) [t + (a+d)/2] & -(a+d)/2 < t < -(a-d)/2 \\ c + \delta_1 & -(a-d)/2 < t < (a-d)/2 \\ c + \delta_1 - (\delta_2/d) [t - (a-d)/2] & (a-d)/2 < t < (a+d)/2 \\ c + \delta_1 - \delta_2 & (a+d)/2 < t \end{cases} \quad (4.15)$$

Following [110] one can find that for *STAIR* type corner model,

$$SDDR_j = (1/\sqrt{2}) \frac{IT_{j+1/2} - OT_{j+1/2}}{IT_j - OT_j} \quad (4.16)$$

which is the same as the result of *END* type corner but here IT_j and OT_j are of opposite sign. Hence, when the scale increases the two extrema move away from each other.

4.4.5 Properties

The analysis presented in the previous subsections results in few properties which can be summarized as follows:

Property 1: If the local variation is the result of an isolated single corner, then the corresponding extremum survives at every scale. In case of a double corner, at least one will persist at higher scales in the wavelet transform domain.(From the analysis of *Generalized* and Γ type corner model.)

Property 2: For an *END* type corner, the two extrema have the same signs and move towards each other as the scale increases and get merged into one. As to a *STAIR* type corner, the two extrema are with opposite sign and move away from each other when the scale increases. (From the analysis of *END* and *STAIR* type corner model.)

Property 3: For an *END* type corner, the interaction between the two corners is constructive, hence the wavelet transform magnitudes at the two corner positions are larger than that of a single corner. On the contrary, for *STAIR* type corner, the interaction between the two corners is destructive. Hence, the wavelet transform magnitudes at the two corner positions are smaller than that of a single corner. (From the analysis of *END* and *STAIR* type corner model.)

Property 4: In wavelet transform domain, any important event is detected easily at higher scales, while good localization of the events is obtained at lower scales [42].

Fig. 4.3 shows an illustration of these properties when spline wavelet (discussed in Chapter 2) is used instead of the first derivative of the Gaussian. We observe that these properties are also valid for spline wavelet also.

4.4.6 Corner Detection Algorithm

In this subsection, a robust corner detection algorithm using spline wavelet is proposed. Corners and arcs are relative terms and largely depend upon the shape of the object under consideration. For example, if there are sharp corners at the boundary, small curvature changes will not be recognized as corners. On the other hand, if the shape consists only of small curvature changes then these curvature changes will be recognized as corner points. Hence, in order to provide such robustness, this algorithm starts with the normalization of wavelet transform modulus maxima. This normalization is obtained at each level regarding the global maxima of that level. This normalization also makes the algorithm adaptive when a different wavelet is used for the decomposition. This is done in Step 1 of the algorithm.

Step 1:

Orientation profile $\phi(t)$ is decomposed using wavelet transform at scales $2^1, 2^2, 2^3$

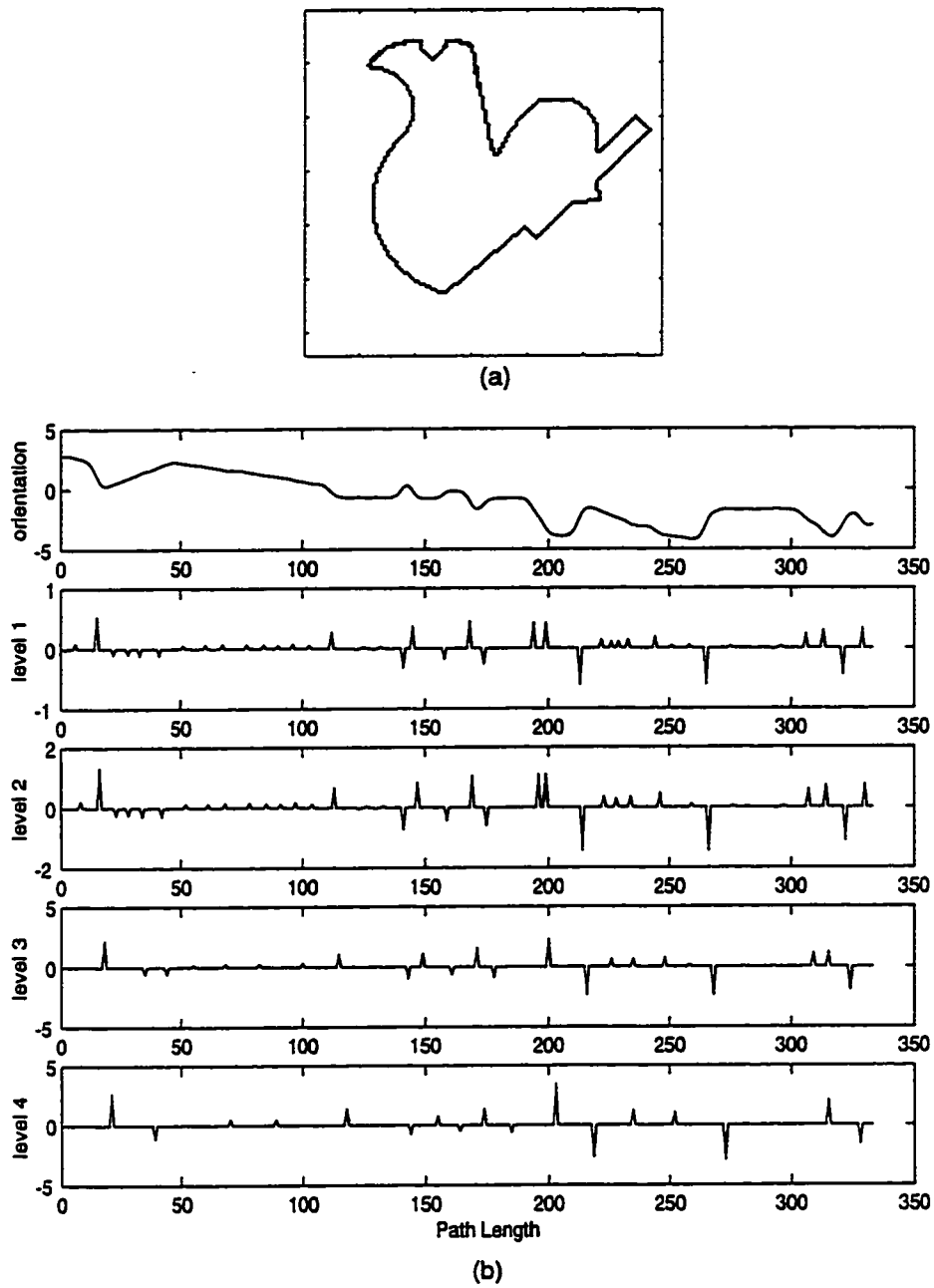


Figure 4.3: A demonstration (a) input image 128×128 (b) orientation space $\phi(t)$ (Top), wavelet transform modulus maxima at scales 2^1 , 2^2 , 2^3 and 2^4 thereafter.

and 2^4 . Wavelet transform modulus maxima (WTMM) is computed at each of these levels. These WTMMs at each level are normalized with respect to the maximum peak at that level.

Step 2:

The events (valid corners) are observed at the highest scale (2^4). The peaks higher than some threshold τ_1 are recognized as valid events. These events are successively tracked at lower scales ($2^3, 2^2, 2^1$) to find their exact locations. (Property 1 and 4)

Step 3:

Those events which are increasing at decreasing scales and are greater than some threshold τ_2 ($< \tau_1$) at scale 2^4 are also taken as valid events. This step is to take care of *STAIR* type corners. These events are also successively tracked at lower scales ($2^3, 2^2, 2^1$) to find their exact locations. (Property 3 and 4)

Step 4:

Find a large (greater than some threshold τ_3) events in the vicinity of already detected events in the previous steps from the lowest scale (i.e. 2^1). This step is to find any *END* type corner model. (Property 1 and 2)

4.4.7 Results and Comparisons

Result of corner detection using the proposed scheme is shown in Fig. 4.4, where $\tau_1 = 0.4$, $\tau_2 = 0.1$ and $\tau_3 = 0.65$. Comparison of the proposed technique with that of Asada and Brady [40] and Lee et. al [96] is done in Figs. 4.5, 4.6 and

4.7. Here we observe that the performance of the proposed technique is better, or at least the same as the one presented in the literature. A test image consists of three digital arcs is taken from [42] and comparison is presented with the works of Rattarangsi and Chin [42], Sankar and Sharma [92], Teh and Chin [66], Freeman and Davis [90], Rosenfeld and Johnson [91], Anderson and Bezdek [72] and Rosenfeld and Weazka [111] (Figs. 4.8 and 4.9). This test image, shown in Fig. 4.8(a), can be interpreted in two ways. It could be interpreted as having corners at each discontinuity, or, alternatively, it consists of having only three small digital semicircles followed by a larger one. Fig. 4.8(b) shows the result according to the first interpretation whereas Fig. 4.8(c) shows the result according to the second interpretation. Fig. 4.8(d) and 4.9 show the results of previously reported works. Here we observe that the proposed technique performs best with respect to both interpretations of the test image. Moreover, the technique reported in [40] is time consuming because it requires computing decompositions using both first and second derivatives of Gaussian function. Since these derivatives are not orthogonal, fast computing techniques using subband approach does not exists. The technique presented in [96] is computationally complex because it requires taking derivative of the ratio of wavelet transform modulus maxima and then splitting the orientation profile to detect corners. The proposed technique is computationally efficient because it requires decomposing the orientation profile only once using very fast wavelet decomposition algorithms (proposed by Mallat *et. al.* [56]). Moreover,

corner detection steps, proposed here, are very simple to implement efficiently on digital computers and does not require segmenting the orientation profile. Hence, the proposed technique is computationally efficient and simple to implement.

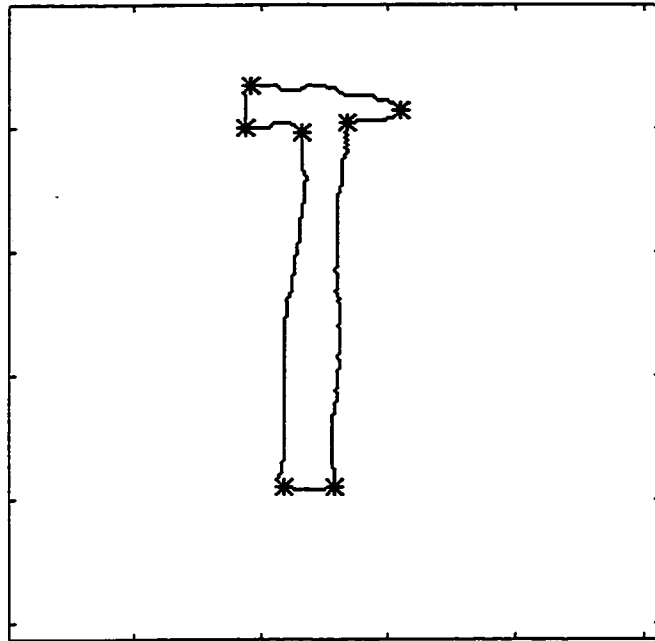
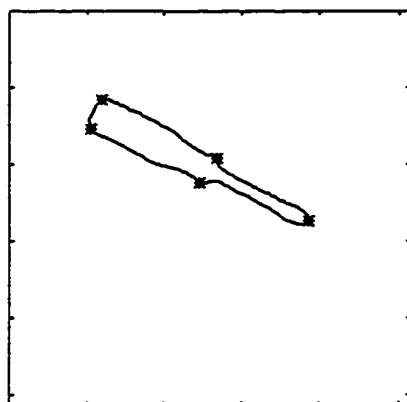


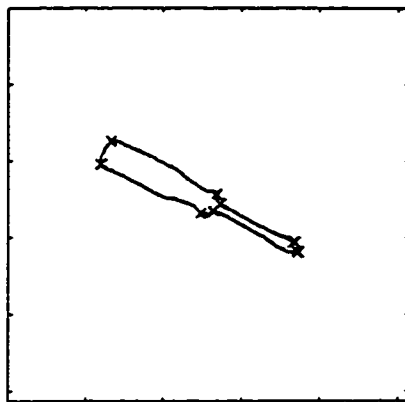
Figure 4.4: Result using wavelet-based corner detection algorithm with $\tau_1 = 0.4$, $\tau_2 = 0.1$ and $\tau_3 = 0.65$

4.5 Smooth Joins using Wavelet Transform

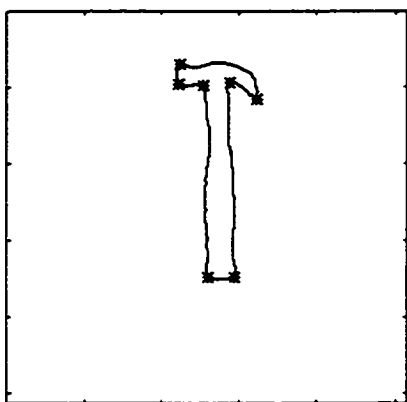
As already discussed, corners, inflections and smooth joins are important features for shape representation and analysis. Here, a wavelet-based technique is proposed to detect all these features from the orientation space of the object. Given the multiresolutional nature of wavelets along with the efficient computation algorithms,



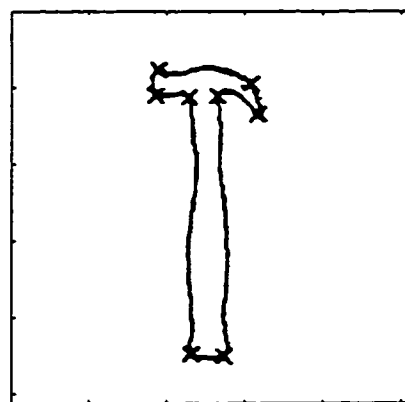
(a)



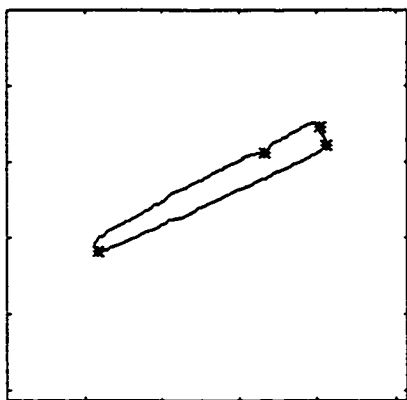
(d)



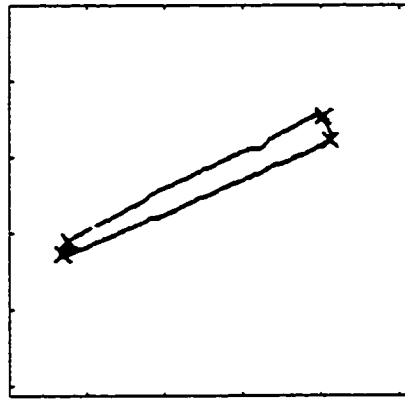
(b)



(e)

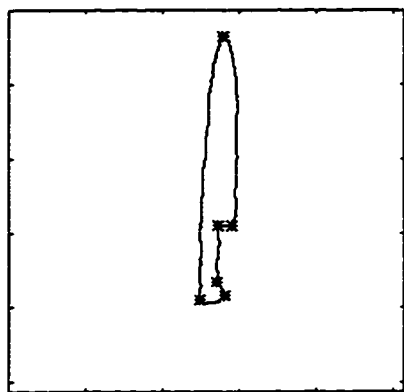


(c)

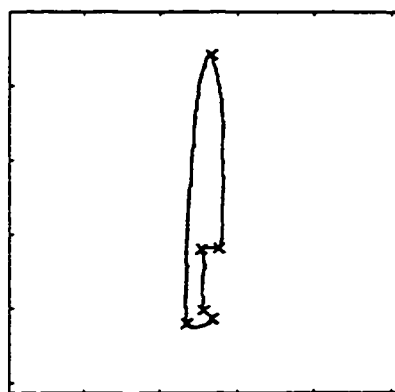


(f)

Figure 4.5: Comparisons: (a)-(c): Corners detected using proposed technique; (d)-(f): Corners detected by Asada and Brady

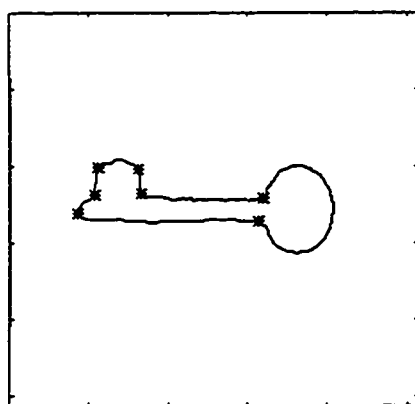


(a)

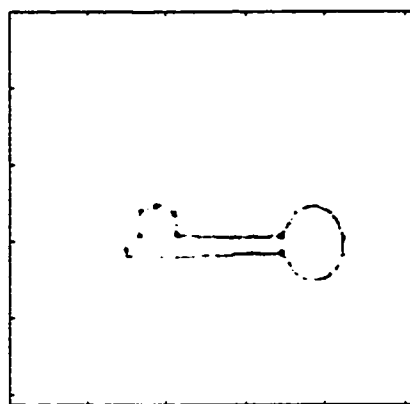


(b)

Figure 4.6: Comparisons: (a) Corners detected using proposed technique, (b) Corners detected by Asada and Brady



(a)



(b)

Figure 4.7: Comparisons: (a) Corners detected using proposed technique, (b) Corners detected by Lee, Sun and Chen

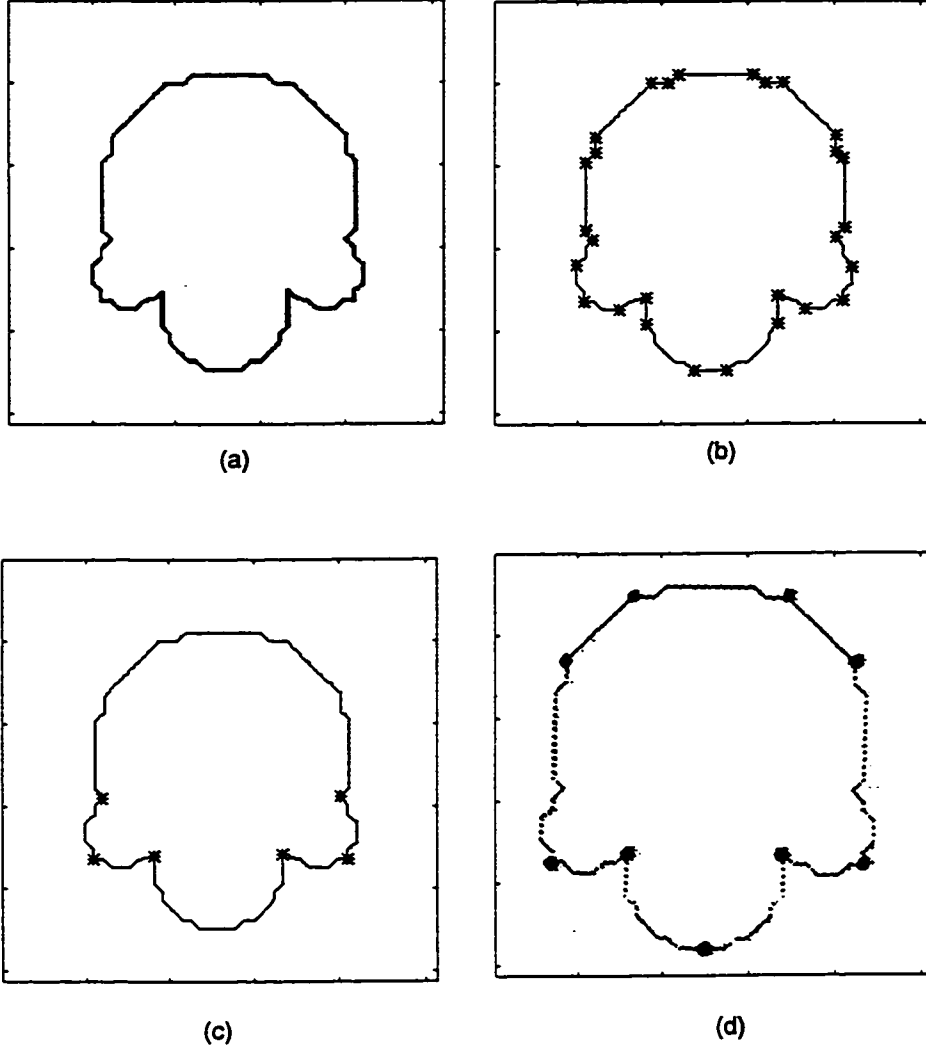
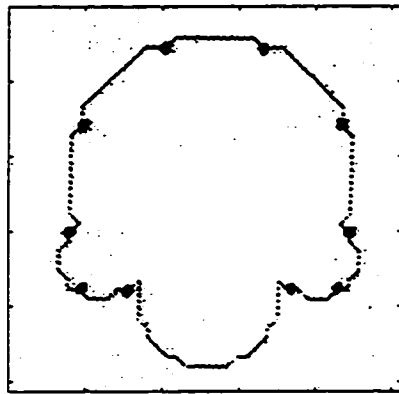
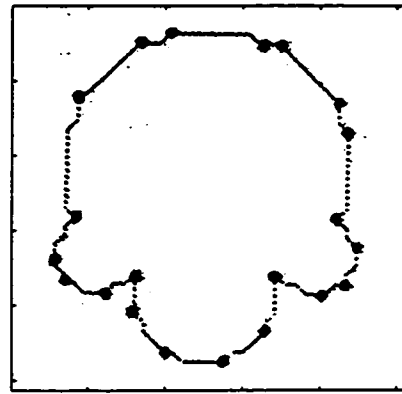


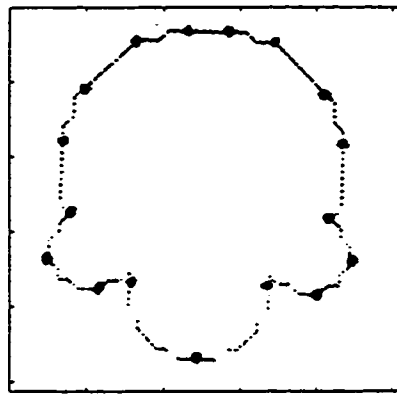
Figure 4.8: Comparisons (a) Test image (256×256) consists of one large semi-circle and three small semi-circles, (b) corners detected using proposed scheme with $\tau_1 = 0.4$, $\tau_2 = 0.1$ and $\tau_3 = 0.65$, (c) corners detected using proposed scheme with $\tau_1 = 0.9$, $\tau_2 = 0.7$ and $\tau_3 = 0.65$, (d) corners detected by Rattarangsi-Chin



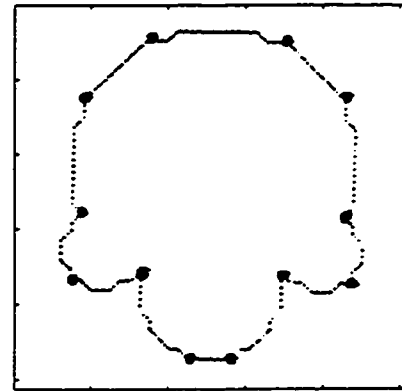
(a)



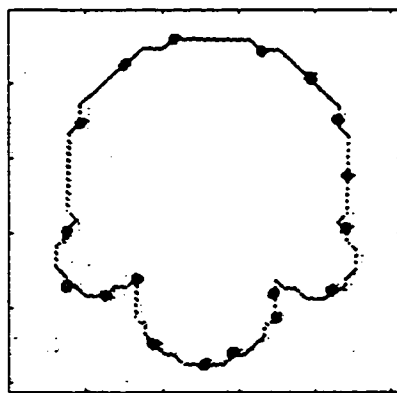
(b)



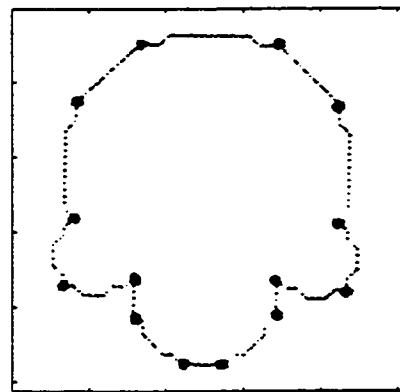
(c)



(d)



(e)



(f)

Figure 4.9: Comparisons (a) corners detected by Sankar-Sharma, (b) corners detected by Teh-Chin, (c) corners detected by Freeman-Davis, (d) corners detected by Rosenfeld-Johnson, (e) corners detected by Anderson-Bezdek, (f) corners detected by Rosenfeld-Weazka.

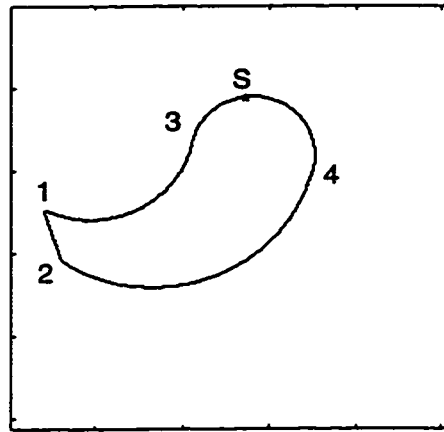
it is a natural candidate for such a task. Arcs in the orientation space, however, cannot be detected by directly using wavelets with only one vanishing moment. At the same time, wavelets with more than one vanishing moments will not be able to locate properly the sharp changes in the orientation space. Fig. 4.10 shows this difficulty.

To solve this problem, discontinuities are introduced deliberately. These discontinuities are formed by an operation similar to *Sample and Hold*. Hence ramp profiles of the arcs in the orientation space become stair type. Now the wavelet with one vanishing moment can be used to detect these artificial discontinuities and thereby providing detection of arcs along the boundary in the orientation space.

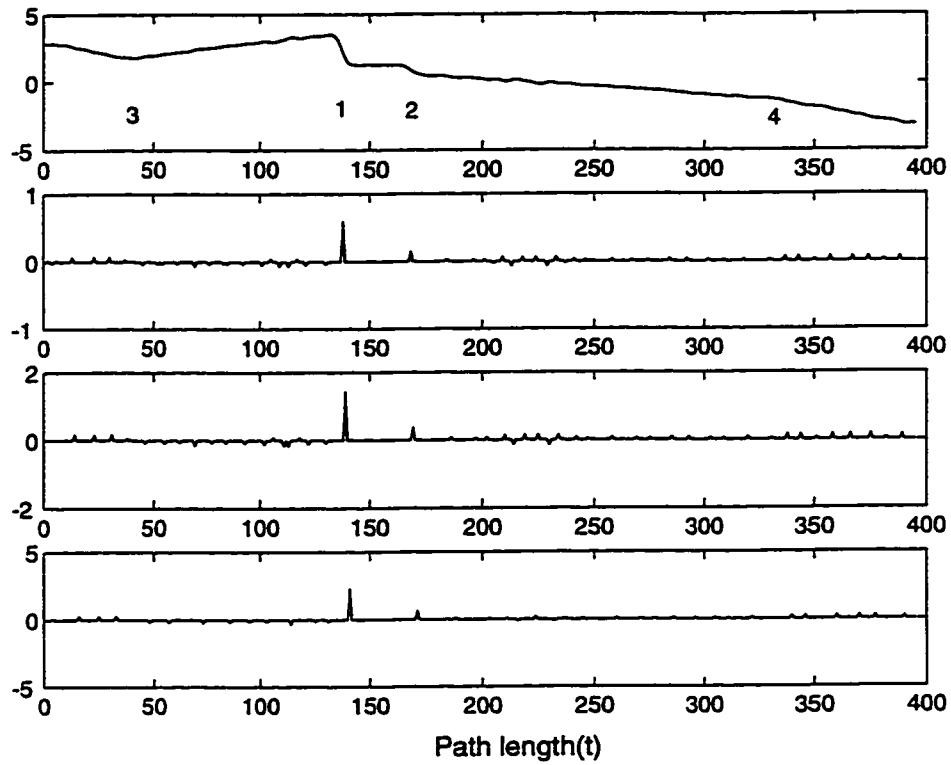
Fig. 4.11 shows the proposed detection process of smooth joins. Here Fig. 4.11(a) shows WTMM of three segments. At the top, a segment is taken from starting point to point 1 of the orientation profile shown in Fig.4.10(b). Here, we observe that the inflection point can be detected by observing the sign of WTMM which is marked as label 3. The middle figure shows the WTMM of the segment from point 1 to point 2 and the last one is for the segment from point 2 to the end. Here we can detect smooth joins by observing a discontinuity in the amplitude of WTMM which is marked as label 4. Fig. 4.11(b) shows all the corners and smooth joins detected.

The *Sample and Hold* operation (for the i th segment) is done at the interval η_i given by

$$\eta_i = \frac{l_i}{C} \quad (4.17)$$

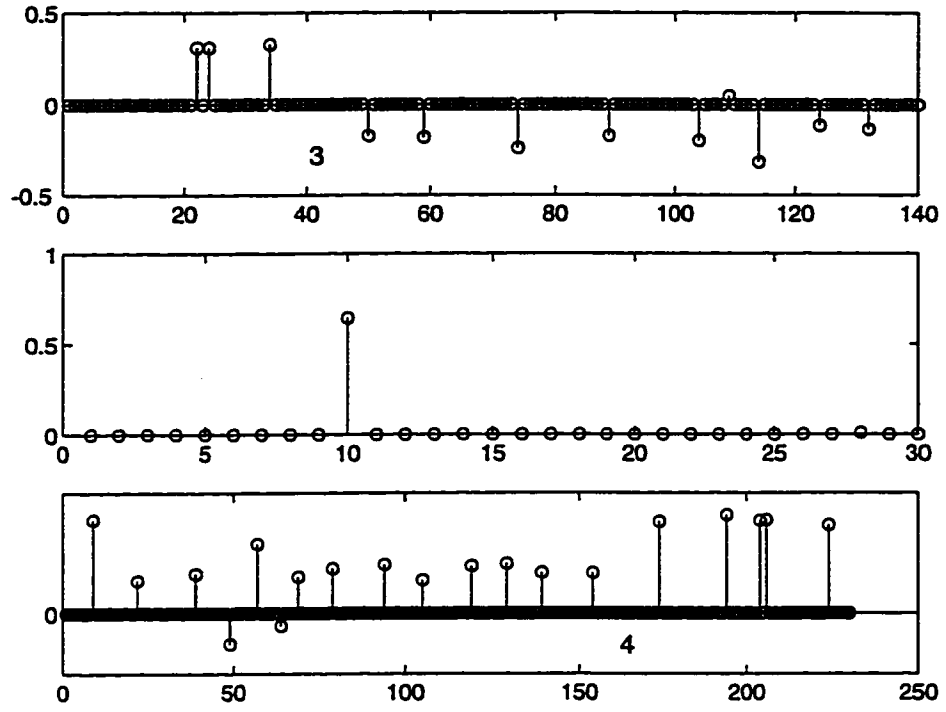


(a)

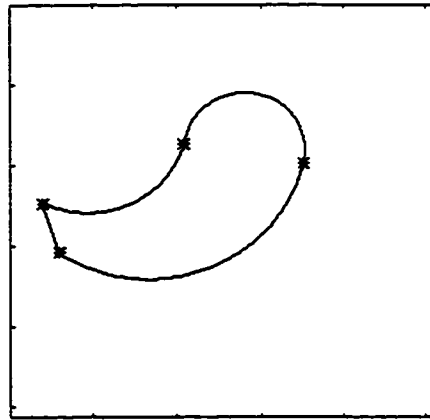


(b)

Figure 4.10: Profiles of smooth joins (a) Original image 256×256 with corners(1,2), inflection (3) and smooth join (4) 'S' indicates starting point of boundary tracking. (b) Orientation space (top) with corresponding points in the image and three levels of WTMM



(a)



(b)

Figure 4.11: Detection of smooth joins (a) WTMMs (at scale 2^3) after the introduction of discontinuities of the segments *start* - 1 (top), 1 - 2 (middle) and 2 - *end* (bottom)(b) detected corners and smooth joins.

where l_i is the length of a valid i th segment, and C is a constant. It can be seen that increasing this constant would increase the susceptibility to the noise. On the other hand, decreasing this constant would lead to more error in the detection of smooth joins. Here, $C = 5$ is found to be satisfactory.

4.5.1 Algorithm for the Detection of Smooth Joins

This algorithm is invoked only after the corner points have been detected as explained in subsection 4.4.6.

Step 1:

Segment the orientation profile, from start to end, with break points at corner points already detected. WTMM is computed at scale 2^3 for each segment (see Fig. 4.11(a)).

Step 2:

The arcs are extracted by observing those impulses which have approximately the same amplitude and are appearing consecutively. Here 3 or more consecutive impulses, of approximately the same heights, are taken as an indication of a valid arc.

Step 3:

A point of inflection is obtained at the mid point between the sign change of the two valid and consecutive arcs. This point is labeled as (3) in Fig. 4.11(a)(top).

Step 4:

A smooth join is detected by observing the sudden change in amplitude of consecutive impulses belonging to the two valid and consecutive arcs. The smooth join is

labeled as (4) on the bottom of Fig. 4.11(a).

4.5.2 Results and Comparison

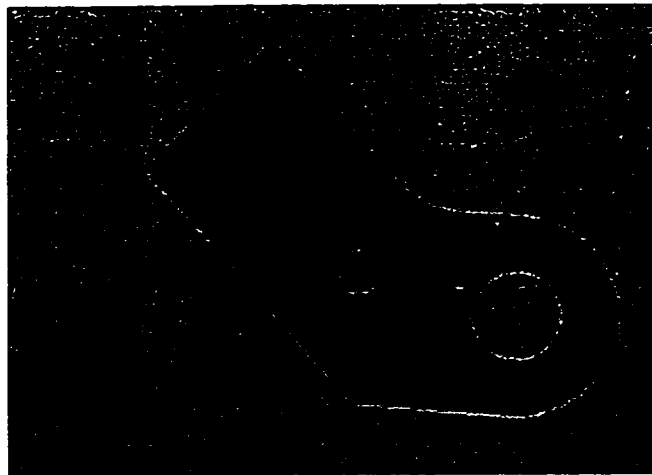
Here, for the sake of comparison, two test images are taken from a recent work of Chen, Ventura and Wu [74]. These gray level test images are shown in Fig. 4.12. The comparisons are shown in Fig. 4.13. For both the test images we see that the performance of both techniques is almost the same. It is to be noted that, the technique of [74] is computationally expensive because it requires dynamic programming. However, the proposed algorithm to detect inflections and smooth joins, requires splitting and *Sample and Hold* operation on the orientation profile only once. As can be seen the detection process is very simple to implement.

4.6 Noise Performance

We also performed corner detection tests under AWGN noise. Noise was added in the coordinates of the tracked boundary. We took a test image shown in Fig. 4.14 and performed corner detection tests with added different standard deviation (σ_N) of Gaussian noise. These results are shown in Figs. 4.14 and 4.15. We also tested smooth join detection under noise and the results are shown in Fig. 4.16.

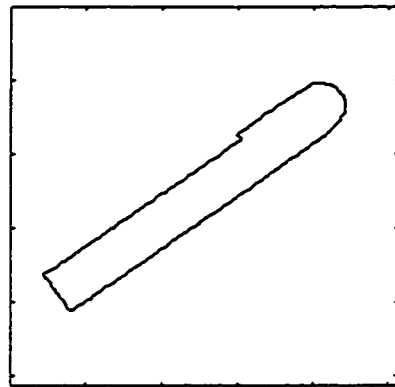


(a)

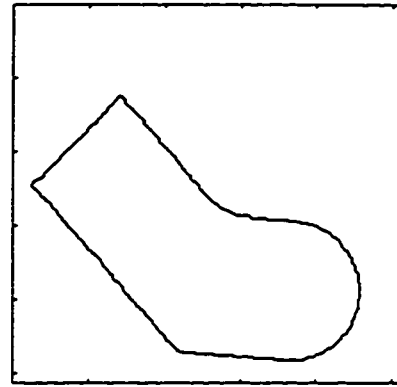


(b)

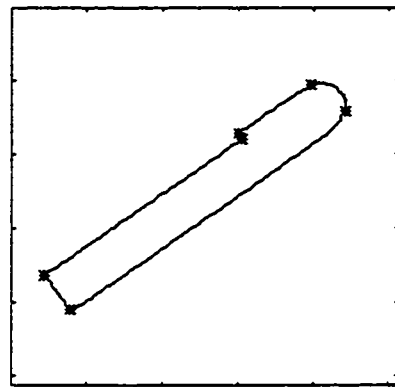
Figure 4.12: Test images (a) First gray level test image (b) Second gray level test image



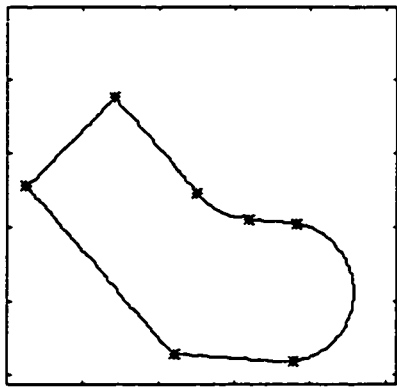
(a)



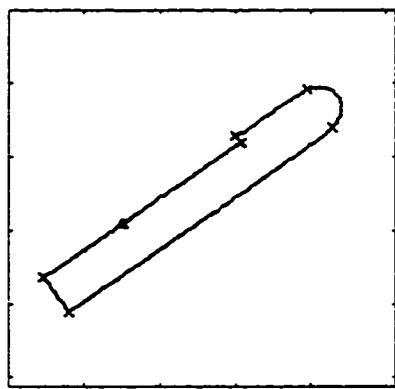
(b)



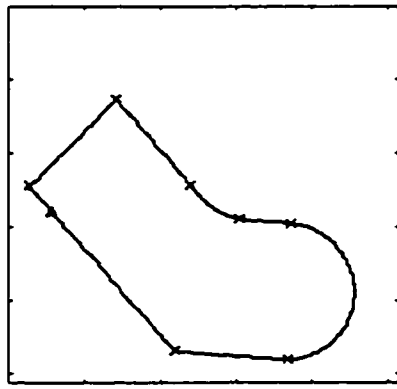
(c)



(d)

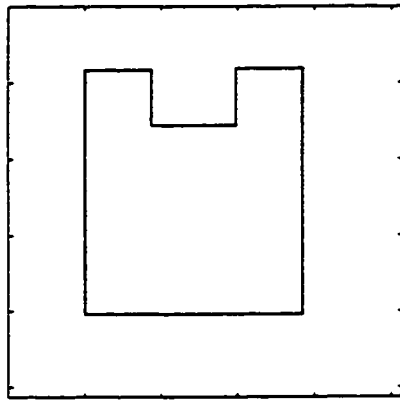


(e)

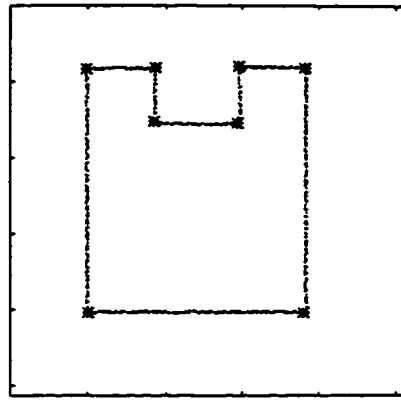


(f)

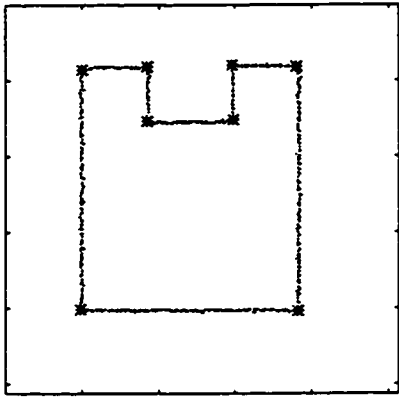
Figure 4.13: Comparisons of the proposed method with Chen *et. al.* (a),(b) Edge images after thresholding and boundary tracking of the test images (c),(d) Corners and smooth joins detected using proposed scheme (e),(f) Corners and smooth joins using the technique presented by Chen *et. al.*



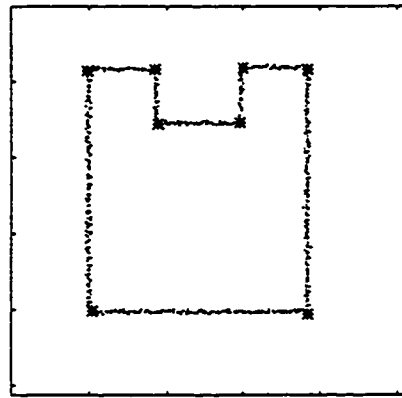
(a)



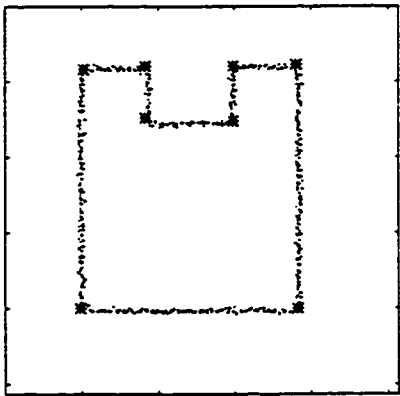
(b)



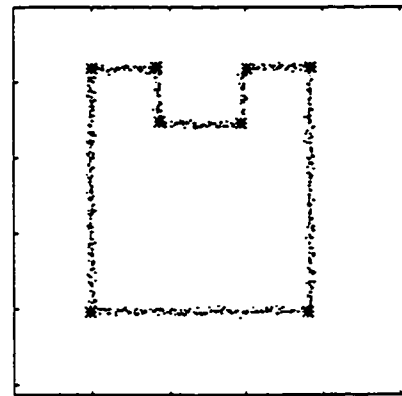
(c)



(d)

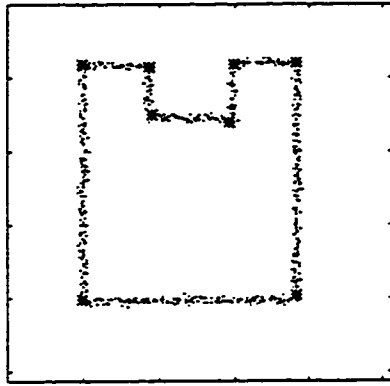


(e)

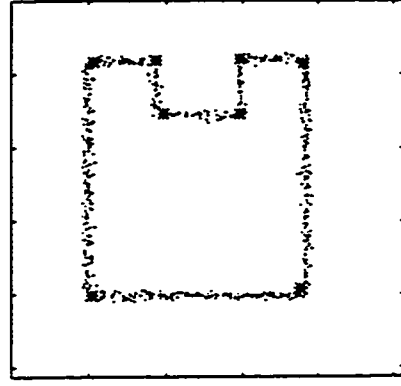


(f)

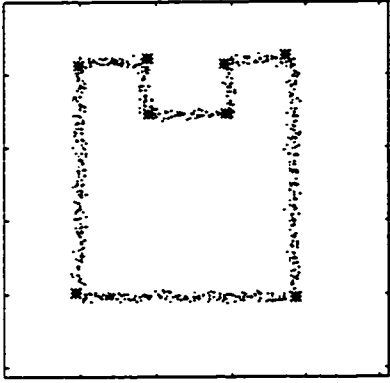
Figure 4.14: Noise performance of the proposed techniques (corner)(a) The test image, (b) $\sigma_N = 0.37$ (c) $\sigma_N = 0.72$ (d) $\sigma_N = 1.06$ (e) $\sigma_N = 1.41$ (f) $\sigma_N = 1.77$



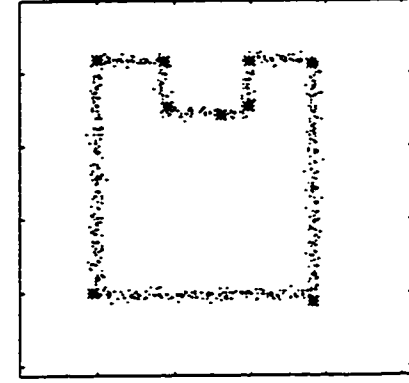
(a)



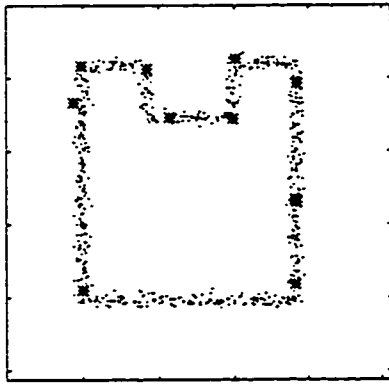
(b)



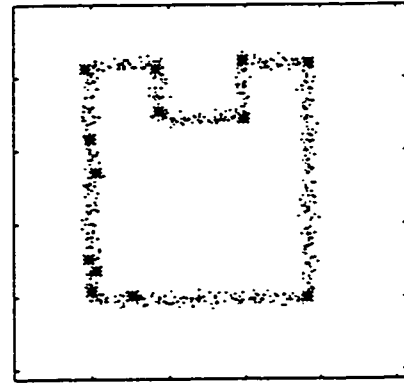
(c)



(d)



(e)



(f)

Figure 4.15: Noise performance of the proposed techniques (corner) (a) $\sigma_N = 2.09$ (b) $\sigma_N = 2.43$ (c) $\sigma_N = 2.82$ (d) $\sigma_N = 3.13$ (e) $\sigma_N = 3.59$ (f) $\sigma_N = 3.85$

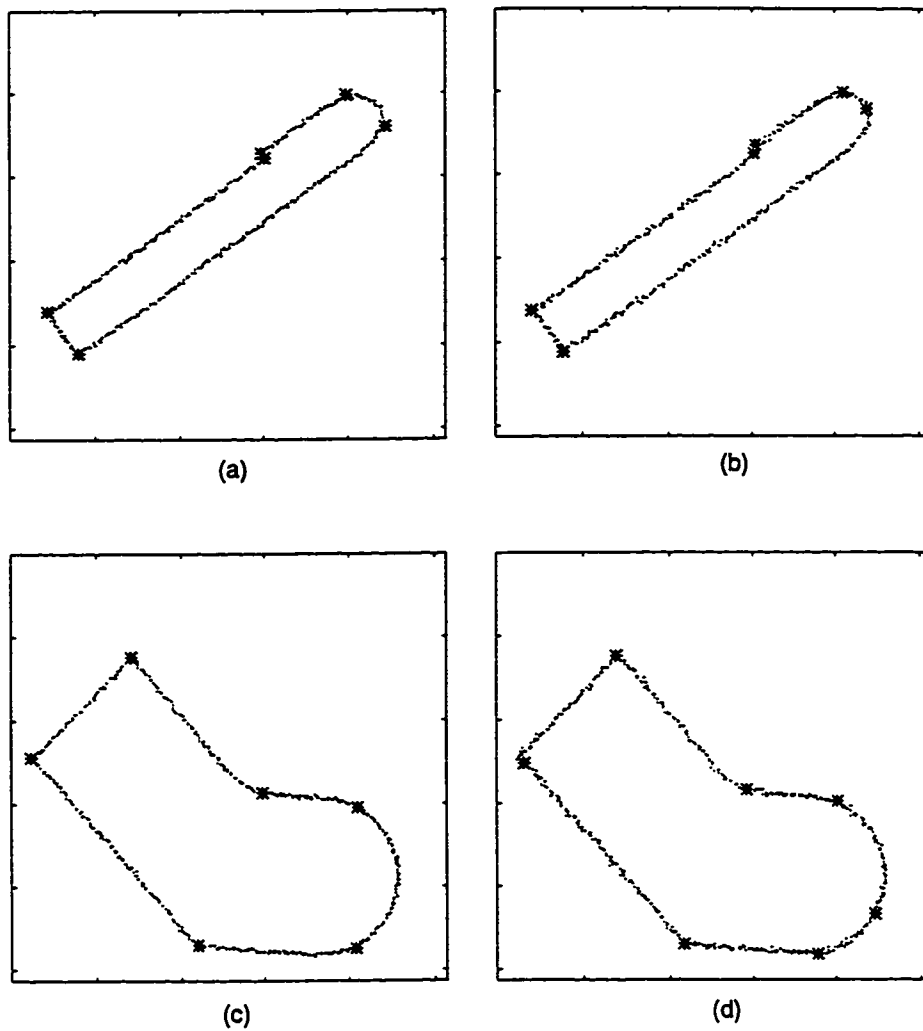


Figure 4.16: Noise performance of the proposed technique (corner and smooth joins)
(a) $\sigma_N = 0.72$ (b) $\sigma_N = 1.08$ (c) $\sigma_N = 0.69$ (d) $\sigma_N = 1.04$

4.7 Suitability of Other Wavelets

Here, we discuss the suitability of other wavelets for corner detection algorithm we proposed. Details regarding different types of wavelets are given in [102]. Morlet ([102], p. 76) and Mexican Hat wavelets ([102], p. 75) yield only continuous wavelet transform. In other words, these do not provide a complete discrete representation. Moreover, fast algorithms for their computation (using Quadrature mirror filters (QMF)) does not exist [15]. Although Meyer wavelet ([102], p. 117, 119, 137, 152) does have discrete representation, however, it does not have fast algorithms (based on QMFs) for computation. In the following we provide corner detection results only with those wavelets which have fast computation algorithms based on QMFs.

4.7.1 Haar Wavelet

Figure 4.17 shows the result of corner detection algorithm using Haar wavelet. This is a special case of Daubechies wavelet ([102], p. 115, 132, 194, 242) with one vanishing moment [15]. This is shown in Fig. 4.17(a) and the result on the test image is shown in Fig. 4.17(b). Since the evolution of wavelet transform modulus maxima (WTMM) across dyadic scale is not related with the Lipschitz regularity of the singularities in the signal, the performance is not satisfactory. Sharp corners have more than one detected corners and some relatively smooth corners are missing.

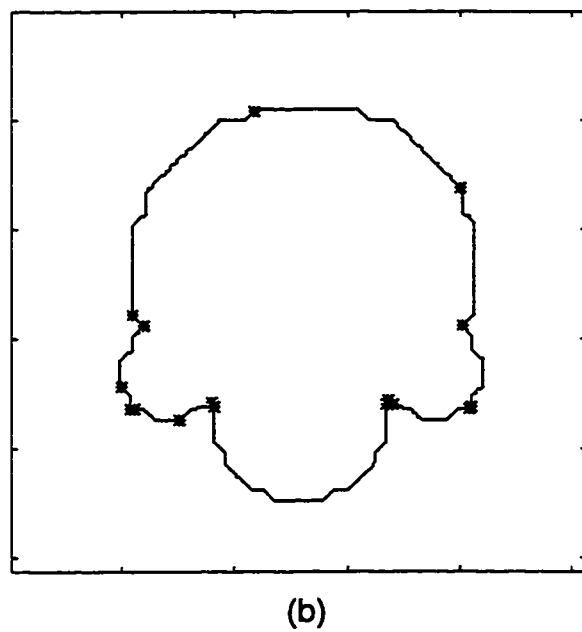
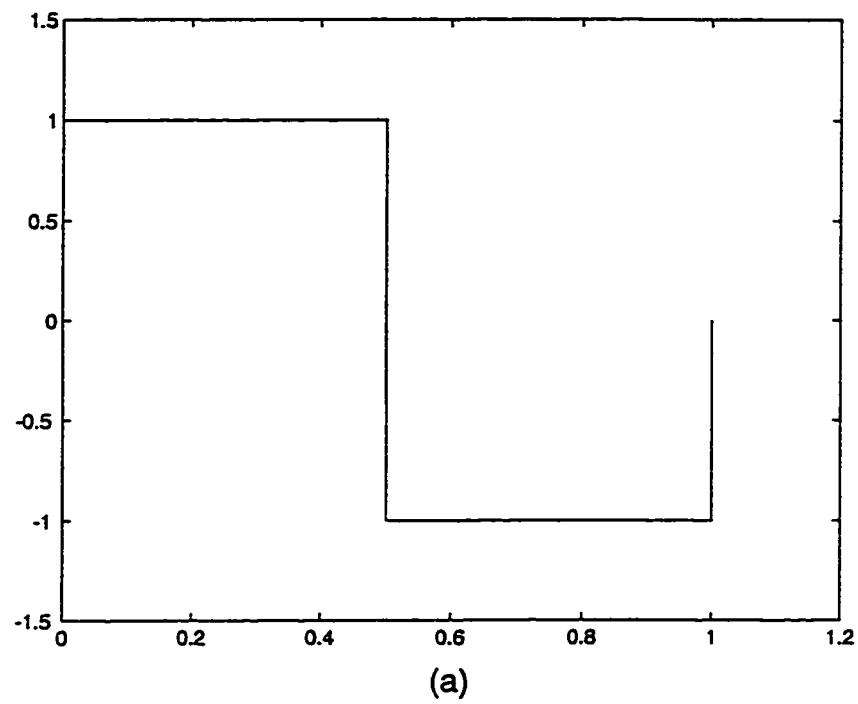


Figure 4.17: Corner detection with Haar wavelet (a) Wavelet function (b) corner detection result

4.7.2 Daubechies Wavelets

Figure 4.18 shows the result of corner detection algorithm using Daubechies wavelets. The wavelet function ([102], p. 115, 132, 194, 242) for *db2*, *db3* and *db4* is shown in Fig. 4.18(a), (b) and (c) respectively. These wavelets have vanishing moments 2, 3 and 4 respectively [15]. The results using these wavelets on the test image is shown in Fig. 4.18(d), (e) and (f). Since higher vanishing moments leads to more number of WTMMs at sharp discontinuities, the proposed algorithm detects more than one corner at these points.

4.7.3 Coiflet Wavelets

Figure 4.19 shows the result of corner detection algorithm using Coiflet wavelets. These wavelets were built by Daubechies at the request of R. Coifman ([102], p. 258-259). The wavelet function for *coif1*, *coif2* and *coif3* is shown in Fig. 4.19(a), (b) and (c) respectively. These wavelets are more symmetrical than *dbN* family. The results using these wavelets on the test image is shown in Fig. 4.19(d), (e) and (f). Since higher vanishing moments leads to more number of WTMMs at sharp discontinuities, the proposed algorithm detects more than one corner at these points.

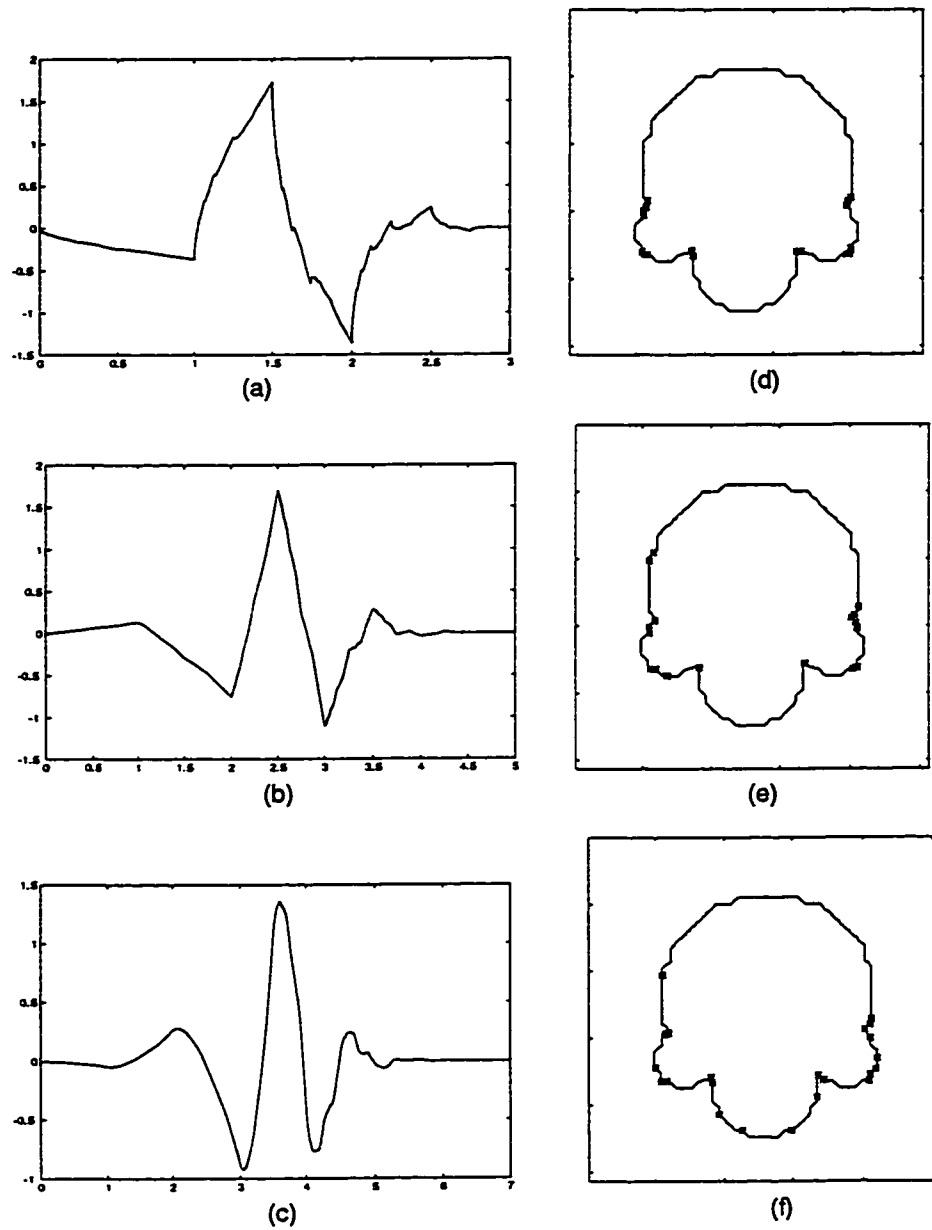


Figure 4.18: Corner detection with Daubechies wavelets (a)-(c) Wavelet functions of $db2$ to $db4$ (d)-(e) Results using $db2$ to $db4$ wavelets

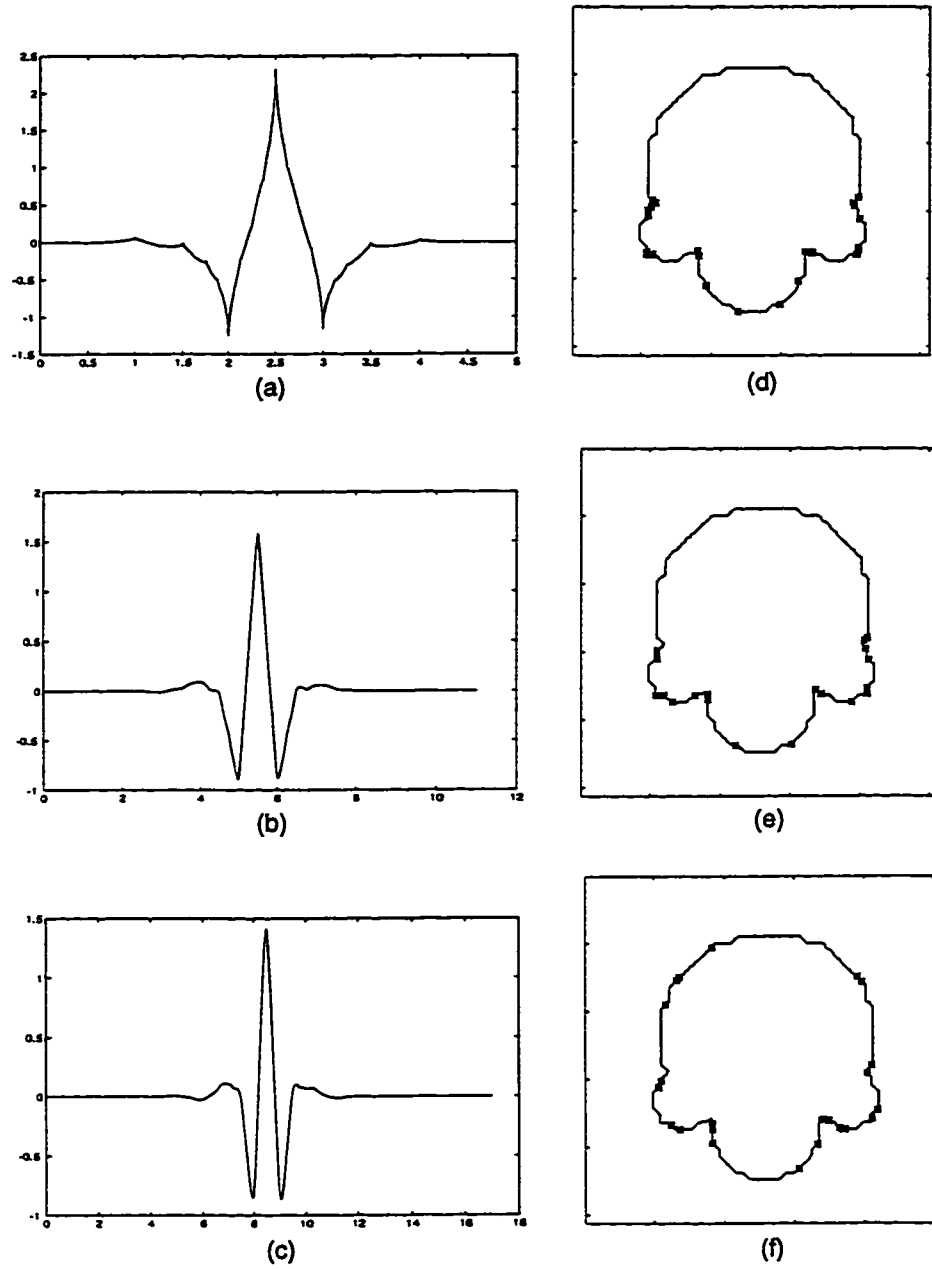


Figure 4.19: Corner detection with Coiflet wavelets (a)-(c) Wavelet functions of *coif1* to *coif3* (d)-(e) Results using *coif1* to *coif3* wavelets

4.7.4 Symlet Wavelets

Figure 4.20 shows the result of corner detection algorithm using Symlet wavelets. These wavelets were built by Daubechies and are more symmetrical than *dbN* ([102], p. 194, 254-257) family. These wavelets are implemented using "minimum phase filter" [15]. The wavelet function for *sym2*, *sym3* and *sym4* is shown in Fig. 4.20(a), (b) and (c) respectively. The results using these wavelets on the test image is shown in Fig. 4.20(d), (e) and (f). Since higher vanishing moments leads to more number of WTMMs at sharp discontinuities, the proposed algorithm detects more than one corner at these points.

4.7.5 Biorthogonal Wavelets

Figures 4.21, 4.22 and 4.23 shows the result of corner detection algorithm using Biorthogonal wavelets. These wavelets were built by Cohen *et. al.* [103]. It is well known that symmetry and exact reconstruction are incompatible, if same FIR filters are used for both decomposition and reconstruction [15]. Hence they used different FIR filters for reconstruction and decomposition. This wavelet family is labeled as *biorNr.Nd*, where *Nr* is the filter lengths for reconstruction and *Nd* is the filter length for decomposition.

The wavelet function for *bior1.3*, *bior1.5* and *bior2.2* is shown in Fig. 4.21(a), (b) and (c) respectively. The results using these wavelets on the test image is shown in

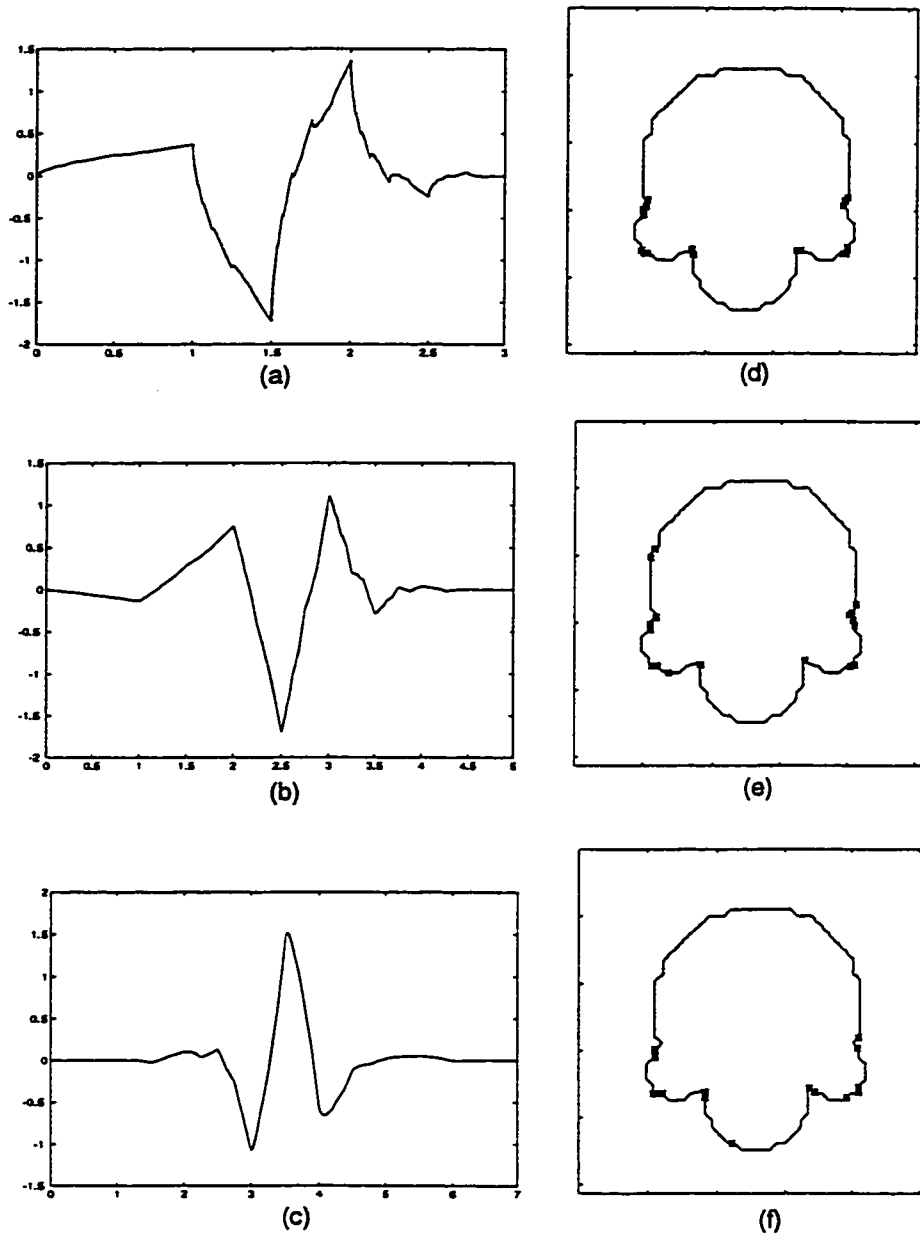


Figure 4.20: Corner detection with Symlet wavelets (a)-(c) Wavelet functions of *sym2* to *sym4* (d)-(e) Results using *sym2* to *sym4* wavelets

Fig. 4.21(d), (e) and (f). Since wavelet function *bior1.3* is quite close to the wavelet used in for the proposed algorithm (shown in Fig. 2.3(a)), the corner detection result in Fig. 4.21(d) is quite close to the result presented in Fig. 4.8(c). However, higher vanishing moments leads to more number of WTMMs at sharp discontinuities, hence, the proposed algorithm detects more than one corner at these points. For the wavelet function *bior1.5* (shown in Fig. 4.21(b)) the wavelet transform oscillates too much at the discontinuities, hence the proposed algorithm could not localize the corners accurately (see Fig. 4.21(e)). Here also more than one corner at each sharp discontinuities is detected. We also observe the same problem with other Biorthogonal wavelets (see Figures 4.22 and 4.23).

4.8 Conclusions

Here a wavelet based scheme is presented for the detection of both corners and smooth joins. The first stage detects corners and the second stage detects the smooth joins. The algorithm for the first stage is adaptive to the object geometry and the type of wavelet used in the analysis. To the best of the author's knowledge, no wavelet-based technique for detecting both corners and smooth joins has been published before. Comparisons have demonstrated that the proposed method gives competitive results with respect to the other available techniques. We also justified the use of Mallat's wavelet (defined in [56]) by using the proposed algorithm with

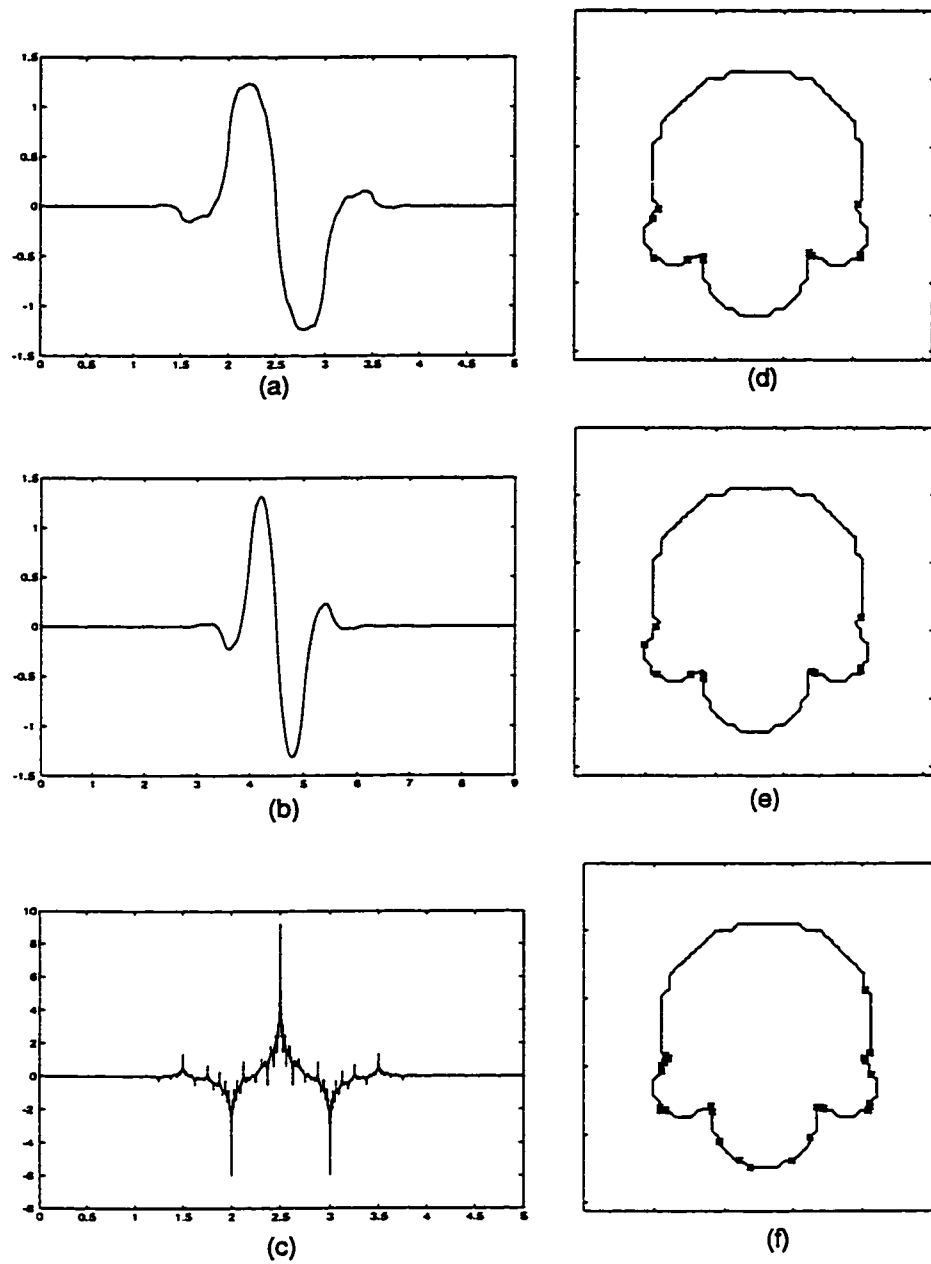


Figure 4.21: Corner detection with Biorthogonal wavelets (a)-(c) Wavelet functions of *bior1.3*, *bior1.5* and *bior2.2* (d)-(e) Results using *bior1.3*, *bior1.5* and *bior2.2* wavelets

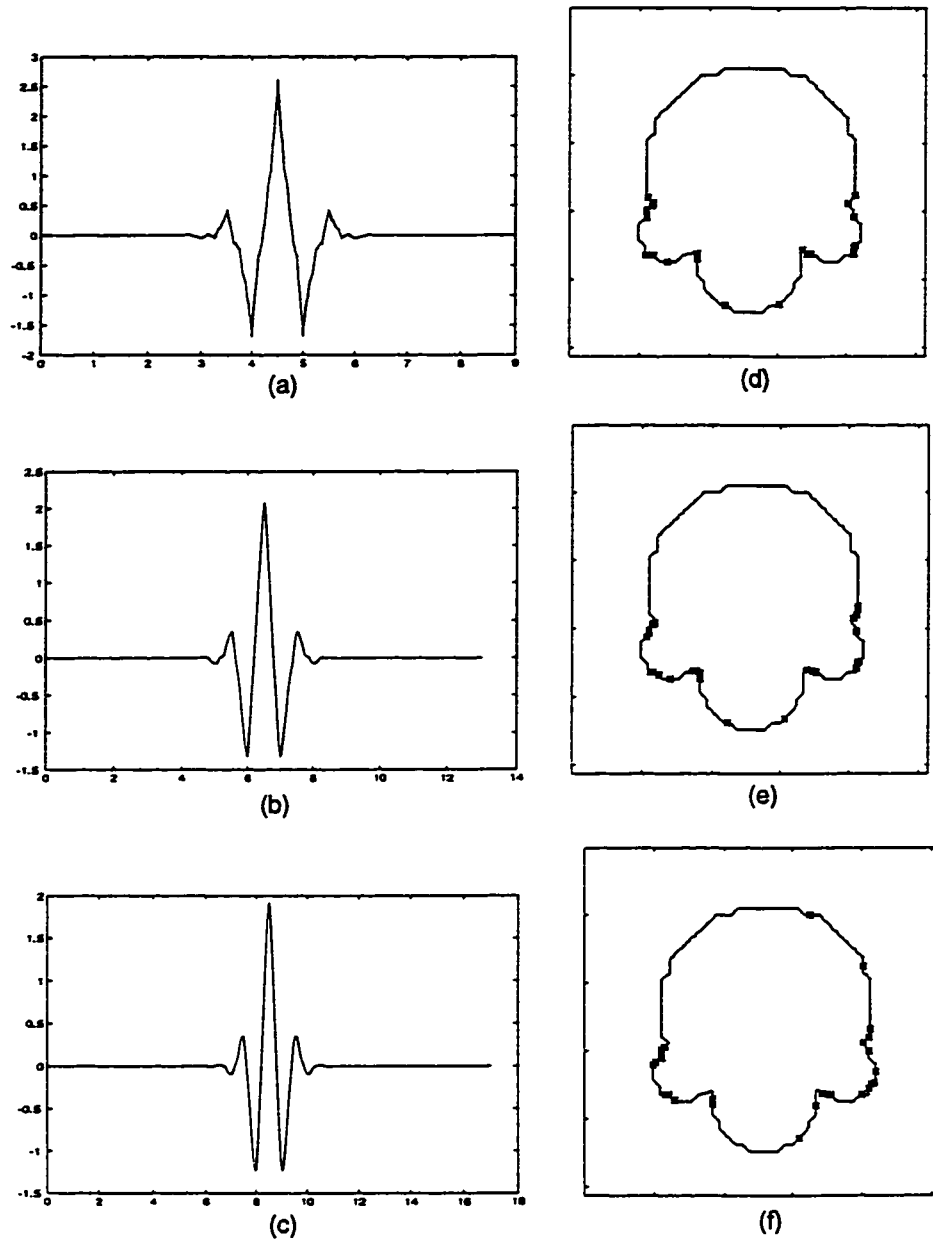


Figure 4.22: Corner detection with Biorthogonal wavelets (a)-(c) Wavelet functions of *bior2.4*, *bior2.6* and *bior2.8* (d)-(e) Results using *bior2.4*, *bior2.6* and *bior2.8* wavelets

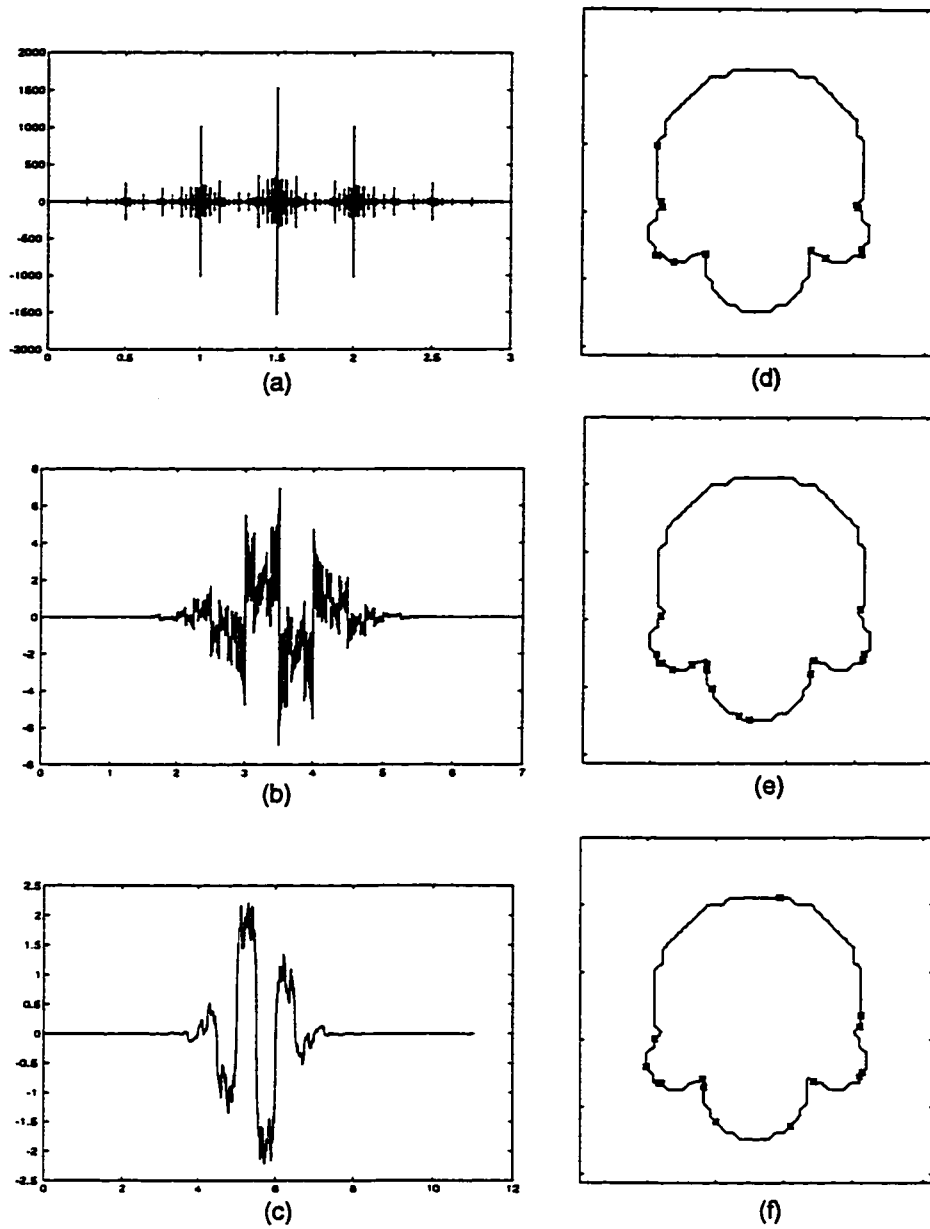


Figure 4.23: Corner detection with Biorthogonal wavelets (a)-(c) Wavelet functions of *bior3.1*, *bior3.3* and *bior3.5* (d)-(e) Results using *bior3.1*, *bior3.3* and *bior3.5* wavelets

other wavelets. The proposed technique has the advantage that it is computationally inexpensive when compared with the other techniques available in the literature. Moreover, the proposed algorithm is robust with respect to object geometry and the type of the wavelet used for the decomposition. Hence, the proposed algorithm does not require any change when the wavelet used in the analysis is changed. Following is the list of contributions:

1. *A computationally efficient scheme for the corner detection is presented. The work presented in [96] requires to compute derivative of the ratio of wavelet transform modulus maxima at two scales which may not be computationally stable. It also requires to segment the boundary to detect the corners. The proposed algorithm does not require any such step.*
2. *The corner detection algorithm is adaptive to the object geometry and the wavelet used in the decomposition.*
3. *The suitability of Mallat's wavelet [56] (against other fast wavelets) for corner detection application was proved qualitatively.*
4. *First time single wavelet transform is used for the detection of both corners and smooth joins.*
5. *Performance under AWGN noise is also presented.*

Chapter 5

CONCLUSIONS AND SUGGESTIONS

Two computationally efficient and simple to implement schemes for detecting corners are proposed. The first scheme is based on Gabor filtering. It detects only the corners and does not require preprocessing. The second scheme is based on wavelet transform. It detects corners, inflection points as well as smooth joins. In the following, we first discuss the features of each of these two corner detection schemes and then provide a comparison among them. Finally, we give suggestions for extending this work.

Firstly, a corner detection technique, based on Gabor filters, has been proposed which is suitable for both binary and gray level images, without requiring tracking the object contour. It is directly applicable to multiple objects and under occlusion.

It also detects line intersections and line endings. It is robust in the sense that it is suitable for both hot and cold objects. In addition, it is suitable for both binary and gray level images. This technique has the limitation that it misses the corner points when the angle at the corner is wide. We have also studied its performance under AWGN noise. We synthesized fifteen images each of them consisting of corner at particular angle. Each of them were subjected to varying degree of noise and the probability of detection is plotted. Here we observe that when angle is small (i.e. corner is sharp) probability of detection is very good. However, as angle at the corner increases the detection performance deteriorates. We have also defined a new performance measure regarding missing and false corners. It was observed that performance is good at low values of α and β .

Secondly, a wavelet based scheme has been presented for the detection of both corners and smooth joins. The first stage detects corners and the second stage detects the smooth joins. Both stages are computationally inexpensive as compared to other techniques. Comparisons are also given and we have demonstrated that our results are competitive with those of other available techniques in the literature. The proposed technique has additional advantage that it is computationally efficient because it uses a very fast wavelet decomposition algorithm [56] and utilizes a fast algorithm for the detection of corners, inflection points and smooth joins. The use of quadratic spline wavelet [56] is justified through qualitative analysis. Here we tested various well known wavelets in the literature and it was shown that the suggested

wavelet performs better than others. The reason for such an observation is also discussed. We subjected the test images with varying degree of AWGN noise and demonstrated that the proposed technique performs better under noise.

In what follows, we provide a comparison between the two proposed corner detection techniques. For the image shown in Fig. 4.8(a), the results of the proposed corner detection schemes using Gabor filters and wavelet transform are shown in Figs. 5.1(a) and (b), respectively. For this image we observe that wavelet based technique performs better than Gabor filter based scheme. This is because the majority of the angles in this test image are larger than 90 degrees. Hence, Gabor filter-based technique does not perform well. For the image shown in Fig. 3.22(a), the result of corner detection schemes using Gabor filters and wavelet transform is shown in Figs. 5.2(a) and (b), respectively. Here, the wavelet based technique misses the corners which do not touch the boundary. This is not the case with Gabor filter-based technique and thus for this image it outperforms the wavelet-based technique. It is important, however, to note that the performance of the wavelet-based technique in this example is not due to the technique itself. Rather, it is due to the boundary tracking algorithm in the preprocessing stage which is not able to track the edges inside the outer boundary. In general, wavelet based scheme will perform better because it requires preprocessing. However, given the advantages of Gabor filter-based scheme, it is an attractive choice, particularly, when preprocessing is to be avoided and there are multiple objects and occluded objects in the image.

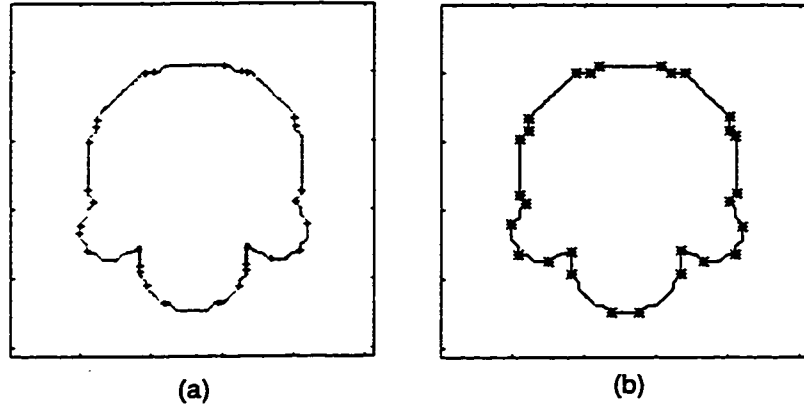


Figure 5.1: (a) Result obtained by Gabor filter based scheme (b) Result obtained by wavelet based scheme

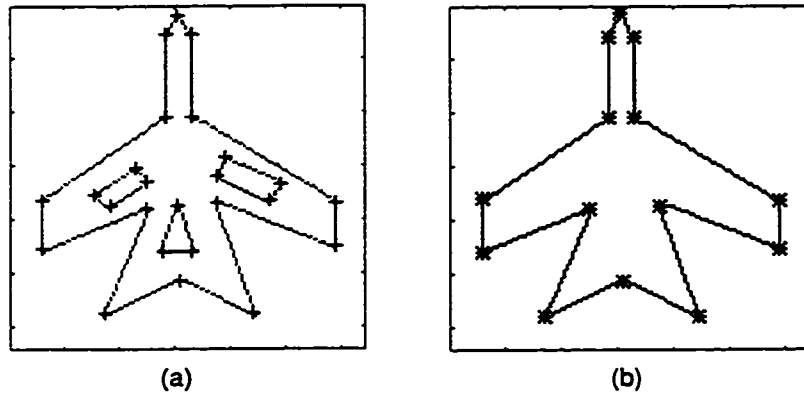


Figure 5.2: (a) Result obtained by Gabor filter based scheme (b) Result obtained by wavelet based scheme

As far as scope for future work is concerned, there are several directions along which Gabor filter-based scheme can be extended. Some of them are discussed as follows:

- In order to better understand this scheme, the iterative nonlinear filtering process is to be mathematically analyzed.
- There is also a possibility to find more efficient ways to extract corner point after filtering. In this regard, variable threshold (based on some criterion) can be tried.
- There is also a possibility to explore, analytically, the selection parameters for different applications and different types of images.

In case of wavelet-based corner detection scheme there could be following ways to extend the work:

- The relation between the number of wavelet decompositions of wavelet transform and the size and types of the corners in the image can be analyzed mathematically.
- There is a possibility to use variable threshold (based on some criterion) which will make the algorithm adaptive to the type and class of objects in the image.
- There is a possibility to develop a similar corner detection algorithm by using other than the orientation profile as a 1-D representation of the boundary

information. This work will help to explore the relation between these 1-D representation of the boundary information.

APPENDIX: MATLAB Code For Algorithms Developed

This appendix provides the actual MATLAB code developed for the implementation of the algorithms discussed in this thesis.

Function *filgn*

This function implements iterative filtering scheme. It input arguments are input image matrix *in*, filtering function in frequency domain *H* and mean square error criterion *err* for termination of the iterative filtering. This function outputs filtered image and the number of iterations.

```
function [out,i]=filgn(in,H,err)
% Repeatitive Gabor filtering
% By: Azhar Quddus
i=0;
[out,ft]=filg(in,H);
msqr=10000;
while msqr >= err
    outb=out;
    [out,ft]=filg(out,H);
    msqr=mean(mean((abs(outb-out)).^2));
i=i+1
end
return
```

Function *clustr*

This function implements the algorithm to find corner points from filtered image. It input argument is filtered image matrix *outf*. This function outputs the detected corners.

```

function p=clustr(outf)
%This function finds the corners
%after filtering

out=outf;
[ro,co]=size(out);
o=zeros(ro,co);

%Treat for boundary points
out(1:3,:)=zeros(3,co);
out(ro-2:ro,:)=zeros(3,co);
out(:,1:3)=zeros(ro,3);
out(:,co-2:co)=zeros(ro,3);

%Finding Max. Point
mx=max(max(out));

mmx=10;
i=0;

while mmx > 0.4*mx,
i=i+1;
[coor,mmx]=maxval(out);
if mmx < 0.55*mx
break;
end

r=coor(1);
c=coor(2);
p(i,1:2)=[r c];

out(r-4:r+4,c-4:c+4)=zeros(9,9);

end
return

```

Function mycor

This function implements the detection of wavelet-based corner detection algorithm. Its input argument is the wavelet transform of the orientation profile w . This function outputs the detected corners.

```

function c=mycor(w)

[r,c]=size(w);
level=r-1;

% Compute WTM
for i=1:level
    wmm(i,:)=mymodm(w(i,:));
end
awm=abs(wmm);

% Compute Score at each level
for i=1:level
    cmx=max(awm(i,:));
    score(i,:)=awm(i,:)/cmx;
end

%Start from last level
pos=find(awm(level,:));
lp=length(pos);
count=0;

for p=1:lp
    cp=pos(p);
    cwm=wmm(level,cp);
    cscr=score(level,cp);
    for l=level-1:-1:1
        cw=wmm(l,:);
        while sign(cw(cp))~=sign(cwm) & cp>1,
            cp=cp-1;
        end
        if (score(l,cp)>0.1 & score(l,cp)-cscr>-0.1) | score(l,cp)>=0.4
            flag=1;
            cwm=wmm(l,cp);
            cscr=score(l,cp);
        else
            flag=0;
            break
        end
    end
    if flag==1 & cscr>0.1

```

```

        count=count+1;
        c(count)=cp;
    end
end

% clearing WTMM from first phase corners
len=length(c);
x1=score(1,:);
x1(c)=zeros(1,len);
%Extracting end corners
lastf=find(x1>0.65);
c=sort([c lastf]);

return

```

Function *myinflec*

This function implements the detection of wavelet-based smooth join detection algorithm. It input arguments are the orientation profile x and the detected corners in the previous algorithm cn . This function outputs the detected corners and smooth joins.

```

function c=myinflec(x,cn)
%This function finds point of inflection
% given input vector is 'x'
% cn-> corner vector

len=length(cn);
ccount=0;
lenx=length(x);
ccount=0;
i=1;
for i=1:len+1
    if i==1
        st=1;
        en=cn(1);
    elseif i==len+1
        st=cn(len);
        en=lenx;
    else
        st=cn(i-1);
    end
    cccount=ccount+1;
    c(ccount)=x(st:en);
end

```



```

        en=cn(i);
    end

    curx=x(st+1:en-1);

    curl=length(curx);
    cj=floor(curl/5);
    if cj~=0
        sp=myshld(curx,cj);
        xw=myndwt(sp,3);
        xwm=mymodm(xw(3,:));
        [pc,nc]=mycrv(xwm);
        %subplot(3,1,i),stem(xwm)

        cc=sort([pc;nc])
        [row,col]=size(cc);
        if ~isempty(cc)
            for k=1:row-1
                ccount=ccount+1;
                c(ccount)=st+cc(k,2)+round((cc(k+1,1)-cc(k,2))/2);
            end
        end
        j=i+1;
    end
end

return

```

Bibliography

- [1] C. A. Mead, *Analog VLSI and neural systems*, Addison Wesley, N.Y., 1990.
- [2] F. Attneave, "Some informational aspects of visual perception", *Psychol. Rev.*, vol. 61, no. 3, pp. 183–193, 1954.
- [3] A. Quddus, *A novel scheme for detection of 2-D motion through OTA-based analog neural networks*, MSc. Engg. Thesis, Electronics Engineering Department, Aligarh Muslim University (A.M.U.), Aligarh, India., 1991.
- [4] M. W. Koch and R. L. Kashyap, "Using polygons to recognize and locate partially occluded objects", *IEEE Trans. Pattern Analysis and Machine Intelligence*, vol. PAMI-9, no. 4, pp. 483–494, July 1987.
- [5] H. C. Liu and M. D. Srinath, "Partial shape classification using contour matching in distance transformation", *IEEE Trans. Pattern Analysis and Machine Intelligence*, vol. PAMI-12, no. 11, pp. 1072–1079, Nov. 1990.

- [6] A. Rosenfeld and M. Thurston, "Edge and curve detection for visual scene analysis", *IEEE Trans. Comput.*, vol. C-20, 1971.
- [7] E. Hall, J. Rouge, and R. Wong, "Hierarchical search for image matching", *Proc. Conf. Decision Contr.*, vol. 70, pp. 791–796, 1976.
- [8] D. Marr and T. Poggio, "A theory of human stereo vision", *Royal Soc. London*, vol. B 204, pp. 301–328, 1976.
- [9] A. Rosenfeld and G. J. Vanderburg, "Coarse-fine template matching", *IEEE Trans. Syst., Man, Cybern.*, vol. 7, pp. 104–107, 1977.
- [10] J. Koenderink, *The structure of images*, Springer Verlag, New York, 1984.
- [11] S. Mallat, "Wavelets for a vision", *Proc. IEEE*, vol. 84, no. 4, pp. 604–614, April 1996.
- [12] P. Schroder, "Wavelets in computer graphics", *Proc. IEEE*, vol. 84, no. 4, pp. 615–625, April 1996.
- [13] K. Ramachandran, M. Vetterli, and C. Herley, "Wavelets, subband coding, and best bases", *Proc. IEEE*, vol. 84, no. 4, pp. 541–560, April 1996.
- [14] A. Cohen and J. Kovacevic, "Wavelets: The mathematical background", *Proc. IEEE*, vol. 84, no. 4, pp. 514–522, April 1996.

- [15] M. Misiti, Y. Misiti, G. Oppenheim, and J.-M. Poggi, *Wavelet toolbox User's Guide*, The MathWorks, Inc., 24, Prime Park Way, Natick, Mass. 01760-1500, 1996.
- [16] D. Gabor, "Theory of communications", *J. Inst. Elect. Eng.*, vol. 93, pp. 429–457, 1946.
- [17] J.G. Daughman, "Uncertainty relation for resolution in space, spatial frequency, and orientation optimized by two-dimensional visual cortical filters", *J. Opt. Soc. Amer.*, vol. 2, pp. 1160–1169, 1985.
- [18] M. Clark and A.C. Bovik, "Multichannel texture analysis using localized spatial filters", *IEEE Trans. Pattern Analysis and Machine Intelligence*, vol. 12, no. 1, pp. 55–73, Jan 1990.
- [19] M. Clark and A.C. Bovik, "Texture discrimination using a model of visual cortex", *Proc. IEEE Int. Conf. Syst., Man, Cyber.*, 1986.
- [20] R.M. Endlich and D.E. Wolf, "Automatic cloud tracking applied to goes and meteosat observations", *J. Appl. Metrology*, vol. 20, no. 3, pp. 309–319, 1981.
- [21] B.L. Yen and T.S. Huang, *Determining 3-D motion and structure of a rigid body using straight line correspondences, in 'Image sequence processing and dynamic scene analysis'*, Huang, T.S. (Ed.), Springer-Verlag, Berlin, 1983.

- [22] B.L. Yen and T.S. Huang, "Determining 3-d motion/structure of rigid body over 2 frames using correspondences of straight lines on parallel planes", *Proc. of 7th Int. Conf. on Pattern Recognition, Montreal, Canada.*, pp. 781–783, 1984.
- [23] S. Ishikawa, M. Yamada, and S.A Ozawa, "A method of estimating the target position for an image tracking system of moving targets", *Proc. of 7th Int. Conf. on Pattern Recognition, Montreal, Canada.*, pp. 9–12, 1984.
- [24] J.P. Gambitto, "Correspondence analysis for target tracking in infrared images", *Proc. of 7th Int. Conf. on Pattern Recognition, Montreal, Canada.*, pp. 526–529, 1984.
- [25] R. Kories and G. Zimmermann, "Motion detection in image sequences: an evaluation of feature detectors", *Proc. of 7th Int. Conf. on Pattern Recognition, Montreal, Canada.*, pp. 778–780, 1984.
- [26] G. Stockman, S. Kopstien, and S. Benett, "Matching images to models for registration and object detection via clustering", *IEEE Trans. Pattern Analysis and Machine Intelligence*, vol. PAMI-4, pp. 229–241, May 1982.
- [27] R. C. Bolles and R. A. Cain, "Recognizing and locating partially visible objects: The focus feature method", *Int. J. Robotics Res.*, vol. 1, no. 3, pp. 57–81, 1982.

- [28] N. Ayache, "A model based vision system to identify and locate partially visible industrial parts", *Proc. Computer Vision and Pattern Recognition*, pp. 492–494, June 1983.
- [29] B. Neuman, "Interpretation of imperfect object contours for identification and tracking", *Proc. Fourth Int. Joint Conf. Pattern Recognition*, pp. 691–693, Jan 1980.
- [30] W. A. Perkins, "A model-based vision system for industrial parts", *IEEE Trans. Comput.*, vol. C-27, Feb 1978.
- [31] P. Rummel and W. Beutel, "A model-based vision system for industrial parts", *Proc. Sixth Int. Conf. Pattern Recognition*, pp. 670–673, Oct 1982.
- [32] P. Burt and E. Adeleson, "The laplacian pyramid as a compact image code", *IEEE Trans. Comm.*, vol. COM-31, pp. 532–549, April 1983.
- [33] D. Marr, *Vision*, Freeman, San Fransisco, 1982.
- [34] S. G. Mallat, "A theory for multiresolution signal decomposition: The wavelet representation", *IEEE Trans. Pattern Analysis and Machine Intelligence*, vol. PAMI-11, no. 7, pp. 674–693, july 1989.
- [35] M. Porat and Y.Y. Zeevi, "The generalized gabor scheme of image representation in biological and machine vision", *IEEE Trans. Pattern Analysis and Machine Intelligence*, vol. 10, pp. 452–468, July 1988.

- [36] M.R. Turner, "Texture discrimination by gabor functions", *Biological Cybernetics*, vol. 55, pp. 71–82, 1986.
- [37] J.G. Daughman, "Complete discrete 2-d gabor transforms by neural networks for image analysis and compression", *IEEE Trans. Accoust. Speech, Signal Processing*, vol. 36, pp. 1169–1179, July 1988.
- [38] S. G. Mallat, "Multifrequency channel decompositions of images and wavelet models", *IEEE Trans. Accoustics, Speech and Signal Processing*, vol. 37, no. 12, pp. 2091–2110, Dec 1989.
- [39] Witkin A., "Scale space filtering", *Proc. Int. Joint Conf. Artificial Intelligence*, pp. 1019–1021, 1983.
- [40] H. Asada and M. Brady, "The curvature primal sketch", *IEEE Trans. Pattern Analysis and Machine Intelligence*, vol. PAMI-8, no. 1, pp. 2–14, Jan 1986.
- [41] K. Xin, K. B. Lim, and G. S. Hong, "A scale-space filtering approach for visual feature extraction", *Pattern Recognition*, vol. 28, pp. 1145–1158, 8 1995.
- [42] A. Rattarangsi and R. T. Chin, "Scale-based detection of corners on planar curves", *IEEE Trans. Pattern Analysis Mach. Intell.*, vol. 14, no. 4, pp. 430–449, April 1992.
- [43] P. Franklin, "A set of continuous orthogonal functions", *Math. Annal.*, vol. 100, pp. 522–529, 1928.

- [44] J. Littlewood and R. Paley, "Theorems on fourier series and power series", *Proc. London Math. Soc.*, vol. 42, pp. 52–89, 1937.
- [45] A. Calderon, "Intermediate spaces and interpolation, the complex method", *Studia Math.*, vol. 24, pp. 113–190, 1964.
- [46] I. Daubechies, "Where do wavelets come from?-a personal point of view", *Proc. IEEE*, vol. 84, no. 4, pp. 510–513, April 1996.
- [47] A. Grossmann and J. Morlet, "Decomposition of hardy functions into square integrable wavelets of constant shape", *SIAM J. Math.*, vol. 15, pp. 723–736, 1984.
- [48] N. Hess-Nielsen and M.V. Wickerhauser, "Wavelets and time-frequency analysis", *Proc. IEEE*, vol. 84, no. 4, pp. 523–540, April 1996.
- [49] I. Daubechies, "Orthonormal bases of compactly supported wavelets", *Commun. Pure Appl. Math.*, vol. 41, pp. 909–996, Nov. 1988.
- [50] S. G. Mallat, "Multiresolution approximation and wavelet orthonormal bases of l_2 ", *Trans. Amer. Math. Soc.*, vol. 3-15, pp. 69–87, Sept. 1989.
- [51] M. J. Smith and T. P. Barnwell, "Exact reconstruction techniques for tree-structured subband coders", *IEEE Trans. Acoust. Speech, Signal Processing*, vol. ASSP-34, June 1986.

- [52] M. Vetterli, "Filter banks allowing perfect reconstruction", *Signal Processing*, vol. 10, no. 3, pp. 219–244, 1986.
- [53] M. Vetterli and D. Le Gall, "Perfect reconstruction fir filter banks: Some properties and factorizations", *IEEE Trans. Acoust., Speech and Signal Processing*, vol. 37, no. 7, pp. 1057–1071, July 1989.
- [54] R. E. Crochiere and L. R. Rabiner, *Multirate digital signal processing*, Prentice-Hall, Englewood Cliffs, NJ, 1983.
- [55] S. G. Mallat and W. L. Hwang, "Singularity detection and processing with wavelets", *IEEE Trans. Information Theory*, vol. 38, no. 2, pp. 617–645, March 1992.
- [56] S. G. Mallat and S. Zhong, "Characterization of signals from multiscale edges", *IEEE Trans. Pattern Analysis and Machine Intelligence*, vol. PAMI-14, no. 7, pp. 710–732, july 1992.
- [57] P. Guillemain and R. Kronland-Martinet, "Characterization of accoustic signals through continuous linear time-frequency representations", *Proc. IEEE*, vol. 84, no. 4, pp. 561–585, April 1996.
- [58] G.W. Wornell, "Emerging applications of multirate signal processing and wavelets in digital communications", *Proc. IEEE*, vol. 84, no. 4, pp. 586–603, April 1996.

- [59] M. Unser and A. Aldroubi, "A review of wavelets in biomedical applications", *Proc. IEEE*, vol. 84, no. 4, pp. 626–638, April 1996.
- [60] M. Farge, N. Kevlahan, V. Perrier, and E. Goirand, "Wavelets and turbulence", *Proc. IEEE*, vol. 84, no. 4, pp. 639–669, April 1996.
- [61] A. Bijaoui, E. Slezak, F. Rue, and E. Lega, "Wavelets and the study of the distant universe", *Proc. IEEE*, vol. 84, no. 4, pp. 670–679, April 1996.
- [62] A. Goshtasby and G. C. Stockman, "Point pattern matching using convex hull edges", *IEEE Trans. Systems, Man Cyber.*, vol. 15, pp. 631–637, 1985.
- [63] M. H. Han and D. Jang, "The use of maximum curvature points for the recognition of partially occluded objects", *Pattern Recognition*, vol. 23, pp. 21–23, 1990.
- [64] E. R. Davies, "Locating objects from their point features using an optimised hough-like accumulation technique", *Pattern Recognition Lett.*, vol. 13, pp. 113–121, 1992.
- [65] L. Dreschler and H. Nagel, "Volumetric model and 3d trajectory of a moving car derived from monocular tv frame sequence of a street scene", *Proc. IJCAI*, pp. 692–697, 1982.

- [66] C. H. Teh and R. T. Chin, "On the detection of dominant points on digital curves", *IEEE Trans. Pattern Analysis Mach. Intell.*, vol. 11, pp. 859–872, 1989.
- [67] X. Zhang and D. Zhao, "A parallel algorithm for detecting dominant points on multiple digital curves", *Pattern Recognition*, vol. 30, no. 2, pp. 239–244, 1997.
- [68] T. Pavlidis, "Algorithms for shape analysis and waveforms", *IEEE Trans. Pattern Analysis and Machine Intelligence*, vol. PAMI-2, pp. 301–312, July 1980.
- [69] J. G. Dunham, "Optimum uniform piecewise linear approximation of planar curves", *IEEE Trans. Pattern Analysis and Machine Intelligence*, vol. PAMI-8, pp. 67–75, Jan. 1986.
- [70] L. D. Wu, "A piecewise linear approximation based on a statistical model", *IEEE Trans. Pattern Analysis and Machine Intelligence*, vol. PAMI-6, pp. 41–45, Jan. 1984.
- [71] K. Wall and P. E. Danielsson, "A fast sequential method for polygonal approximation of digitized curves", *Comput. Vision, Graphics, Image Processing*, vol. 28, pp. 220–227, 1984.

- [72] J. C. Bezdek and I. M. Anderson, "An application of the c-varieties clustering algorithms to polygonal curve fitting", *IEEE Trans. Syst., Man, Cybern.*, vol. SMC-15, pp. 637–641, Sept. 1985.
- [73] R. Bellman, "On the approximation of curves by the line segments using dynamic programming", *Comm. ACM*, vol. 4, pp. 284, 1961.
- [74] J. M. Chen, J. A. Ventura, and H. Wu, C, "Segmentation of planar curves into circular arcs and line segments", *Image and Vision Computing*, vol. 14, no. 1, pp. 71–83, Feb. 1996.
- [75] Mehrotra R. and S. Nichani, "Corner detection", *Pattern Recognition*, vol. 23, pp. 1223–1233, 1990.
- [76] M. Trajkovic and M. Hedly, "Fast corner detection", *Image and Vision Computing*, vol. 16, pp. 75–87, 1998.
- [77] L. Kitchen and A. Rosenfeld, "Gray level corner detection", *Pattern Recognition Lett.*, vol. 1, pp. 95–102, 1982.
- [78] A. Singh and M. Shneier, "Gray level corner detection: a generalization and a robust real time implementation", *Comput. Vision Graphics Image Process.*, vol. 55, pp. 54–69, 1990.
- [79] R. Deriche and G. Giraudon, "A computational approach for corner and vertex detection", *Int. J. Comput. Vision*, vol. 10, pp. 101–124, 1993.

- [80] U. Seeger and R. Seeger, "Fast corner detection in gray level image", *Pattern Recognition*, vol. 15, pp. 669–675, 1994.
- [81] B. S. Manjunath, C. Shekhar, and R. Chellappa, "A new approach to image feature detection with applications", *Pattern Recognition*, vol. 29, no. 4, pp. 627–640, 1996.
- [82] A. Dobbins, S. W. Zucker, and M. S. Cynader, "Endstopped neurons in the visual cortex as a substrate for calculating curvatures", *Nature*, vol. 329, pp. 438–441, 1987.
- [83] A. Rosenfeld and J. S. Weszka, "An improved method of angle detection on digital curves", *IEEE Trans. Comput.*, vol. C-24, pp. 940–941, Sept. 1975.
- [84] I. M. Anderson and J. C. Bezdek, "Curvature and tangential deflection of discrete arcs: A theory based on the commutator of scatter matrix pairs and its application to vertex detection in planar shape data", *IEEE Trans. Pattern Analysis and Machine Intelligence*, vol. PAMI-6, pp. 27–40, Jan. 1984.
- [85] M. Worring and W. M. Smeulders, "Digital curvature estimation", *CVGIP: Image Understanding*, vol. 58, pp. 366–382, 1993.
- [86] D. P. Fairney and P. T. Fairney, "On the accuracy of point curvature estimators in a discrete environment", *Image and Vision Computing*, vol. 12, pp. 259–265, 1994.

- [87] D. M. Tsai and M. F. Chen, "Curve fitting approach for tangent angle and curvature measurements", *Pattern Recognition*, vol. 27, pp. 699–711, 1994.
- [88] H. L. Beus and S. S. H. Tiu, "An improved corner detection algorithm based on chain-coded plane curves", *Pattern Recognition*, vol. 20, pp. 291–296, 1987.
- [89] H. C. Liu and Srinath M. D., "Corner detection from chain code", *Pattern Recognition*, vol. 23, pp. 520–540, 1990.
- [90] H. Freeman and L. S. Davis, "A corner-finding algorithm for chain coded curves", *IEEE trans. Comput.*, vol. 26, pp. 297–303, 1977.
- [91] A. Rosenfeld and E. Johnston, "Angle detection on digital curves", *IEEE Trans. Comput.*, vol. C-22, pp. 875–878, Sept. 1973.
- [92] P. V. Sankar and C. V. Sharma, "A parallel procedure for the detection of dominant points on a digital curve", *Comput. Graphics, Image Processing*, vol. 7, pp. 403–412, 1978.
- [93] C. Fermuller and W. Kropatsch, "A syntactic approach to scale-space-based corner detection", *IEEE Trans. Pattern Analysis Mach. Intell.*, vol. 16, pp. 748–751, 1994.
- [94] B. K. Ray and K. S. Ray, "Scale-space analysis and corner detection on digital curves using a discrete scale-space kernel", *Pattern recognition*, vol. 30, no. 9, pp. 1463–1474, 1997.

- [95] J. S. Lee, Y. N. Sun, C. H. Chen, and C. T. Tsai, "Wavelet based corner detection", *Pattern Recognition*, vol. 26, no. 6, pp. 853–865, 1993.
- [96] J. S. Lee, Y. N. Sun, and C. H. Chen, "Multiscale corner detection by wavelet transform", *IEEE Trans. Image Processing*, vol. 4, no. 1, pp. 100–104, Jan. 1995.
- [97] O. Zuniga and R. Haralick, "Corner detection using the facet model", *Proc. CVPR*, pp. 30–37, 1983.
- [98] D. M. Tsai, "Boundary-based corner detection using neural networks", *Pattern Recognition*, vol. 30, no. 1, pp. 85–97, 1997.
- [99] X. Xie, R. Sudhakar, and H. Zhuang, "Corner detection by a cost minimization approach", *Pattern Recognition*, vol. 26, no. 8, pp. 1235–1243, 1993.
- [100] S. Kwanghoon, H. K. Jung, and W. E. Alexander, "A mean field annealing approach to robust corner detection", *IEEE Trans. Systems, Man and Cybernetics, Part B.*, vol. 28, no. 1, pp. 82–90, Feb. 1998.
- [101] D. Marr and E. Hildreth, "Theory of edge detection", *Proc. Royal Soc. London.*, vol. 207, pp. 187–217, 1980.
- [102] I. Daubechies, *Ten lectures on wavelets*, SLAM, 1992.

- [103] A. Cohen, I. Daubechies, and Feauveau. J.C., "Biorthogonal basis of compactly supported wavelets", *Comm. Pure Appl. Math.*, vol. 45, pp. 485–560, 1992.
- [104] A. Quddus and M. M. Fahmy, "Corner detection using gabor-type filtering", *IEEE Intl. Symposium on Circuits and Systems (ISCAS'98)*, June 1998.
- [105] S. Marcelja, "Mathematical description of the responses of simple cortical cells", *J. Opt. Soc. Amer.*, vol. 70, no. 11, pp. 1279–1300, 1980.
- [106] J.S. Boreczky and L.A. Rowe, "Comparison of video shot boundary detection techniques", *SPIE Proceedings*, vol. 2670, pp. 170–179, 1996.
- [107] Q. M. Tieng and W. W. Boles, "Wavelet-based affine invariant representation: A tool for recognizing planar objects in 3-d space", *IEEE Trans. Pattren Analysis and Machine Intelligence*, vol. PAMI-19, no. 8, pp. 846–857, Aug. 1997.
- [108] Q. M. Tieng and W. W. Boles, "Recognition of 2d object contours using the wavelet transform zero-crossing representation", *IEEE Trans. Pattren Analysis and Machine Intelligence*, vol. PAMI-19, no. 8, pp. 910–916, Aug. 1997.
- [109] L. M. Reissel, "Wavelet multiresolution representation of curves and surfaces", *Graphical Models and Image Processing*, vol. 58, no. 3, pp. 198–217, May 1996.

- [110] J. S. Lee, Y. N. Sun, and C. H. Chen, "Wavelet transform for corner detection", *Proc. IEEE International Conference on Systems Engineering, Kobe, Japan.*, pp. 596–599, Sept. 1992.
- [111] A. Rosenfeld and J.S. Weazka, "An improved method of angle detection on digital curves", *IEEE Trans. Comput.*, vol. C-24, pp. 940–941, Sept. 1975.

Vita

- AZHAR QUDDUS

- Born in India, on December 10, 1967.

- Permanent Address :

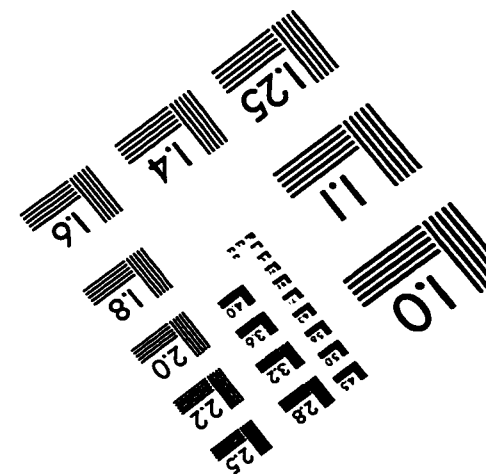
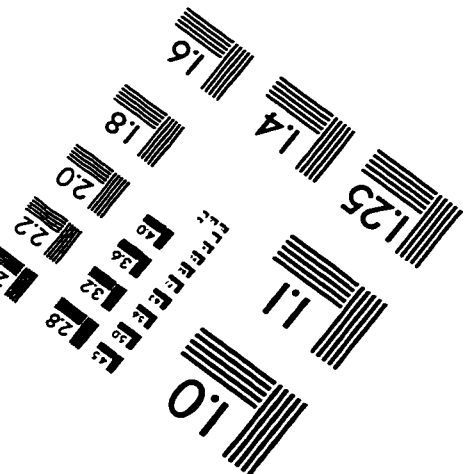
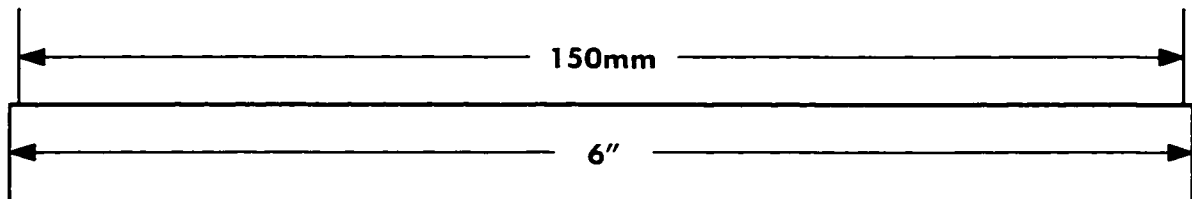
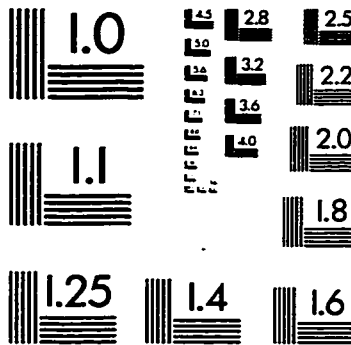
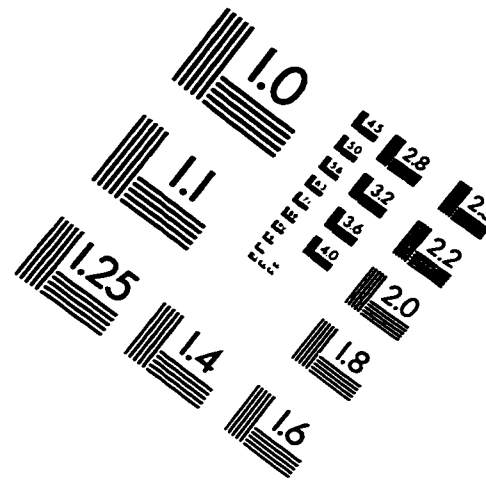
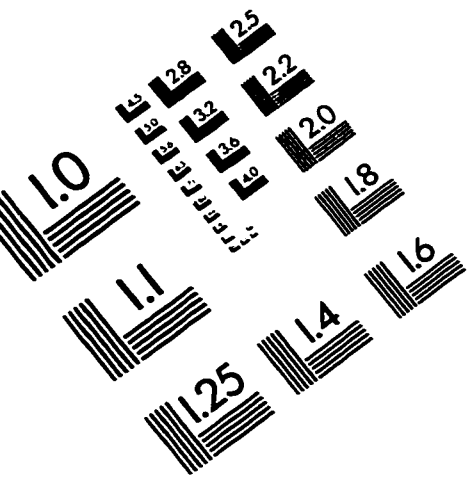
H.No. C-536, Kareli Colony,

G. T. B. Nagar, Allahabad 211016,

INDIA.

- Received Bachelor of Engineering (B.E.) degree in Electronics and Communication Engineering from Gulbarga University, Gulbarga, India in May 1988.
- Received Master of Science in Engineering (MSc. Engg) degree in Electronics Engineering from Aligarh Muslim University, Aligarh, India in May 1991.
- Joined Ph.D. program, in Electrical Engineering Department at KFUPM, Dhahran, Saudi Arabia, in February 1994.
- Research Areas: Image Processing, Computer Vision, Time Frequency and Time Scale Analysis and Electronic Circuits.
- Publications: Currently, there are seven publications in refereed journals and international conferences.

IMAGE EVALUATION TEST TARGET (QA-3)



APPLIED IMAGE, Inc.
1653 East Main Street
Rochester, NY 14609 USA
Phone: 716/482-0300
Fax: 716/288-5989

© 1993, Applied Image, Inc., All Rights Reserved